Doctoral Dissertation (Shinshu University)

Studies on flux growth of inorganic oxide-based ion exchange crystals with two- or three-dimensionally nanostructured channels

March 2017

Xiong XIAO

Dedicated to my family.

Abstract

"Materials" are identified as condensed-state substances that exhibit characteristics intended for certain applications. Materials are often described in terms of "composition + structure," where "structure" includes the crystallinity, nanostructure, and morphology of the material, all of which are strongly affected by the method of preparation. Flux growth techniques are a powerful method to grow idiomorphic crystals below the melting point of the solutes. Herein, I focus on the flux growth of inorganic oxide materials with high crystallinities, nanostructural channels that can exchange specific ions, well-developed crystal facets, and appropriate morphologies. This work aims to understand the manner in which these materials grow from fluxes.

Chapter 1 summarizes the factors that affect the performance of these materials, their flux growth method, and my overall research objectives.

Chapter 2 presents the low-temperature growth of idiomorphic $Li_5La_3Ta_2O_{12}$ single crystals from LiOH flux. The $Li_5La_3Ta_2O_{12}$ crystals were grown at 500 °C from LiOH flux and subsequently transformed into $Li_7La_3Ta_2O_{13}$ at 700 °C. The pseudo-perovskite-type $LiLa_2TaO_6$ phase, initially formed during holding at 500 °C, was efficiently transformed into the $Li_5La_3Ta_2O_{12}$ phase with an extended holding time. The growth of $Li_5La_3Ta_2O_{12}$ crystals was independent of the cooling rate but was affected by the flux type and the solute concentration. Thus, a low solute concentration (1 or 5 mol%) was the key to obtaining well-dispersed and idiomorphic single crystals. These results indicate that the formation and growth of $Li_5La_3Ta_2O_{12}$ single crystals are not only controlled by a general flux growth process but also involve chemical reactions between the solutes and the LiOH flux. Finally, high-resolution transmission electron microscopy images and selected-area electron diffraction patterns were used to identify products with high crystallinity and well-developed {110} and {211} facets.

In **Chapter 3**, the flux growth of β-Li_2TiO_3 crystals was studied comprehensively under different conditions. Results demonstrating efficient anisotropic growth of {001}-faceted β-Li_2TiO_3 single crystals using the Na_2SO_4 flux method are presented. In the Na_2SO_4 flux at 1000 °C, the optimal solute concentration for growing large (~15.0 μm in lateral size), plate-like, and faceted β-Li_2TiO_3 crystals is 20 mol%.

Observations from experiments conducted at various holding times indicate that these crystals were grown anisotropically. TEM images with clear electron diffraction spots reveal that the flux-grown plate-like β-Li_2TiO_3 are single crystals with dominant {001} facets. This anisotropic crystal growth is attributed to the concerted effects of the preferential attachment of sodium cations on the {001} faces and to efficient dissolution of β-Li_2TiO_3 crystals as well as the solvation of the resulting O^{2-} ions in the sulfate-based flux.

Chapter 4 presents a combined experimental and computational study of $KTiNbO_5$ (KTN) as a selective and durable adsorbent for Sr^{2+} ions. KTN grown from a nitrate flux at 500–600 °C (KTN_{flux}) has a zigzag, layered gallery space. The structural analysis indicates that KTN_{flux} crystals are plate-like, with surface areas from 48 to 86 $m^2 \cdot g^{-1}$. These areas are ~50 times larger than those of KTN prepared by solid-state reaction at 1100 °C. This dramatic increase in surface area is a result of efficient, anisotropic crystal growth. Sr^{2+}-adsorption experiments indicate that the Sr^{2+} ion-exchange capacity of KTN_{flux} is ~1.04 $mmol \cdot g^{-1}$ and that most of the ion-exchange sites are homogeneous. The kinetic analysis shows that the Sr^{2+} ion-exchange rate on KTN_{flux} is one order of magnitude higher than that on KTN_{SSR}. The dependence of the distribution coefficient, K_d, for Sr^{2+} on the Na^+ concentration indicates that the KTN_{flux} shows a high affinity for Sr^{2+} in addition to remarkable durability and that $K_d > 1.26 \times 10^4$ $mL \cdot g^{-1}$ even at $[Na^+] = 0.1$ $mol \cdot L^{-1}$. The origin of the high selectivity for Sr^{2+} was studied by density functional theory (DFT). The results of these calculations indicate that the high preference for Sr^{2+} is due to confinement within subnanometer-sized pockets built from oxygen species of both the anionic metalate frameworks and intercalated water molecules, forming monocapped heptahedra or octahedra that resemble the active sites of enzymes.

In **Chapter 5**, the conclusions from the present research as well as future perspectives are summarized.

Contents

Chapter 1
Introduction

Chapter 1 Introduction

1.1 Crystalline inorganic oxides

"Materials" are identified as condensed-state substances with properties intended for certain applications. Materials are often described in terms of "composition + structure," where "structure" includes the crystallinity, nanostructure, and morphology of the material, all of which are strongly affected by the method of preparation. An understanding of the features of the crystal structures of crystalline materials is particularly important and motivates the in-depth study of the correlations between the crystal structure and the observed performances. Therefore, the following introduction focuses on crystalline inorganic materials.

1.1.1 Nanostructure of crystals

Crystalline inorganic materials can be classified into one-dimensional (1D), two-dimensional (2D), and three-dimensional (3D) structural materials according to the possible dimensionality of the passageways for mobile ions in the inorganic frameworks. These passageways may be affected by the application of an external electric field, potential, or concentration gradient. They are always built from immobilized polyhedra attached via corner, edge, or face sharing to form ion migration channels for mobile ions. **Table 1.1** shows the sub-classes of ion-exchanger species in the group of crystals; the classifications are based on the features of the crystal structures.

A. Crystals with 1D channels

In materials with a 1D channel structure, the mobilized ions in the framework can diffuse in only one direction. Cations are stabilized in the 1D diffusion pathways; *i.e.*, high activation energies are needed for ion migration. Therefore, compared to other structures, ion-exchange materials with tunnel-like structures are rare.

Table 1.1 Principal Classification of Ion Exchangers in the Group of Crystals; Classification Is Based on Features of the Crystal Structure

Category	Typical Example		
	Tunnel-like 1D structure	Layered 2D structure	Caged 3D structure
Aluminosilicate	Protonated albite ($NaAlSi_3O_8$, triclinic)	Clay[1–4]	Zeolite[1,5–7]
Hydrous oxide	α-MnO_2 ([2×2]), β-$MnO_2 \cdot nH_2O$ ([1×1]), R (ramsdellite)-MnO_2 ([2×1])[8–10] $Na_2Co_2B_{12}O_{21}$[11] $Na_2Ti_6O_{13}$[12] $Na_2Nb_2O_6 \cdot H_2O$[13,14]	Metal titanates/niobium ($KNbO_3$,[14] $Na_2Ti_3O_7$[12]) $Na_2Si_2O_{17}$ H_2O Antimony oxides ($(H_3O)_2Sb_2O_6 \cdot nH_2O$)	Spinel-type oxides ($MnO_2 \cdot 0.5H_2O$,[15,16] λ-MnO_2[17]) H_2TiO_3,[18,19] $Rb_8Nb_{22}O_{59}$[20,21] Niobium and tantalum oxides ($LiNbO_3$, $LiTaO_3$) $HSbO_3 \cdot nH_2O$[22,23]
Phosphates	Hydroxyapatite ($Ca_{10-x}H_x(PO_4)_6(OH)_{2-x}$)[24–26]	$Zr(HPO_4)_2 \cdot nH_2O$[27,28] $KSb(PO_4)_2 \cdot nH_2O$, $Nb/TaH(PO_4)_2$	Aluminophosphate[29] Protonated NASICON[30,31]
Carbon materials		MXene[32–34]	
Sulfides		$K_2MnSn_2S_6$ (KMS-1)[35] $K_{2x}Mg_xSn_{3-x}S_6$ ($0.5 \leq x \leq 1$) (KMS-2)[36] $K_{2x}Sn_{4-x}S_{8-x}$ ($0.65 \leq x \leq 1$)[37]	
Hydroxides		Layered double hydroxide (LDH)[38,39]	
Heteropolyacid salts			Ammonium molybdophosphate[40,41] Ammonium molybdosilicate[42]
Ferrocyanides			$A_2Zn_3[Fe(CN)_6]_2 \cdot nH_2O$ (A = Na, K)[43–45]

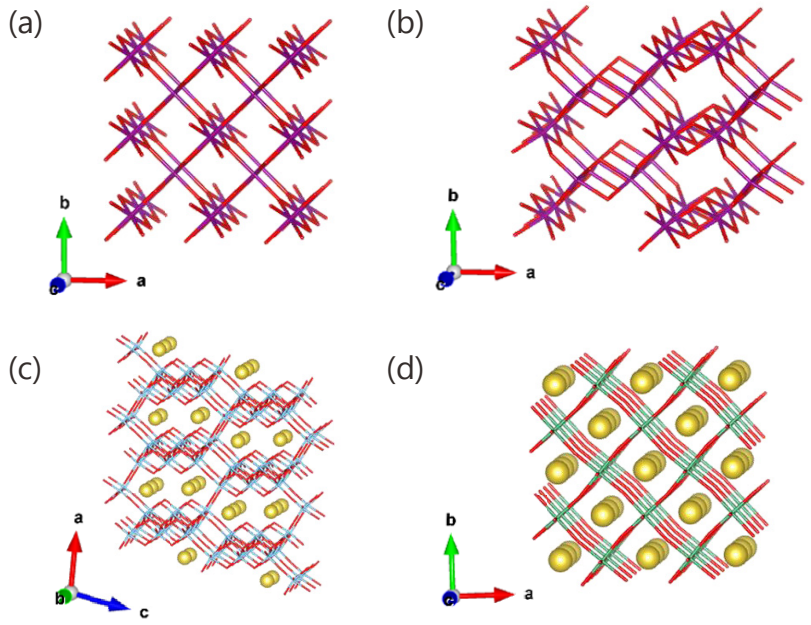

Figure 1.1 The 1D nanostructural channels of (a) [1×1] tunnels (pyrolusite), (b) [2×2] tunnels (hollandite), (c) $Na_2Ti_6O_{13}$,[51] and (d) $Na_2Nb_2O_6$.[52] The crystal structures were visualized using the VESTA program.

One-dimensional tunnel manganese oxides are the largest family of materials with a 1D channel structure. Tunnel structures can be constructed via both edge- and corner-sharing of MnO_6 octahedra to form [1×1] tunnels (pyrolusite), [2×2] tunnels (hollandite), [2×3] tunnels (romanechite), or [3×3] tunnels (todorokite).[8,9,46] **Figure 1.1a** and **b** show [1×1] and [2×2] tunnel structures of MnO_2, respectively. These tunneled manganese oxides have been extensively studied for potential applications, such as cation exchange,[47] batteries,[48] and catalysis.[49,50] Manganese oxides are difficult to use in commercial applications because they pose the risk of releasing toxic manganese ions, resulting in secondary pollution due to their unstable chemical properties.

The titanate/niobate-based materials $Na_2Ti_6O_{13}$ and $Na_2Nb_2O_6$ have been taken as representatives of this class because of their environmentally friendliness and chemical stability. **Figure 1.1c** and **d** illustrates the structures of $Na_2Ti_6O_{13}$[51] and $Na_2Nb_2O_6$,[52] respectively. $Na_2Ti_6O_{13}$ has microporous tunnels consisting of eight linked TiO_6 octahedra forming a quasi-rectangular shape, and the sodium ions located in these tunnels are exchangeable (**Figure 1.1c**). $Na_2Ti_6O_{13}$ has been investigated for use in

various applications, including as a cation exchanger,[12] an anode for sodium-ion batteries,[53] and a parent material for photocatalysts.[54] $Na_2Nb_2O_6$, one of the members of the group of Sandia octahedral molecular sieves (SOMS),[13,55] comprises a framework of NbO_6 and NaO_6 octahedra linked by corner- or edge-sharing with the exchangeable Na^+ ions residing in the tunnels (**Figure 1.1d**). It is primarily used as an ion exchanger. For instance, the CECs for sorption of Sr^{2+} and Ba^{2+} ions are ~2.53 and ~1.05 mmol g^{-1}, respectively, at a pH from 6 to 7.[14]

B. Crystals with 2D channels

In materials with 2D channel structures, mobilized ions in the frameworks can diffuse freely in a plane. Normally, materials in this group have layered structures.

Clays composed of mainly tetrahedrally arranged SiO_4 and octahedrally arranged $Al(O,OH)_6$, such as kaolinite, montmorillonite, and illite, are well-known ion exchanger species (**Figure 1.2 a-c**).[1–3,56–59] Clay minerals and their modified forms (clay minerals treated with acids and alkalis or by organic functionalization) are widely utilized in many facets of our society, such as tiles and sanitary ware, paper coatings, plastic fillers, catalysts, and adsorbents.[3,4] Layered titanate/niobate-based oxides are another large category of layered materials with a 2D structure. The structures of these compounds are built of octahedra sharing edges or oxygen atoms forming a double plane, and exchangeable cations lie between the planes, binding them together by electrostatic attraction. **Figure 1.2 d-g** shows idealized structures of some titanate/niobate-based oxides with a layered structure.[60–63] The interlayers of titanate/niobate-based oxides contain more types of nanospaces compared to the interlayers of clays, which have only flat interlayer spaces (**Figure 1.2 a-c**). Although no systematic research on this topic has been reported, due to intercalated water and exchangeable sites, for example, these nanospaces may influence the ion-exchange process.[12,14] Layered titanate/niobate-based oxides are widely used as hosts for catalysts,[64,54,65,66] ion-exchangers,[14,67] piezoelectric materials,[68] and luminescent materials.

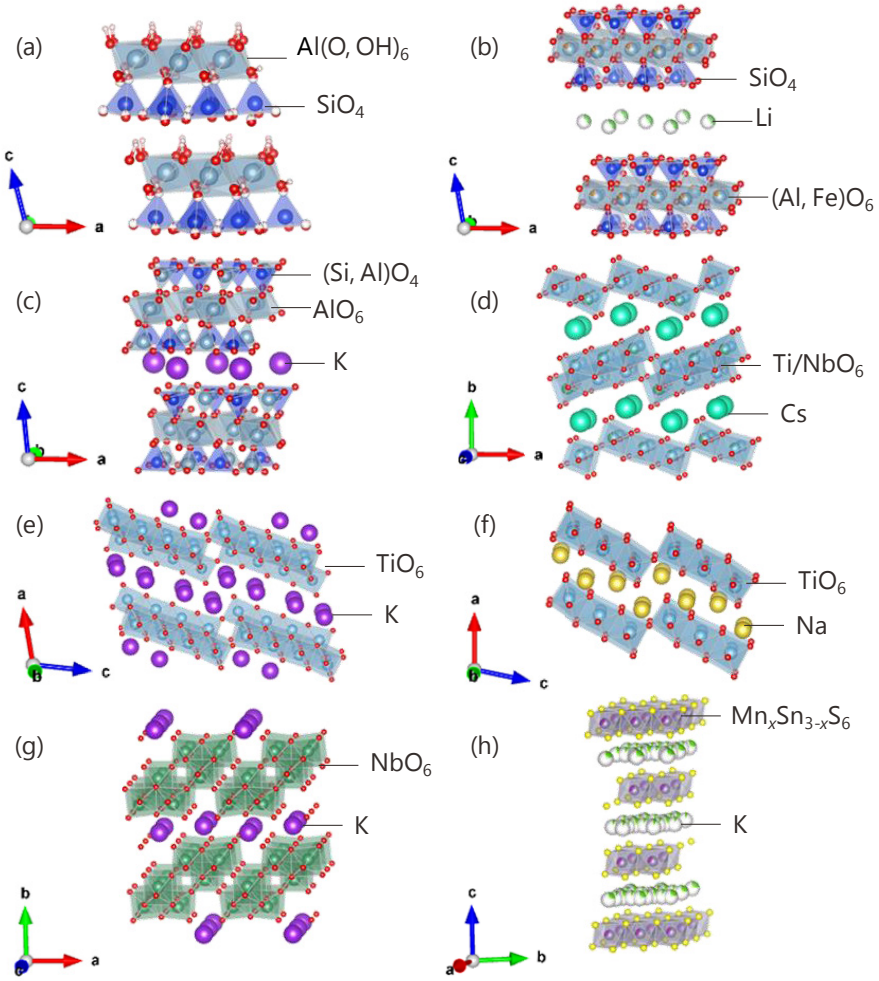

Figure 1.2 The 2D nanostructural channels of (a) kaolinite,[57] (b) montmorillonite,[58] (c) illite,[59] (d) $CsTi_2NbO_7$,[60] (e) $K_2Ti_4O_9$,[61] (f) $Na_2Ti_3O_7$,[62] (g) KNb_3O_8,[63] and (h) $Mg_{0.667}Al_{0.333}(OH)_2(CO_3)_{0.167}\cdot(H_2O)_{0.5}$.[71] The crystal structures were visualized using the VESTA program.

Layered sulfides,[35–37,69,70] a new family in the group of layered 2D materials, show a substantial affinity for some radioactive ions and can selectively uptake them from aqueous solutions. For instance, $K_{2x}Mn_xSn_{3-x}S_6$ (KMS-1, $0.5 \leq x \leq 0.95$) has a 2D layered structure. As shown in **Figure 1.2h**, KMS-1 consists of hexagonal $[Mn_xSn_{3-x}S_6]^{2x-}$ slabs of the CdI_2 type. Highly mobile K^+ ions are contained in their interlayer space, and these ions are easily exchangeable with other cations.[70] KMS-1 displays an outstanding preference for Cs^+ ions[35] and Sr^{2+} ions[70] under both strongly acidic and strongly basic conditions. The maximum Cs^+ and Sr^{2+} exchange capacities of KMS-1 were found to be 0.90 and 1.70 mmol g^{-1}, respectively.

Layered double hydroxides (LDHs), also known as anionic clays, are a family of

materials that have attracted increasing attention in various fields. LDHs exhibit anionic exchange capacity, and their ability to capture organic and inorganic anions makes them almost unique as inorganic materials. $Mg_{0.667}Al_{0.333}(OH)_2(CO_3)_{0.167}\cdot(H_2O)_{0.5}$ is a well-known and the most extensively studied LDH.[71] These compounds can be expressed as $[M(II)_{1-x}M(III)_x(OH)_2]^{x+}[A^{n-}]_{x/n}\cdot zH_2O$ (M(II) = Mg, Ni, Zn, Cu; M(III) = Al, Fe, Cr; A^{n-} = OH^-, NO_3^-, Cl^-, CO_3^{2-}, SO_4^{2-}).[38,39] Because of their wide range of possible compositions, LDHs have applications in many fields, including catalysis,[72–74] ion-exchange and adsorption,[72,73,75] pharmaceutics,[76,77] and electrochemistry,[73,78] among others.[79]

MXene is a newly discovered and large family of 2D materials based on transition-metal carbides and/or nitrides.[80] MXenes are produced by selective etching of the A-element layers from the layered hexagonal transition-metal carbides and or nitrides of MAX phases.[81] $Ti_3C_2T_x$ is the most widely studied and best understood member of the MXene family, where T represents a surface termination (O, OH, F, H, *etc*.), and x is the number of terminating groups.[34] $Ti_3C_2T_x$ has a negatively charged and hydrophilic surface as well as a high surface area. It can act as an efficient adsorbent to remove or uptake cations from aqueous solutions. The adsorption properties of $Ti_3C_2T_x$ have been investigated, and the results of adsorption experiments show that a wide range of cations with various sizes and charges can intercalate between the $Ti_3C_2T_x$ layers.[32–34] When $Ti_3C_2T_x$ is formed into membranes, the formed $Ti_3C_2T_x$ membranes demonstrate attractive separation properties based on the selective permeation of cations with various sizes and charges.[33]

C. Crystals with 3D channels

In materials with a 3D channel structure, ions mobilized in the crystal framework can diffuse in three dimensions. Zeolites and closely related systems such as aluminophosphates represent the predominant class of materials with a crystalline 3D channel structure.

Zeolites, *i.e.*, crystalline hydrated aluminosilicates, are built from $[SiO_4]^{4-}$ and

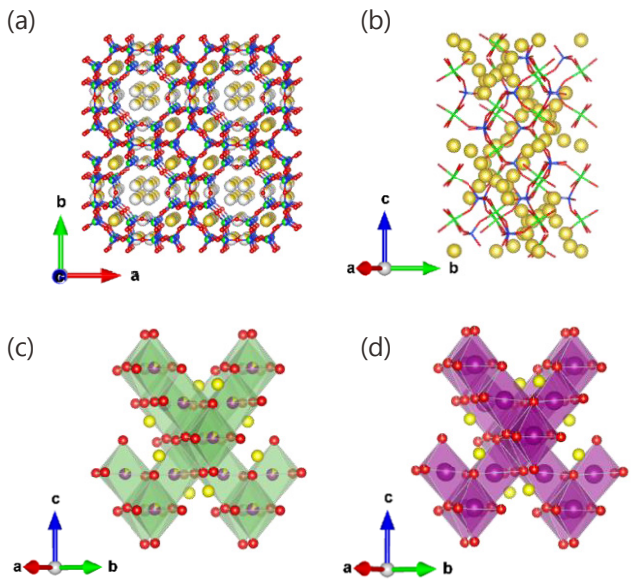

Figure 1.3 The 3D nanostructurcal channels of (a) zeolite 4A[82] and (b) NASICON,[83] (c) non-stoichiometric $LiNi_{0.5}Mn_{1.5}O_{4-\delta}$,[87] and (d) $Li_4Ti_5O_{12}$. The crystal structures were visualized using the VESTA program.

$[AlO_4]^{5-}$ tetrahedra connected by oxygen bridges, and they exist in more than 100 different structures. These structures have already been widely used as absorbents, molecular sieves, and most importantly, catalysts on an industrial scale. For instance, zeolite A, one of the hydrated low-silica zeolites (Si/Al < 2), is used widely as an ion exchanger because of its high CEC, low cost, and favorable kinetics. **Figure 1.3a** illustrates the structure of zeolite A.[82] The maximum CECs of zeolite A for Cs^+ and Sr^{2+} ions are in the ranges 2.51–2.54 and 4.90–5.51 mmol g^{-1}, respectively.[5]

Figure 1.3b shows the typical structure of a NASICON (Na super-ion conductor)-type phosphate. NASICONs have the general compositional formula $Na_3M_2(XO_4)_3$, where A = Ni, Co, Mn, Fe, Ti, or V and X = S, P, As, Mo, or W. For instance, NASICON with the composition of $Na_3V_2(PO_4)_3$ is built by VO_6 octahedra interlinked via corners with tetrahedral PO_4 to establish a 3D $V_2(PO_4)_3$ framework.[83,84] The created lantern units feature a highly covalent open structure that generates large interstitial spaces through which Na ions can diffuse. These units have been examined mainly for their conduction properties.

Non-stoichiometric $LiNi_{0.5}Mn_{1.5}O_{4-\delta}$ has attracted extensive interest over the past few

decades. Because of its good cycling behavior and relatively high capacity, with one dominant plateau at high voltage, it has attracted research interest as a high-voltage cathode material in the field of Li-ion batteries.[85,86] **Figure 1.3c** shows the crystal structure of $LiNi_{0.5}Mn_{1.5}O_{4-\delta}$, which has a face-centered cubic spinel structure in the *Fd*-3*m* space group. It can be expressed as $Li_{(8a)}[Ni_{0.5}Mn_{1.5}]_{(16d)}O_{4-\delta(32e)}$, in which the Li, Ni and Mn, and O atoms occupy the 8a tetrahedral sites, 16d octahedral sites, and 32e sites, respectively.[87,88] **Figure 1.3d** shows the crystal structure of $Li_4Ti_5O_{12}$. $Li_4Ti_5O_{12}$, another material in the spinel group, has attracted considerable attention as a promising anodic material for lithium-ion batteries (LIBs) because of its small change in volume during the lithium insertion/extraction process, long cycling lifetime, and safety.[89–92] At room temperature, the basic crystal structure of $Li_4Ti_5O_{12}$ is also a cubic spinel in the *Fd*-3*m* space group. The spinel $Li_4Ti_5O_{12}$ can be expressed as $Li_{(8a)}[Li_{1/3}Ti_{5/3}]_{(16d)}O_{4(32e)}$ in space notation. Here, the octahedral 16c sites and the tetrahedral 8b and 48f sites are empty, making this material suitable for lithium diffusion and insertion/extraction.[90,92] The isotropic structures of spinels $LiNi_{0.5}Mn_{1.5}O_{4-\delta}$ and $Li_4Ti_5O_{12}$ provide a 3D network for lithium-ion diffusion; hence, these materials are suitable for fast lithium-insertion and -extraction reactions.

1.1.2 Morphology of materials

Depending on the apparent morphology of materials, they can be divided into zero-dimensional (0D), 1D, 2D, and 3D materials. The details of these morphologies will be discussed in the following subsections.

A. Zero-dimensional materials

In 0D materials, all the dimensions are measured within the nanoscale. The most common representation of 0D materials are nanoparticles. The reduced particle size can increase the specific surface area for an interfacial reaction and decrease the distance of ion or electron diffusion.[91] The shape of 0D materials attracts much attention because it not only controls the physicochemical properties of 0D materials but also determines

their relevance and merit for applications ranging from catalysis to optics, electronics, magnetics, photonics, energy storage, environmental protection, and medicine.[93–95,97,98] The shape of a crystal depends on the growth rates of the different crystallographic faces. The growth of a given face is governed by the crystal structure and defects and by the growth conditions, which will be introduced in section 1.2. Controllable growth of crystals with specific surfaces has been studied in detail in the field of 0D metal nanomaterials.[94,95] Changing the shape of a metal nanocrystal is well known to potentially profoundly alter its properties, and thus, its performance in a given application. For instance, tetrahexahedral platinum nanocrystals with high-index facets such as {730}, {210}, and/or {520} surfaces, efficiently enhanced (by up to 400%) the catalytic activity of Pt for the electro-oxidation of small organic fuels.[96]

B. One-dimensional materials

One-dimensional materials, such as tubes, wires, rods, and fibers, have stimulated increasing interest because of their wide range of potential applications in fabricating electronic, optoelectronic, electrochemical, and electromechanical devices with nanoscale dimensions.[97] To date, four different strategies have been demonstrated for preparing 1D materials: (i) dictation by the anisotropic crystallographic structure of a solid through the “bottom up” approach; (ii) introduction of a liquid-solid interface to reduce the symmetry of a seed; (iii) use of various 1D templates to direct the formation of 1D materials; and (iv) kinetic control provided by a capping agent.[97]

C. Two-dimensional (2D) materials

Two-dimensional materials, such as nanosheets and nanoplates, have two dimensions outside of the nanometric size range. The synthesis of 2D materials has become a focal area in materials research because of their numerous low-dimensional characteristics that differ from the properties of the corresponding bulk materials. For instance, transition-metal dichalcogenides (TMDs) and MXenes have gained world-wide attention in recent years and are being heavily researched for use in photovoltaic devices, LIBs, hydrogen evolution catalysts, transistors, photodetectors, DNA detection

devices, and memory devices.[99]

D. Three-dimensional materials

The synthesis of 3D NSMs with a controlled structure and morphology is of great interest because of their large specific surface area and other properties that are superior to those of their bulk counterparts, arising from quantum size and shape effects. Typical 3D materials such as nanopillars, nanoflowers, and mesoporous materials have a wide range of applications in the area of catalysis, magnetic materials, and electrode materials for batteries because of their high surface area, which can supply correspondingly more absorption and reaction sites.

1.1.3 Processes for ion insertion, diffusion, and extraction

Inorganic oxide materials with exchangeable ions are interesting to chemists because of their great potential in various applications ranging from batteries, to ion sieves, to host materials for sensing, catalysis, luminescence, and drug delivery. For instance, in the fields of photochromic and photocatalytic materials, a host material with the appropriate geometry and chemical environment enables modification of its photo-properties by exchanging species in its nanospace.[64] Such materials can be used as both

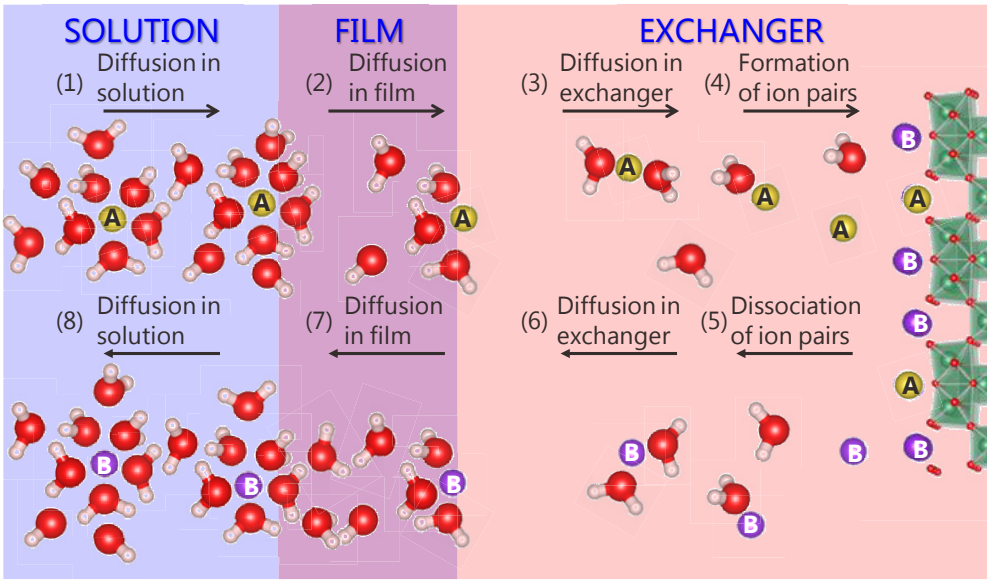

Figure 1.4 Schematic of the general steps in an ion-exchange process.

functional materials or as parent materials for design. The properties of these materials are affected by ion-exchange processes. Most cases are related to ion-exchange processes, which can be divided into the following consecutive steps, as shown in **Figure 1.4**: (1) diffusion of the A ion from the solution toward the inter-phase film; (2) diffusion of the A ion through the inter-phase film, also called film diffusion or external diffusion; (3) diffusion of the A ion inside the material phase (internal diffusion); (4) association between the A ion and exchangeable site; (5) dissociation of the B ion from the exchangeable site; (6) diffusion of the B ion inside the material phase toward the surface; (7) diffusion of the B ion through the inter-phase film; and (8) diffusion and distribution of the B ion in the solution.

Steps 1, 2, 7, and 8 are affected by the temperature, stirring speed, and viscosity of the solution (*e.g.*, water, organic electrolyte, or chelating agent) as well as by the size, surface area, and exposed surface features of the material. Steps 3, 4, 5, and 6 are affected by the crystallinity, framework and physicochemical properties of the material. Hence, the important characteristics pertinent to applications of these materials are crystallinity, particle size, shape, surface chemistry, and area, and other physical and chemical properties.

1.2 Flux growth method

Crystal growth requires careful control of phase changes. Three main categories of crystal growth methods can be defined: vapor-phase growth,[83,86] liquid-phase growth,[102,103] and solid-state growth.[101,104] Liquid-phase growth methods can be subdivided into melt-state growth and solution growth methods. Flux growth methods are a type of solution growth method. In nature, flux growth has been occurring since the formation of the Earth. The most notable example is the formation of diamonds in the hot and fluid magma below the crust.[105]

Several groups have conducted extensive work on the growth of functional crystals using flux growth methods. Our group also reported the growth of various functional

crystals with special surface facets and various crystal sizes ranging from nanometers to millimeters under different conditions obtained by varying the atmosphere, temperature, solute concentration, and cooling rate.[106–111] The growth temperature can be lowered to 350 °C.[106]

1.2.1 Theory of flux growth method

The flux growth method is a modification of the high-temperature solid-state reaction method, with the addition of inorganic salts or metals as a solvent to facilitate the growth of crystals with improved crystallinity and particle homogeneity. The simplest way to introduce concepts related to the growth of crystals by the flux growth method is with a simple binary eutectic system. **Figure 1.5** shows the phase diagram of a binary eutectic system consisting of a crystal A and flux B. First, the constituents of crystal A are dissolved in a suitable flux. Crystallization then occurs as the solution becomes critically supersaturated. Two different routes to supersaturation exists. One is by evaporation of the flux (from point a to point b in **Figure 1.5**), and the other is by cooling the solution (from point a to point c in **Figure 1.5**). In the former case, the flux solution is supersaturated through evaporation of the flux. This route requires the flux to be highly volatile. The latter route is to supersaturate the flux system by cooling the

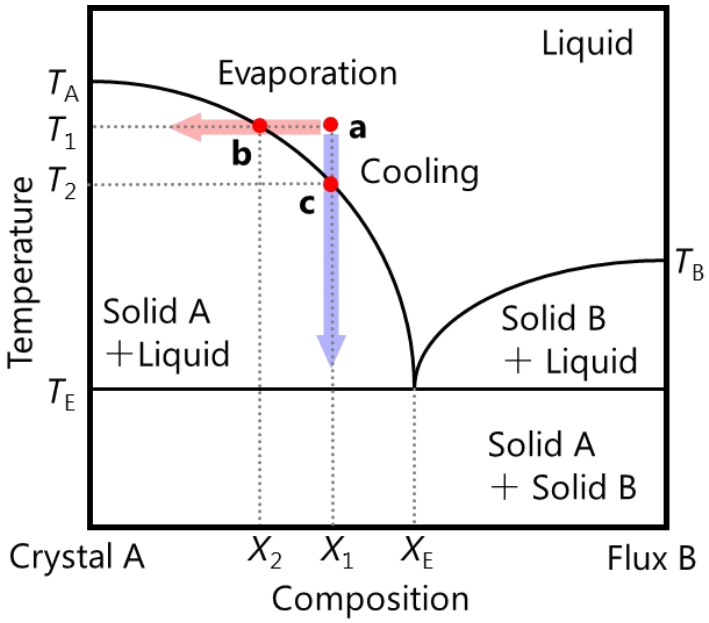

Figure 1.5 Typical phase diagram of a binary system consisting of crystal A and flux B.

solute from high temperature to low temperature. This route requires the solubility of solutes to be sensitive to temperature changes.

The advantages and disadvantages of the flux growth method are summarized in **Table 1.2**. There are three main advantages of the flux method. One of the principal advantages is that crystals are grown below the melting point of the solutes, which may also enable the growth of low-temperature phases that cannot be prepared otherwise. The following possible reasons are considered for the low-temperature crystal growth character of the flux method: (i) The flux is a powerful solvent for the starting materials; *i.e.*, it breaks chemical bonds, generating ions that can easily react and form the target crystal. (ii) The flux acts like a catalyst, decreasing the reaction activation energy. (iii) The flux reacts with the solutes to form intermediates, changing the route for formation of the target product and decreasing the reaction activation energy.

Table 1.2 Advantages and Disadvantages of the Flux Growth Method

Advantages	Disadvantages
• Crystal growth below the melting point	• Separation of crystals and flux
• Formation of crystals with developed facets, controllable size, and fewer defects	• Low crystal growth rate
• Simple equipment	• Lack of knowledge of the growth mechanism
	• Flux incorporation into crystals

Furthermore, the use of a flux allows crystal growth in the absence of a temperature gradient, which not only minimizes mechanical or thermal constraints on the crystals grown from the solution but also reduces the presence of crystal defects, leading to the formation of high-quality crystals with developed facets. The formation of faceted crystals is determined foremost by thermodynamic control, which is affected by temperature, pressure, and the surrounding environment; to a lesser extent, the formation of faceted crystals is determined by kinetic control, which depends on the concentration, mass transport, temperature, and the involvement of foreign species. The set of thermodynamic and kinetic controls are intimately and intricately entangled with each other.[93,112] The essence of thermodynamic control is to minimize the total surface free energy of a system,[93] and a thermodynamically controlled synthesis can be

achieved in two ways: (i) by adding different types of capping agents to selectively cap different metal facets, resulting in selective lowering of the specific surface free energies of the capped facets, and (ii) by controlling the coverage density of a capping agent through adjusting its concentration and reaction time in the system.[93] In some cases, however, especially in the field of nanocrystals, the surface diffusion is not adequate. Thus, the crystal will be trapped in a thermodynamically less favorable shape, leading to the formation of a kinetic product. The exact shape displayed by the nanocrystal is determined by the rates of atom deposition ($V_{deposition}$) and surface diffusion ($V_{diffusion}$), which are kinetic parameters and can be changed by varying the experimental conditions related to chemical kinetics.[93] When $V_{deposition}/V_{diffusion} \ll 1$, most of the adatoms will migrate to the site lowest in surface free energy, driven by thermodynamics. In contrast, when $V_{deposition}/V_{diffusion} \gg 1$, surface diffusion can be ignored, and the growth will be switched to a kinetically favored direction. Therefore, changing the values of $V_{deposition}/V_{diffusion}$ through experimental design offers a possible way to control the shape of the desired crystals. The concept of thermodynamic and kinetic control of crystal growth has been widely used in nanocrystal growth using solution-phase methods.

Finally, the simplicity of the technique, which does not require substantial investment in expensive equipment, is also one of its merits.

The flux method also has some disadvantages. **Table 1.2** shows the four main disadvantages of using the flux method. First, removal of the flux by dissolution in a suitable solvent is typically necessary to separate the crystals. Water is the ideal solvent because fluxes are water-soluble, whereas the crystals are not water-sensitive. Second, the flux method is time-consuming compared to the crystal pulling method because of its low rate of crystal growth. Third, the lack of knowledge of the solution dynamics hampers the development of flux growth methods. For instance, solvent–solute interactions are expected to be important and the crystal–solution interface is expected to influence the growth process; however, no good methods exist for routinely studying these processes.[113] Therefore, systematic investigations and optimization of the growth

conditions for target crystals is necessary to evaluate the data, propose an appropriate mechanism, and verify the proposed mechanism in other crystals. Lastly, I note that substitutional or interstitial incorporation of flux ions into the crystal can lead to the formation of unexpected compositions and structures and is also a method to discover and synthesize new materials.

1.2.2 Choice of fluxes

The selection of a "perfect" flux by overall consideration of the advantages and disadvantages of the flux growth method is necessary. The wide variety of fluxes available as solvents for crystal growth complicate the choice of a "perfect" flux. On the basis of the published criteria and their own observations, Elwell and Scheel have stated the following criteria for an ideal flux:[105]

1) Reagents should be highly soluble in the flux.

2) The crystal phase required should be the only stable solid phase.

3) The solubility should undergo a significant change with temperature.

4) The flux should have a low melting point.

5) The flux should have low volatility (in the range from 1 to 10 cP).

6) The flux should have low reactivity with the crucible.

7) The crystals should be easily separable after crystal growth.

8) The flux should be commercially available at a low cost.

9) The flux should have low toxicity.

However, no known flux possesses all of these ideal properties, and most crystals are grown from multiple flux systems. Therefore, a compromise is always necessary, depending on the desired outcome given highest priority, such as the size, quality, or features of the faceted surface.

A common anion or cation often positively influences the growth of high-quality crystals with a large crystal size. This positive influence stems from the enhanced solution chemistry and solubility that result from the close match between the polarizability of the molten flux and that of the final product. For instance, in the study of flux-grown $Ba_5Nb_4O_{15}$ from a $BaCl_2$ flux,[114] the common-ion effect of Ba^{2+} in the solute and flux provides an effective reaction field to facilitate Ostwald ripening, resulting in idiomorphic plate-like $Ba_5Nb_4O_{15}$ crystals up to 50 μm in size.

The presence of a different anion or cation raises the possibility of incorporation of impurities into the product crystals. However, a different anion or cation can also contribute to lowering the viscosity of the flux or to building crystals with faceted surface features. For instance, the addition of monovalent ions, such as alkali ions, into B_2O_3 to form $Na_2B_4O_7$ ($Na_2O + 2B_2O_3$)[115] is known to greatly lower its viscosity and promote crystal growth from a B_2O_3-based flux. This is due to the disruption of the glassy network of B_2O_3. In the growth of crystals with faceted surface features, a different anion or cation may act as a capping agent. This strategy is well-known in the growth of nanocrystals such as nanorods and nanobelts.[116] For example, $Li(Ni_{1/3}Co_{1/3}Mn_{1/3})O_2$ crystals[117] and cube-like $BaTaO_2N$ crystals[118] bound by {003}, {101}, and {111} facets were successfully grown from Na_2SO_4 and KCl fluxes, respectively. This success may be a consequence of the capping effect; *i.e.*, the foreign ions Na^+ and K^+ may act as capping agents, attaching to certain facets and blocking their growth. Note that the capping effect in the field of flux growth is still not well understood.

In this study, I focus on investigating the effects of alkali-based salt fluxes on the growth of functional crystals. The melting point of alkali-based salts, including alkali nitrates, alkali hydroxides, alkali chlorides, alkali carbonates, and alkali sulfates, as reported in the *Molten Salts Handbook*, are summarized in **Table 1.3**.[119]

Table 1.3. Melting Points and Characteristics of Alkali-Based Salts

Alkali-based salts		Melting point (°C)
Nitrates	$LiNO_3$	254
	$NaNO_3$	310
	KNO_3	337
Hydroxides	LiOH	462
	NaOH	318
	KOH	360
Chlorides	LiCl	610
	NaCl	808
	KCl	772
Carbonates	Li_2CO_3	735
	Na_2CO_3	854
	K_2CO_3	896
Sulfates	Li_2SO_4	859
	Na_2SO_4	884
	K_2SO_4	1074

Abundant empirical data indicate that when the cations in alkali-based salts are the same, and the reaction temperatures are near the melting point of various salts, the solubilizing power of metal oxides increases in the order chlorides < nitrates < carbonates ≈ sulfates < hydroxides. This phenomenon can be explained through the Lux-Flood theory. Ionic melts are often studied as solvents for Lux-Flood acid-base reactions.

The Lux-Flood theory is a well-known acid-base theory of oxides. The advantage of this theory is that there is not an implicit theoretical assumption regarding the way in which the oxygen ion is bound to the cation.[120] On the other hand, the limitation of this theory is that it excludes the possibility of regarding the analogous reactions of the sulfide and fluoride ions as acid-base reactions.[120] In the Lux-Flood theory, the acid is defined as an O^{2-} acceptor, whereas the base is defined as an O^{2-} donor using the formulation[120]

$$\text{Base} \leftrightarrow \text{Acid} + O^{2-}$$

Molten alkali-based oxosalts can be written according to the flux-Flood theory as shown in **Table 1.4**.[120–127]

Table 1.4. Possible O^{2-} Donor Chemical Equation and Donor O^{2-} Percentage per Anion

Possible O^{2-} donor chemical equation	Donor O^{2-} percentage per anion
$4NO_3^-$ (base) ↔ $4NO_2$ (acid) + O_2 + $2O^{2-}$	16.7%
$2OH^-$ (base) ↔ H_2O (acid) + O^{2-}	50.0%
CO_3^{2-} (base) ↔ CO_2 (acid) + O^{2-}	33.3%
$2SO_4^{2-}$ (base) ↔ $2SO_3$ (acid) + $2O^{2-}$	25.0%

Different anions exhibit different abilities to act as O^{2-} donors. For instance, 50.0% of the oxygen in OH^- can be released as donor O^{2-}, whereas in the case of NO_3^-, only 16.7% of the oxygen can be used for donor O^{2-}. Griffith *et al.*[128] have used DFT to demonstrate that the addition of nitrate ions into a carbonate melt can increase and maintain oxidizing species such as oxygen, superoxide, and peroxide ions in the melt system.

When the anions are the same and the holding temperatures are in the vicinity of the melting points of various salts, large alkali-metal cations are superior to smaller alkali-metal cations in solvating and maintaining O^{2-}; *i.e.*, K > Na > Li.[124,125]

1.3 Objective

The objective of this study is to use the flux method to grow ion-exchange crystals with 2D or 3D nanostructured channels and to understand the manner in which growth occurs from fluxes. The target crystals in this study are $Li_5La_3Ta_2O_{12}$, Li_2TiO_3, and $KTiNbO_5$. $Li_5La_3Ta_2O_{12}$ is a compound from the garnet family. It is well known as a solid electrolyte in all-solid-state LIBs, because of its three-dimensional Li-ion pathway and high chemical stability. β-Li_2TiO_3 has diverse applications because of its superior tritium diffusion and lithium-ion intercalation properties. The lithium-ion diffusion paths in β-Li_2TiO_3 are provided by a mixture of 1D and 2D nanostructural channels. $KTiNbO_5$ has been widely used in many fields but not as an ion-exchange material. It is composed of two different MO_6 (M = Ti or Nb) metalate layers of octahedra that share edges. All potassium cations are located in the corner of the gallery to compensate for the negatively charged frameworks. $KTiNbO_5$ has a 2D ion-diffusion nanostructural channel.

Conventionally, these target crystals are prepared using solid-state reactions, sol-gel methods, and hydrothermal methods. The properties of crystals, such as their size, surface area, crystallinity, and framework, play a substantial role in the ion-exchange properties of inorganic materials. Therefore, shape- and/or size-controlled crystals of high crystallinity are required. The flux growth method is a solution growth method in which shape- and/or size-controlled crystal growth is possible through the selection of an appropriate flux and/or additives for the flux reaction system. In this study, $Li_5La_3Ta_2O_{12}$ crystals, Li_2TiO_3 crystals and $KTiNbO_5$ crystals are first grown from a flux. Their manner of growth is then discussed on the basis of the experimental results. Finally, their ion-exchange properties are investigated.

1.4 Outline

Chapter 1 begins with a general introduction of the chemical composition, crystallinity, nanostructure, shape of the crystal, and morphology of the material—properties that affect the applications of inorganic ion-exchangeable oxides. This chapter also introduces the flux method that I will use to prepare ion-exchangers in this thesis. Finally, my overall research objectives are summarized.

Chapter 2 describes a low-temperature growth of idiomorphic $Li_5La_3Ta_2O_{12}$ single crystals, which have a 3D lithium diffusion pathway, as a function of the holding temperature and time, cooling rate, flux type, and the solute concentration. The results reveal a unique manner of growth.

Chapter 3 presents the flux growth of β-Li_2TiO_3 crystals, which also have a 3D lithium diffusion pathway, under different conditions. The results demonstrate the efficient anisotropic growth of {001}-faceted β-Li_2TiO_3 single crystals from a sodium-based oxysalt flux.

Chapter 4 presents a combined experimental and computational study of $KTiNbO_5$ with a 2D layered structure as a selective and durable adsorbent for Sr^{2+} ions. $KTiNbO_5$ is grown from a nitrate flux via a solid-state reaction. The Sr^{2+}-adsorption properties of

$KTiNbO_5$ are experimentally investigated. The origin of the high selectivity for Sr^{2+} is studied by density functional theory.

Finally, **Chapter 5** summarizes this research and presents conclusions as well as future perspectives.

References

(1) Robinson, B. *Ion-Exchange Minerals and Disposal of Radioactive Wastes A Survey of Literature*; 1962.

(2) Liu, X. D.; Lu, X. C. A Thermodynamic Understanding of Clay-Swelling Inhibition by Potassium Ions. *Angew. Chem. Int. Ed.* **2006**, *45* (38), 6300–6303.

(3) Sen Gupta, S.; Bhattacharyya, K. G. Adsorption of Metal Ions by Clays and Inorganic Solids. *RSC Adv.* **2014**, *4* (54), 28537–28586.

(4) Rahman, R. O. A.; Ibrahium, H. A.; Hung, Y.-T. Liquid Radioactive Wastes Treatment: A Review. *Water* **2011**, *3* (4), 551–565.

(5) El-Kamash, A. M. Evaluation of Zeolite A for the Sorptive Removal of Cs^{+} and Sr^{2+} Ions from Aqueous Solutions Using Batch and Fixed Bed Column Operations. *J. Hazard. Mater.* **2008**, *151* (2–3), 432–445.

(6) Kodama, T.; Harada, Y.; Ueda, M.; Shimizu, K. I.; Shuto, K.; Komarneni, S. Selective Exchange and Fixation of Strontium Ions with Ultrafine Na-4-Mica. *Langmuir* **2001**, *17* (16), 4881–4886.

(7) García-Sosa, I.; Solache-Ríos, M. Cation-Exchange Capacities of Zeolites A, X, Y, ZSM-5 and Mexican Erionite Compared with the Retention of Cobalt and Cadmium. *J. Radioanal. Nucl. Chem.* **2001**, *250* (1), 205–206.

(8) Turner, S.; Buseck, P. R. Todorokites: A New Family of Naturally Occurring Manganese Oxides. *Science* **1981**, *212* (4498), 1024–1027.

(9) Ooi, K. Preparation of Manganese Oxide Porous Crystals and Their Ion-Sieve Properties. *J. Ion Exch.* **2001**, *12*, 47–56.

(10) Li, Y. F.; Zhu, S. C.; Liu, Z. P. Reaction Network of Layer-to-Tunnel Transition of MnO_2. *J. Am. Chem. Soc.* **2016**, *138* (16), 5371–5379.

(11) Rowsell, J. L. C.; Taylor, N. J.; Nazar, L. F. Structure and Ion Exchange Properties of a New Cobalt Borate with a Tunnel structure "Templated" by Na^{+}. *J. Am. Chem. Soc.* **2002**, *124* (23), 6522–6523.

(12) Yang, D.; Zheng, Z.; Yuan, Y.; Liu, H.; Waclawik, E. R.; Ke, X.; Xie, M.; Zhu, H. Sorption Induced Structural Deformation of Sodium Hexa-Titanate

Nanofibers and Their Ability to Selectively Trap Radioactive Ra(II) Ions from Water. *Phys. Chem. Chem. Phys.* **2010**, *12*, 1271–1277.

(13) Nyman, M.; Tripathi, A.; Parise, J. B.; Maxwell, R. S.; Nenoff, T. M. Sandia Octahedral Molecular Sieves (SOMS): Structural and Property Effects of Charge-Balancing the M^{IV}-Substituted (M = Ti, Zr) Niobate Framework. *J. Am. Chem. Soc.* **2002**, *124* (8), 1704–1713.

(14) Sun, J.; Liu, L.; Zhao, X.; Yang, S.; Komarneni, S.; Yang, D. Capture of Radioactive Cations from Water Using Niobate Nanomaterials with Layered and Tunnel Structures. *RSC Adv.* **2015**, *5* (92), 75354–75359.

(15) Shi, X.; Zhou, D.; Zhang, Z.; Yu, L.; Xu, H.; Chen, B.; Yang, X. Synthesis and Properties of $Li_{1.6}Mn_{1.6}O_4$ and Its Adsorption Application. *Hydrometallurgy* **2011**, *110* (1–4), 99–106.

(16) Xiao, J.-L.; Sun, S.-Y.; Wang, J.; Li, P.; Yu, J.-G. Synthesis and Adsorption Properties of $Li_{1.6}Mn_{1.6}O_4$ Spinel. *Ind. Eng. Chem. Res.* **2013**, *52* (34), 11967–11973.

(17) Ooi, K.; Sakakihara, J. Mechanism of Li^+ Insertion in Spinel-Type Manganese Oxide. Redox and Ion-Exchange Reactions. *Langmuir* **1991**, *7*, 1167–1171.

(18) Yu, C.-L.; Wang, F.; Cao, S.-Y.; Gao, D.-P.; Hui, H.-B.; Guo, Y.-Y.; Wang, D.-Y. The Structure of H_2TiO_3 —a Short Discussion on "Lithium Recovery from Salt Lake Brine by H_2TiO_3." *Dalt. Trans.* **2015**, *44* (35), 15721–15724.

(19) Chitrakar, R.; Makita, Y.; Ooi, K.; Sonoda, A. Lithium Recovery from Salt Lake Brine by H_2TiO_3. *Dalton Trans.* **2014**, *43* (23), 8933–8939.

(20) Yang, X.; Makita, Y.; Hosokawa, J.; Sakane, K.; Ooi, K. Preparation and Alkali Metal Ion Exchange Properties of Protnated $Rb_8Nb_{22}O_{59}$ Compound. *Chem. Mater.* **2005**, *17*, 5420–5427.

(21) Kumada, N.; Takagi, M.; Kinomura, N. Ion-Exchange Reaction of Rubidium Ion in $Rb_8Nb_{22}O_{59}$. *Chem. Lett.* **1996**, *25* (11), 989–990.

(22) Fourquet, J. L.; Gillet, P. A.; Le Bail, A. Li^+/H^+ Topotactic Exchange on $LiSbO_3$: The Series $Li_{1-X}H_XSbO_3$ ($0 \leq X \leq 1$). *Mater. Res. Bull.* **1989**, *24* (10), 1207–1214.

(23) Nalbandyan, V. B.; Avdeev, M.; Pospelov, A. A. Ion Exchange Reactions of

$NaSbO_3$ and Morphotropic Series $MSbO_3$. *Solid State Sci.* **2006**, *8* (12), 1430–1437.

(24) Gómez-Morales, J.; Iafisco, M.; Delgado-López, J. M.; Sarda, S.; Drouet, C. Progress on the Preparation of Nanocrystalline Apatites and Surface Characterization: Overview of Fundamental and Applied Aspects. *Prog. Cryst. Growth Charact. Mater.* **2013**, *59* (1), 1–46.

(25) Minh, D. P.; Tran, N. D.; Nzihou, A.; Sharrock, P. Hydroxyapatite Gel for the Improved Removal of Pb^{2+} Ions from Aqueous Solution. *Chem. Eng. J.* **2013**, *232*, 128–138.

(26) Suzuki, T.; Kyoichi, I.; Miyake, M. Synthetic Hydroxyapatites as Inorganic Cation Exchangers. Part 3.—Exchange Characteristics of Lead Ions (Pb^{2+}). *J. Chem. Soc. Faraday Trans. 1 Phys. Chem. Condens. Phases* **1984**, *80* (11), 3157–3165.

(27) Guang, C.; Hong, H. G.; Mallouk, T. E. Layered Metal Phosphates and Phosphonates - From Crystals To Monolayers. *Acc. Chem. Res.* **1992**, *25* (9), 420–427.

(28) Costantino, U. Novel Layered Materials : Phosphates. *Ion Exch.* **1997**, 1595–1610.

(29) Cheetham, A.; Férey, G.; Loiseau, T. Open Framework Inorganic Materials. *Angew. Chemie Int. Ed.* **1999**, *38* (22), 3268–3292.

(30) Pinus, I. Y.; Stenina, I. A.; Veresov, A. G.; Yaroslavtsev, A. B. Kinetics of H^+/Na^+ Ion Exchange on $H_{1\pm x}Zr_{2-x}M_x(PO_4)_3$ (M = Y or Nb) NASICON Materials. *Russ. J. Inorg. Chem.* **2008**, *53* (2), 181–185.

(31) Hirose, N.; Kuwano, J. Ion-Exchange Properties of NASICON-Type Phosphates with the Frameworks $[Ti_2(PO_4)_3]$ and $[Ti_{1.7}Al_{0.3}(PO_4)_3]$. *J. Mater. Chem.* **1994**, *4* (1), 9–12.

(32) Ying, Y.; Liu, Y.; Wang, X.; Mao, Y.; Cao, W.; Hu, P.; Peng, X. Two-Dimensional Titanium Carbide for Efficiently Reductive Removal of Highly Toxic chromium(VI) from Water. *ACS Appl. Mater. Interfaces* **2015**, *7* (3), 1795–1803.

(33) Ren, C. E.; Hatzell, K. B.; Alhabeb, M.; Ling, Z.; Mahmoud, K. A.; Gogotsi, Y. Charge- and Size-Selective Ion Sieving Through $Ti_3C_2T_x$ MXene Membranes. *J. Phys. Chem. Lett.* **2015**, *6* (20), 4026–4031.

(34) Ghidiu, M.; Halim, J.; Kota, S.; Bish, D.; Gogotsi, Y.; Barsoum, M. W. Ion-Exchange and Cation Solvation Reactions in Ti_3C_2 MXene. *Chem. Mater.* **2016**, *28* (10), 3507–3514.

(35) Manos, M. J.; Kanatzidis, M. G. Highly Efficient and Rapid Cs^+ Uptake by the Layered Metal Sulfide $K_{2x}Mn_xSn_{3-x}S_6$ (KMS-1). *J. Am. Chem. Soc.* **2009**, *6* (7), 6599–6607.

(36) Mertz, J. L.; Fard, Z. H.; Malliakas, C. D.; Manos, M. J.; Kanatzidis, M. G. Selective Removal of Cs^+, Sr^{2+}, and Ni^{2+} by $K_{2x}Mg_xSn_{3-x}S_6$ (X = 0.5-1) (KMS-2) Relevant to Nuclear Waste Remediation. *Chem. Mater.* **2013**, *25* (10), 2116–2127.

(37) Sarma, D.; Malliakas, C. D.; Subrahmanyam, K. S.; Islam, S. M.; Kanatzidis, M. $K_{2x}Sn_{4-x}S_{8-x}$ (x=0.65-1): A New Metal Sulfide for Rapid and Selective Removal of Cs^+, Sr^{2+} and UO_2^{2+} Ions. *Chem. Sci.* **2016**, *7*, 1121–1132.

(38) Halajnia, A.; Oustan, S.; Najafi, N.; Khataee, A. R.; Lakzian, A. Adsorption–desorption Characteristics of Nitrate, Phosphate and Sulfate on Mg–Al Layered Double Hydroxide. *Appl. Clay Sci.* **2013**, *80–81*, 305–312.

(39) Tezuka, S.; Chitrakar, R.; Sonoda, A.; Ooi, K.; Tomida, T. Studies on Selective Adsorbents for Oxo-Anions. NO_3^- Adsorptive Properties of Ni-Fe Layered Double Hydroxide in Seawater. *Adsorption* **2005**, *11*, 751–755.

(40) Smit, J. van R.; Robb, W.; Jacobs, J. J. Cation Exchange on Ammonium molybdophosphate - I: The Alkali Metals. *J. Inorg. Nucl. Chem.* **1959**, *12* (1–2), 104–112.

(41) Smit, J. V. R.; Robb, W. Ion Exchange on Ammonium Molybdophosphate-II Bivalent and Trivalent Ions. *J. Inorg. Nucl. Chem.* **1964**, *26* (9), 509–518.

(42) R. Smit, J.; Jacobs, J. J.; Robb, W. Cation Exchange Properties of the Ammonium Heteropolyacid Salts. *J. Inorg. Nucl. Chem.* **1959**, *12* (1), 95–103.

(43) Bennett, M. V.; Shores, M. P.; Beauvais, L. G.; Long, J. R. Expansion of the

Porous Solid $Na_2Zn_3[Fe(CN)_6]_2$ $9H_2O$: Enhanced Ion- Exchange Capacity in $Na_2Zn_3[Re_6Se_8(CN)_6$ $24H_2O$. *J. Am. Chem. Soc.* **2000**, *122* (28), 6664–6668.

(44) Vlasselaer, S.; D'olieslager, W.; D'hont, M. Caesium Ion Exchange Equilibrium on Potassium-Zinc-hexacyanoferrate(II), $K_2Zn_3[Fe(CN)_6]_2$. *J. Inorg. Nucl. Chem.* **1976**, *38* (2), 327–330.

(45) MIMURA, H.; SAKAKIBARA, T.; NIIBORI, Y.; TANAKA, K. Selective Uptake of Palladium by Insoluble Ferrocyanides. *J. Ion Exch.* **2005**, *16* (1), 29–33.

(46) Shen, X.; Ding, Y.; Liu, J.; Laubernds, K.; Zerger, R. P.; Polverejan, M.; Son, Y. C.; Aindow, M.; Suib, S. L. Synthesis, Characterization, and Catalytic Applications of Manganese Oxide Octahedral Molecular Sieve (OMS) Nanowires with a 2 × 3 Tunnel Structure. *Chem. Mater.* **2004**, *16* (25), 5327–5335.

(47) Tsuji, M.; Abe, M.; Tanaka, Y.; Tanaka, Y. Ion-Exchange Selectivity for Alkali Metal Ions on a Hydrous Manganese Dioxide with a Tunnel Structure. *Seventh Symp. salt* **1993**, *28*, 23–28.

(48) Tsuda, M.; Arai, H.; Nemoto, Y.; Sakurai, Y. Electrode Performance of Romanechite for Rechargeable Lithium Batteries. *J. Power Sources* **2001**, *102* (1–2), 135–138.

(49) Tian, Z. Manganese Oxide Mesoporous Structures: Mixed-Valent Semiconducting Catalysts. *Science* **1997**, *276* (5314), 926–930.

(50) Brock, S. L.; Duan, N.; Tian, Z. R.; Giraldo, O.; Zhou, H.; Suib, S. L. A Review of Porous Manganese Oxide Materials. *Chem. Mater.* **1998**, *10* (10), 2619–2628.

(51) Andersson, S.; Wadsley, A. D. The Structures of $Na_2Ti_6O_{13}$ and $Rb_2Ti_6O_{13}$ and the Alkali Metal Titanates. *Acta Crystallogr.* **1962**, *15* (3), 194–201.

(52) Mitchell, R. H.; Burns, P. C.; Knight, K. S.; Howard, C. J.; Chakhmouradian, A. R. Observations on the Crystal Structures of Lueshite. *Phys. Chem. Miner.* **2014**, *41* (6), 393–401.

(53) Rudola, A.; Saravanan, K.; Devaraj, S.; Gong, H.; Balaya, P. $Na_2Ti_6O_{13}$: A Potential Anode for Grid-Storage Sodium-Ion Batteries. *Chem. Commun.* **2013**,

49 (67), 7451.

(54) Vázquez-Cuchillo, O.; Gómez, R.; Cruz-López, A.; Torres-Martínez, L. M.; Zanella, R.; Sandoval, F. J. A.; Ángel-Sánchez, K. Del. Improving Water Splitting Using RuO_2-Zr/$Na_2Ti_6O_{13}$ as a Photocatalyst. *J. Photochem. Photobiol. A Chem.* **2013**, *266*, 6–11.

(55) Xu, H.; Nyman, M.; Nenoff, T. M.; Navrotsky, A. Prototype Sandia Octahedral Molecular Sieve (SOMS) $Na_2Nb_2O_6$ H_2O: Synthesis, Structure and Thermodynamic Stability. *Chem. Mater.* **2004**, *16*, 2034–2040.

(56) Smrčok, Ľ.; Tunega, D.; Ramirez-Cuesta, A. J.; Scholtzová, E. The Combined Inelastic Neutron Scattering and Solid State DFT Study of Hydrogen Atoms Dynamics in a Highly Ordered Kaolinite. *Phys. Chem. Miner.* **2010**, *37* (8), 571–579.

(57) Benazzouz, B. K.; Zaoui, A. A Nanoscale Simulation Study of the Elastic Behaviour in Kaolinite Clay under Pressure. *Mater. Chem. Phys.* **2012**, *132* (2–3), 880–888.

(58) Gournis, D.; Lappas, A.; Karakassides, M. A.; Többens, D.; Moukarika, A. A Neutron Diffraction Study of Alkali Cation Migration in Montmorillonites. *Phys. Chem. Miner.* **2008**, *35* (1), 49–58.

(59) Gualtieri, A. F. Accuracy of XRPD QPA Using the Combined Rietveld-RIR Method. *J. Appl. Crystallogr.* **2000**, *33* (2), 267–278.

(60) Hervieu, M.; Raveau, B. A Layer Structure: The Titanoniobate $CsTi_2NbO_7$. *J. Solid State Chem.* **1980**, *32* (2), 161–165.

(61) Catti, M.; Pinus, I.; Scherillo, A. On the Crystal Energy and Structure of $A_2Ti_nO_{2n+1}$ (A = Li, Na, K) Titanates by DFT Calculations and Neutron Diffraction. *J. Solid State Chem.* **2013**, *205*, 64–70.

(62) Andersson, S.; Wadsley, A. D. The Crystal Structure of $Na_2Ti_3O_7$. *Acta Crystallogr.* **1961**, *14* (12), 1245–1249.

(63) Gasperin, M. Structure du triniobate(V) de Potassium KNb_3O_8, un Niobate Lamellaire. *Acta Crystallogr. Sect. B* **1982**, *38* (7), 2024–2026.

(64) Ogawa, M.; Kuroda, K. Photofunctions of Intercalation Compounds. *Chem. Rev.*

1995, *95* (2), 399–438.

(65) Kudo, A.; Miseki, Y. Heterogeneous Photocatalyst Materials for Water Splitting. *Chem. Soc. Rev.* **2009**, *38*, 253–278.

(66) Kudo, A.; Tanaka, A.; Domen, K.; Maruya, K. ichi; Aika, K. ichi; Onishi, T. Photocatalytic Decomposition of Water over $NiOK_4Nb_6O_{17}$ Catalyst. *J. Catal.* **1988**, *111* (1), 67–76.

(67) Clearfield, A. Role of Ion Exchange in Solid-State Chemistry. *Chem.Rev.* **1988**, *88*, 125–148.

(68) Capel, F.; Moure, C.; Villegas, M.; Ferna, Â. F. Processing and Dielectric Properties of the Mixed-Layer Bismuth Titanate Niobate $Bi_7Ti_4NbO_{21}$ by the Metal-Organic Precursor Synthesis Method. *J. Eur. Ceram. Soc.* **2001**, *21*, 1–8.

(69) Manos, M. J.; Kanatzidis, M. G. Layered Metal Sulfides Capture Uranium from Seawater. *J. Am. Chem. Soc.* **2012**, *134* (39), 16441–16446.

(70) Manos, M. J.; Ding, N.; Kanatzidis, M. G. Layered Metal Sulfides: Exceptionally Selective Agents for Radioactive Strontium Removal. *Proc. Natl. Acad. Sci. U. S. A.* **2008**, *105* (10), 3696–3699.

(71) Belloto Maurizio; Bernadette, R.; Olivier, C.; John, L.; Dominique, B.; Elkaim, E. A Reexamination of Hydrotalcite Chemistry. *J. Phys. Chem.* **1996**, *100* (20), 8527–8534.

(72) Zümreoglu-Karan, B.; Ay, A. N. Layered Double Hydroxides — Multifunctional Nanomaterials. *Chem. Pap.* **2011**, *66* (1), 1–10.

(73) Wang, Q.; O'Hare, D. Recent Advances in the Synthesis and Application of Layered Double Hydroxide (LDH) Nanosheets. *Chem. Rev.* **2012**, *112* (7), 4124–4155.

(74) Iguchi, S.; Teramura, K.; Hosokawa, S.; Tanaka, T. Photocatalytic Conversion of CO_2 in an Aqueous Solution Using Various Kinds of Layered Double Hydroxides. *Catal. Today* **2015**, *251*, 140–144.

(75) Goh, K.-H.; Lim, T.-T.; Dong, Z. Application of Layered Double Hydroxides for Removal of Oxyanions: A Review. *Water Res.* **2008**, *42* (6–7), 1343–1368.

(76) Bi, X.; Zhang, H.; Dou, L. Layered Double Hydroxide-Based Nanocarriers for

Drug Delivery. *Pharmaceutics* **2014**, *6* (2), 298–332.

(77) Del Hoyo, C. Layered Double Hydroxides and Human Health: An Overview. *Appl. Clay Sci.* **2007**, *36* (1–3), 103–121.

(78) Tonelli, D.; Scavetta, E.; Giorgetti, M. Layered-Double-Hydroxide-Modified Electrodes: Electroanalytical Applications. *Anal. Bioanal. Chem.* **2013**, *405* (2–3), 603–614.

(79) Wang, Q.; Ohare, D. Recent Advances in the Synthesis and Application of Layered Double Hydroxide (LDH) Nanosheets. *Chem. Rev.* **2012**, *112* (7), 4124–4155.

(80) Naguib, M.; Mochalin, V. N.; Barsoum, M. W.; Gogotsi, Y. 25th Anniversary Article: MXenes: A New Family of Two-Dimensional Materials. *Adv. Mater.* **2014**, *26* (7), 992–1005.

(81) Naguib, M.; Kurtoglu, M.; Presser, V.; Lu, J.; Niu, J.; Heon, M.; Hultman, L.; Gogotsi, Y.; Barsoum, M. W. Two-Dimensional Nanocrystals Produced by Exfoliation of Ti_3AlC_2. *Adv. Mater.* **2011**, *23* (37), 4248–4253.

(82) Yanagida, R. Y.; Amaro, A. A.; Seff, K. Redetermination of the Crystal Structure of Dehydrated Zeolite 4A. *J. Phys. Chem.* **1973**, *77* (6), 805–809.

(83) Boilot, J. P.; Collin, G.; Colomban, P. Relation Structure-Fast Ion Conduction in the NASICON Solid Solution. *J. Solid State Chem.* **1988**, *73* (1), 160–171.

(84) Song, W.; Ji, X.; Wu, Z.; Zhu, Y.; Yang, Y.; Chen, J.; Jing, M.; Li, F.; Banks, C. E. First Exploration of Na-Ion Migration Pathways in the NASICON Structure $Na_3V_2(PO_4)_3$. *J. Mater. Chem. A* **2014**, *2* (15), 5358.

(85) Ohzuku, T.; Takeda, S.; Iwanaga, M. Solid-State Redox Potentials for $Li[Me_{1/2}Mn_{3/2}]O_4$ (Me: 3d-Transition Metal) Having Spinel-Framework Structures: A Series of 5 Volt Materials for Advanced Lithium-Ion Batteries. *J. Power Sources* **1999**, *81–82*, 90–94.

(86) Amdouni, N.; Zaghib, K.; Gendron, F.; Mauger, A.; Julien, C. M. Structure and Insertion Properties of Disordered and Ordered $LiNi_{0.5}Mn_{1.5}O_4$ Spinels Prepared by Wet Chemistry. *Ionics (Kiel).* **2006**, *12* (2), 117–126.

(87) Gao, P.; Wang, L.; Chen, L.; Jiang, X.; Pinto, J.; Yang, G. Microwave Rapid

Preparation of $LiNi_{0.5}Mn_{1.5}O_4$ and the Improved High Rate Performance for Lithium-Ion Batteries. *Electrochim. Acta* **2013**, *100*, 125–132.

(88) Santhanam, R.; Rambabu, B. Research Progress in High Voltage Spinel $LiNi_{0.5}Mn_{1.5}O_4$ Material. *J. Power Sources* **2010**, *195* (17), 5442–5451.

(89) Ziebarth, B.; Klinsmann, M.; Eckl, T.; Elsässer, C. Lithium Diffusion in the Spinel Phase $Li_4Ti_5O_{12}$ and in the Rocksalt Phase $Li_7Ti_5O_{12}$ of Lithium Titanate from First Principles. *Phys. Rev. B - Condens. Matter Mater. Phys.* **2014**, *89* (17), 1–7.

(90) Sun, X.; Radovanovic, P. V.; Cui, B. Advances in Spinel $Li_4Ti_5O_{12}$ Anode Materials for Lithium-Ion Batteries. *New J. Chem.* **2015**, *39* (1), 38–63.

(91) Zhao, B.; Ran, R.; Liu, M.; Shao, Z. A Comprehensive Review of $Li_4Ti_5O_{12}$-Based Electrodes for Lithium-Ion Batteries: The Latest Advancements and Future Perspectives. *Mater. Sci. Eng. R Reports* **2015**, *98*, 1–71.

(92) Aldon, L.; Kubiak, P.; Womes, M.; Jumas, J. C.; Olivier-Fourcade, J.; Tirado, J. L.; Corredor, J. I.; Pérez Vicente, C. Chemical and Electrochemical Li-Insertion into the $Li_4Ti_5O_{12}$ Spinel. *Chem. Mater.* **2004**, *16* (11), 5721–5725.

(93) Xia, Y.; Xia, X.; Peng, H. C. Shape-Controlled Synthesis of Colloidal Metal Nanocrystals: Thermodynamic versus Kinetic Products. *J. Am. Chem. Soc.* **2015**, *137* (25), 7947–7966.

(94) Grzelczak, M.; Perez-Juste, J.; Mulvaney, P.; Liz-Marzan, L. M. Shape Control in Gold Nanoparticle Synthesis. *Chem Soc Rev* **2008**, *37* (9), 1783–1791.

(95) Xia, Y.; Xiong, Y.; Lim, B.; Skrabalak, S. E. Shape-Controlled Synthesis of Metal Nanocrystals: Simple Chemistry Meets Complex Physics? *Angew. Chemie - Int. Ed.* **2009**, *48* (1), 60–103.

(96) Katsuyama, T.; Hiruma, K.; Ogawa, K.; Odom, T. W.; Lieber, C. M.; Werner, P.; Zacharias, M.; Ellis, W. C.; Schmidt, V.; Senz, S. Synthesis of Tetrahexahedral Platinum Nanocrystals with High-Index Facets and High Electro-Oxidation Activity. *science* **2007**, 732–735.

(97) Xia, Y. N.; Yang, P. D.; Sun, Y. G.; Wu, Y. Y.; Mayers, B.; Gates, B.; Yin, Y. D.; Kim, F.; Yan, Y. Q.; Xia, B. Y. One-Dimensional Nanostructures: Synthesis,

Characterization, and Applications. *Adv. Mater.* **2003**, *15* (5), 353–389.

(98) International Atomic Energy Agency. *Application of Ion Exchange Processes for the Treatment of Radioactive Waste and Management of Spent Ion Exchangers*; 2002.

(99) Lv, R.; Robinson, J. A.; Schaak, R. E.; Sun, D.; Sun, Y.; Mallouk, T. E.; Terrones, M. Transition Metal Dichalcogenides and beyond: Synthesis, Properties, and Applications of Single- and Few-Layer Nanosheets. *Acc. Chem. Res.* **2015**, *48* (1), 56–64.

(100) Arthur, J. R. Molecular Beam Epitaxy. *Surf. Sci.* **2002**, *500* (1–3), 189–217.

(101) Scheel, H. J. Historical Aspects of Crystal Growth Technology. *J. Cryst. Growth* **2000**, *211* (1), 1–12.

(102) Burda, C.; Chen, X.; Narayanan, R. Chemistry and Properties of Nanocrystals of Different Shapes. *Chem. Rev.* **2005**, *105* (4), 2–5.

(103) Ueltzen, M. The Verneuil Flame Fusion Process: Substances. *J. Cryst. Growth* **1993**, *132* (1–2), 315–328.

(104) Kang, S. J. L.; Park, J. H.; Ko, S. Y.; Lee, H. Y. Solid-State Conversion of Single Crystals: The Principle and the State-of-the-Art. *J. Am. Ceram. Soc.* **2015**, *98* (2), 347–360.

(105) Elwell, D.; Schell, H. J. *Crystal Growth from High-Temperature Solutions*; London, New York, San Francisco, 2011.

(106) Hayashi, F.; Shirasaki, A.; Wagata, H.; Kamikawa, H.; Aoki, Y.; Oishi, S.; Teshima, K. Flux-Assisted Fabrication of Vertically Aligned Layered Double Hydroxide Plates on in Situ Formed Alumina Particles. *Cryst. Growth Des.* **2015**, *15* (2), 732–736.

(107) Teshima, K.; Lee, S. H.; Sakurai, M.; Kameno, Y.; Yubuta, K.; Suzuki, T.; Shishido, T.; Endo, M.; Oishi, S. Well-Formed One-Dimensional Hydroxyapatite Crystals Grown by an Environmentally Friendly Flux Method. *Cryst. Growth Des.* **2009**, *9* (6), 2937–2940.

(108) Kurihara, M.; Hayashi, F.; Shimizu, K.; Wagata, H.; Hirano, T.; Nakajima, Y.; Yubuta, K.; Oishi, S.; Teshima, K. Flux-Boosted Sulfide Crystal Growth:

Growth of $CuInS_2$ Crystals by NaCl-$InCl_3$ Evaporation. *Cryst. Growth Des.* **2016**, *16* (3), 1195–1199.

(109) Teshima, K.; Lee, S.; Mizuno, Y.; Inagaki, H.; Hozumi, M.; Kohama, K.; Yubuta, K.; Shishido, T.; Oishi, S. Environmentally Friendly Growth of Well-Developed $LiCoO_2$ Crystals for Lithium-Ion Rechargeable Batteries Using a NaCl Flux. *Cryst. Growth Des.* **2010**, *10* (10), 4471–4475.

(110) Teshima, K.; Lee, S.; Murakoshi, S.; Suzuki, S. Highly Crystalline, Idiomorphic $Na_2Ti_6O_{13}$ Whiskers Grown from a NaCl Flux at a Relatively Low Temperature. *Eur. J. Inorg. Chem.* **2010**, 2936–2940.

(111) Hayashi, F.; Kurokawa, S.; Shiiba, H.; Wagata, H.; Yubuta, K.; Oishi, S.; Nishikiori, H.; Teshima, K. Exceptional Flux Growth and Chemical Transformation of Metastable Orthorhombic $LiMnO_2$ Cuboids into Hierarchically-Structured Porous $H_{1.6}Mn_{1.6}O_4$ Rods as Li Ion Sieves. *Cryst. Growth Des.* **2016**, *16* (11), 6178–6185.

(112) Wang, Y.; He, J.; Liu, C.; Chong, W. H.; Chen, H. Thermodynamics versus Kinetics in Nanosynthesis. *Angew. Chemie - Int. Ed.* **2015**, *54* (7), 2022–2051.

(113) Bugaris, D.; Loye, H. zur. Materials Discovery by Flux Crystal Growth: Quaternary and Higher Order Oxides. *Angew. Chemie Int. Ed.* **2012**, *51* (16), 3780–3811.

(114) Yamada, T.; Murata, Y.; Wagata, H.; Yubuta, K.; Teshima, K. Facile Morphological Modification of $Ba_5Nb_4O_{15}$ Crystals Using Chloride Flux and in-Situ Growth Investigation. *Cryst. Growth Des.* **2016**, *16* (7), 3954–3960.

(115) Shannon, R. D. Revised Effective Ionic Radii and Systematic Studies of Interatomic Distances in Halides and Chalcogenides. *Acta Crystallogr. Sect. A* **1976**, *32* (5), 751–767.

(116) Bakshi, M. S. How Surfactants Control Crystal Growth of Nanomaterials. *Cryst. Growth Des.* **2016**, *16* (2), 1104–1133.

(117) Kimijima, T.; Zettsu, N.; Teshima, K. Growth Manner of Octahedral-Shaped $Li(Ni_{1/3}Co_{1/3}Mn_{1/3})O_2$ Single Crystals in Molten Na_2SO_4. *Cryst. Growth Des.* **2016**, *16* (5), 2618–2623.

(118) Hojamberdiev, M.; Yubuta, K.; Vequizo, J. J. M.; Yamakata, A.; Oishi, S.; Domen, K.; Teshima, K. NH_3-Assisted Flux Growth of Cube-like $BaTaO_2N$ Submicron Crystals in a Completely Ionized Nonaqueous High-Temperature Solution and Their Water Splitting Activity. *Cryst. Growth Des.* **2015**, *15* (9), 4663–4671.

(119) Janz, G. J. *Molten Salts Handbook*; Academic Press, 1967.

(120) Flood, H.; Förland, T. The Acidic and Basic Properties of Oxides. *Acta Chem. Scand* **1947**, *1*, 592–604.

(121) Freeman, E. S. The Kinetics of the Thermal Decomposition of Sodium Nitrate and of the Reaction between Sodium Nitrite and Oxygen. *J. Am. Chem. Soc.* **1956**, *60*, 1487–1493.

(122) Freeman, E. S. The Kinetics of the Thermal Decomposition of Potassium Nitrate and of the Reaction between Potassium Nitrite and Oxygen. *J. Am. Chem. Soc.* **1957**, *79* (February), 838–841.

(123) Afanasiev, P.; Afanasiev, P.; Geantet, C.; Geantet, C. Synthesis of Solid Materials in Molten Nitrates. *Coord. Chem. Rev.* **1998**, *180*, 1725–1752.

(124) Mugavero, S. J.; Gemmill, W. R.; Roof, I. P.; zur Loye, H.-C. Materials Discovery by Crystal Growth: Lanthanide Metal Containing Oxides of the Platinum Group Metals (Ru, Os, Ir, Rh, Pd, Pt) from Molten Alkali Metal Hydroxides. *J. Solid State Chem.* **2009**, *182* (7), 1950–1963.

(125) Cortese, A. J.; Abeysinghe, D.; Wilkins, B.; Smith, M. D.; Rassolov, V.; zur Loye, H.-C. Oxygen Anion Solubility as a Factor in Molten Flux Crystal Growth, Synthesis, and Characterization of Four New Reduced Lanthanide Molybdenum Oxides: $Ce_{4.918(3)}Mo_3O_{16}$, $Pr_{4.880(3)}Mo_3O_{16}$, $Nd_{4.910(3)}Mo_3O_{16}$, and $Sm_{4.952(3)}Mo_3O_{16}$. *Cryst. Growth Des.* **2016**, *918* (3), 4225–4231.

(126) Cherginets, V. L.; Rebrova, T. P. On Carbonate Ion Dissociation in Molten Alkali Metal Halides at ≈800 ºC. *J. Chem. Eng. Data* **2003**, *48* (3), 463–467.

(127) Cherginets, V. L.; Rebrova, T. P. On The Effect of Ionic Melt Compositions on Their Acid-Base Properties. *Phys. Chem. Liq.* **2001**, *39* (3), 367–381.

(128) Griffiths, T. R.; Volkovich, V. A.; Carper, W. R. The Structures of the Active

Intermediates in Catalyst-Enhanced Molten Salt Oxidation and a New Method for the Complete Destruction of Chemical Warfare Arsenicals. *Struct. Chem.* **2010**, *21* (2), 291–297.

Chapter 2
Low temperature growth of garnet-type $Li_5La_3Ta_2O_{12}$ crystals from LiOH flux

Chapter 2 Low temperature growth of garnet-type $Li_5La_3Ta_2O_{12}$ crystals from LiOH flux

2.1 Introduction

Garnet-type $Li_{5+x}Ln_3M^{IV}_{2-y}M^{V}_{y}O_{12+z}$ (x, y = 0–2, z = 0–1; Ln = La, Pr, Nd; M = Ta, Zr, Nb) compounds function as solid electrolytes in all-solid-state lithium-ion batteries (LIBs), because of their three-dimensional Li-ion pathway and high chemical stability.[1–6] Among these garnets, $Li_{6.75}La_3Zr_{1.75}Ta_{0.25}O_{12}$ shows the highest lithium ion conductivity, ~ 8.7×10^{-4} S·cm^{-1} at room temperature,[7, 8] while the corresponding theoretical value was reported as ~ 1×10^{-2} S·cm^{-1}.[9] This discrepancy could reflect the presence of particle boundary as well as the impurity phases of the $Li_{6.75}La_3Zr_{1.75}Ta_{0.25}O_{12}$ sample.[9] This highlights the need for the underlying method that efficiently grows the garnet-type crystals.

Generally, garnet-type materials are prepared by solid-state reaction (SSR) methods above 800 °C.[9,10] However, the high-temperature synthesis presents environmental and cost issues. Whereas tetragonal $Li_7La_3Zr_2O_{12}$ is commonly prepared by SSR method at 1250 °C, Il'ina and coworkers recently reported the successful synthesis of $Li_7La_3Zr_2O_{12}$ at lower (900 °C) temperature using the citrate-nitrate method, thanks to the intermediate compounds (Li_2ZrO_3, $La_2Zr_2O_7$) formed during the synthesis.[11] This result indicates that suitable intermediates can lower the formation temperature of the target products by altering the reaction path. The flux method, a liquid-phase single crystal growth technique used to prepare inorganic materials, is a promising approach for controlling the final shape of single crystals and to lower reaction temperatures.[12,13] Awaka[14] and Tietz[15] *et al.* reported preparing $Li_7La_3Zr_2O_{12}$ single crystals at around

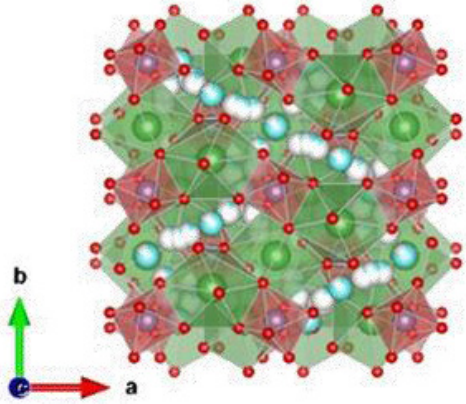

Figure 2.1 Schematic representation of the crystal structure of garnet-type $Li_5La_3Ta_2O_{12}$. Crystal structure of $Li_5La_3Ta_2O_{12}$ is visualized using the VESTA program.

1000 °C in two steps using Li_2CO_3 flux. Kimijima *et al.*[16] successfully grew $Li_7La_3Zr_2O_{12}$ single crystals at 700 °C using LiOH flux in one step. These results indicated that alkali metal hydroxide fluxes were effective for the crystal growth of mixed oxides at low temperatures, due to their low melting point and high solubility behavior.[12,17] I have previously reported the growth of garnet-type $Li_5La_3Nb_2O_{12}$ single crystals at 500 °C by the LiOH flux method.[18] Roof *et al.*[6] also reported the synthesis of $Li_5La_3Ta_2O_{12}$ single crystals using the $LiOH{\cdot}H_2O$ flux method at 600 °C in a closed silver tube. These results indicated that LiOH represent an effective flux to decrease the reaction temperature and form single crystals. Nevertheless, the growth manner of garnet single crystals under such conditions remains unknown.

In this study, garnet-type $Li_5La_3Ta_2O_{12}$ was selected as a model material because of its promising properties as solid electrolyte. The crystal structure is shown in **Figure 2.1**. I explored different LiOH flux growth conditions (involving variable holding temperatures, solute concentrations, holding times, and cooling rates), and analyzed the corresponding formation behavior. The characterization of the species formed at the various stages of the synthesis allowed us to discuss the growth manner. To the best of our knowledge, this is the first work where the formation of idiomorphic $Li_5La_3Ta_2O_{12}$ single crystals is discussed.

2.2 Experimental section

2.2.1 Flux growth of $Li_5La_3Ta_2O_{12}$ crystals

$Li_5La_3Ta_2O_{12}$ crystals were prepared by the flux method. La_2O_3 (99.99%) and Ta_2O_5 (99.9%) powders were used as solutes, whereas $LiOH \cdot H_2O$ (98%) was employed as flux as well as solute. The growth conditions are summarized in **Tables 2.1** and **2.2**. The total mass of all reagents was fixed to approximately 10 g in each run. After mixing, each mixture was put into an alumina crucible with a volume of 30 cm^3. The crucibles were loosely covered with an alumina lid and placed into a programmable furnace, followed by heating at 500 $°C \cdot h^{-1}$ and then holding for 10 h at the respective holding temperature. After heating, the crucibles were cooled to 100 ºC at a cooling rate of 10, 200, or > 9000 $ºC \cdot h^{-1}$ under air. A cooling rate > 9000 $°C \cdot h^{-1}$ indicates that the crucible was immediately removed from the furnace after heating. The products were separated from the remaining flux using hot water (~ 80 ºC).

Table 2.1 Growth Conditions for $Li_5La_3Ta_2O_{12}$ Crystals Grown from LiOH Flux

Run	Holding temp. / ºC	Holding time / h	Solute			Flux	Solute conc. / mol%	Cooling rate / $ºC \cdot h^{-1}$
			LiOH[a] / g	La_2O_3 / g	Ta_2O_5 / g	LiOH[a] / g		
2-1	400	10	1.083	2.522	2.281	4.115	5	200
2-2	500	10	1.083	2.522	2.281	4.115	5	200
2-3	600	10	1.083	2.522	2.281	4.115	5	200
2-4	700	10	1.083	2.522	2.281	4.115	5	200
2-5	800	10	1.083	2.522	2.281	4.115	5	200
2-6	900	10	1.083	2.522	2.281	4.115	5	200
2-7	1000	10	1.083	2.522	2.281	4.115	5	200
2-8	500	10	0.396	0.923	0.834	7.841	1	200
2-9	500	10	1.382	3.219	2.911	2.488	10	200
2-10	500	10	1.604	3.736	3.378	1.283	20	200
2-11	500	10	1.694	3.947	3.568	0.791	30	200
2-12	500	1	1.083	2.522	2.281	4.115	5	200
2-13	500	5	1.083	2.522	2.281	4.115	5	200
2-14	500	20	1.083	2.522	2.281	4.115	5	200

2-15	500	10	1.083	2.522	2.281	4.115	5	10
2-16	500	10	0.396	0.923	0.834	7.841	5	air quenching

[a] $LiOH \cdot H_2O$

Table 2.2 Growth Conditions for $Li_5La_3Ta_2O_{12}$ Crystals Grown from Different Fluxes

Run	Holding temp. / ºC	Holding time / h	Solute			Flux			Solute conc. / mol%	Coolin g rate / ºC·h^{-1}
			LiOH[a] / g	La_2O_3 / g	Ta_2O_5 / g	$LiNO_3$ / g	NaOH / g	KOH / g		
2-17	500	10	1.840	4.285	3.875	0	0	0	100	200
2-18	500	10	0.856	1.994	1.803	5.346	0	0	5	200
2-19	500	10	1.104	2.572	2.325	0	3.999	0	5	200
2-20	500	1	0.951	2.215	2.003	0	0	4.832	5	200

[a] $LiOH \cdot H_2O$

2.2.2 Characterization

Scanning electron microscopy (SEM, JEOL, JCM-5700) images were acquired at an acceleration voltage of 15 kV. The average particle size was calculated over a sample of more than 300 crystals observed in the SEM images. Transmission electron microscopy (TEM, TOPCON, EM-002B) data were obtained at an acceleration voltage of 200 kV. X-ray diffraction (XRD) analyses were performed on a powder diffractometer (RIGAKU, MiniflexII) operating at 30 kV and 20 mA, using Cu Kα radiation (λ = 0.15418 nm). The XRD data for Rietveld refinement were collected in the 2θ range from 5 º to 120 º with a step of 0.012 º on a powder diffractometer (RIGAKU, SmartLab) operating at 40 kV and 40 mA, using Cu Kα radiation (λ = 0.1540593 nm). The whole pattern matching refinements of parameters of samples prepared at 500 ºC and 700 ºC (flux, LiOH; solute concentration, 5 mol%; holding time, 10 h) were carried out using Rietveld analysis PDXL software (RIGAKU).

2.3 Results and discussion

2.3.1 Effect of holding temperature and time

The effect of the holding temperature on crystal growth was first examined with the solute concentration of 5 mol%. **Figure 2.2** shows the XRD patterns of products flux-grown at various temperatures range from 400 to 1000 ºC. At 400 ºC (Run 2-1), no $Li_5La_3Ta_2O_{12}$ phase was obtained and all the diffraction peaks were attributed to $La(OH)_3$ (**Figure 2.2a**), which is formed from the reaction of La_2O_3 with LiOH and the hydration of the remaining La_2O_3 during the washing process with hot water (see **Figure 2.3**).

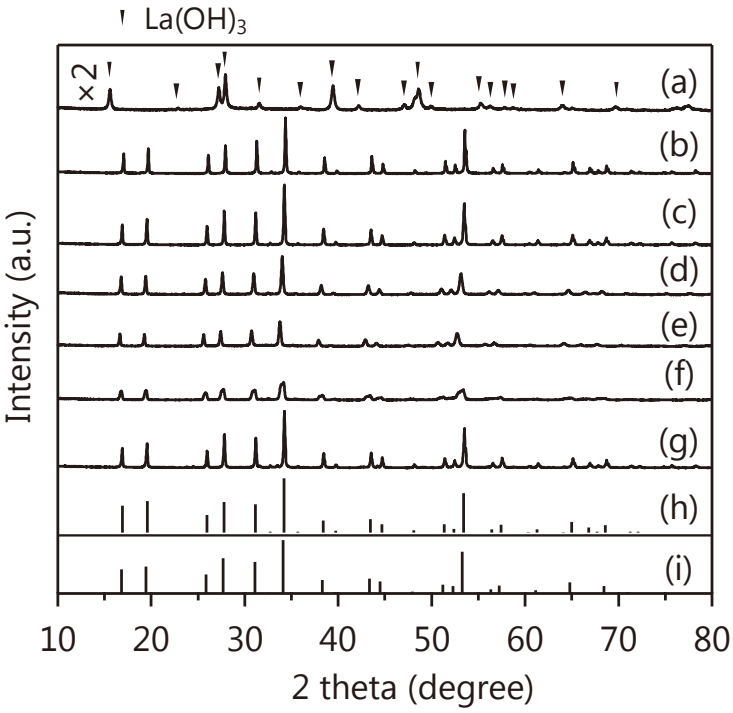

Figure 2.2 XRD patterns of samples prepared at (a) 400 ºC, (b) 500 ºC, (c) 600 ºC, (d) 700 ºC, (e) 800 ºC, (f) 900 ºC, and (g) 1000 ºC. Flux, LiOH; solute concentration, 5 mol%; holding time, 10 h. The patterns in (h) and (i) are the Powder Diffraction File (PDF) patterns of $Li_5La_3Ta_2O_{12}$ (# 45-0110) and $Li_7La_3Ta_2O_{13}$ (# 39-0898) taken from the International Centre for Diffraction Data (ICDD) database.

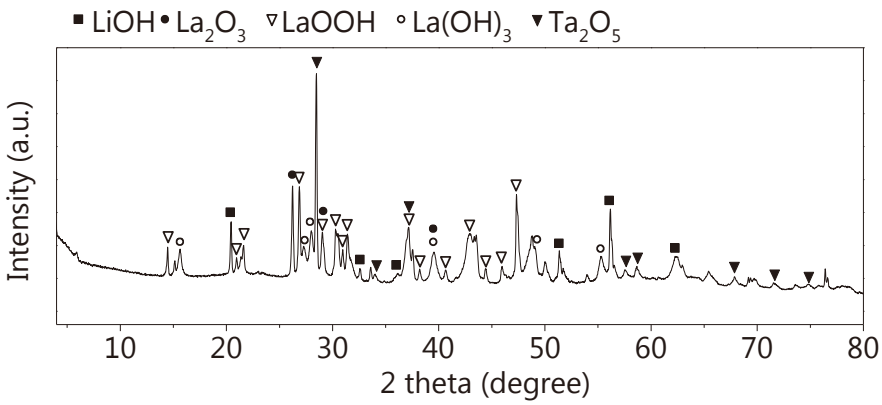

Figure 2.3 XRD patterns of samples prepared at 400 ºC before washing. Flux, LiOH; solute concentration, 5 mol%; holding time, 10 h.

At 500 ºC (Run 3-2), all diffraction peaks were attributed to $Li_5La_3Ta_2O_{12}$ without impurity phases as shown in **Figure 2.2b**. Upon increasing the holding temperature from 600 ºC to 800 ºC (Runs 2-2, 2-3, and 2-4), the peaks were gradually shifted to lower angles (**Figure 2.2c**, **2.2d**, **2.2e**), indicating the conversion of $Li_5La_3Ta_2O_{12}$ to $Li_7La_3Ta_2O_{13}$. The increase in the holding temperature up to 900 ºC (Runs 2-5) resulted in the wide peak width (**Figure 2.2f**) indicating the part decomposition of $Li_7La_3Ta_2O_{13}$

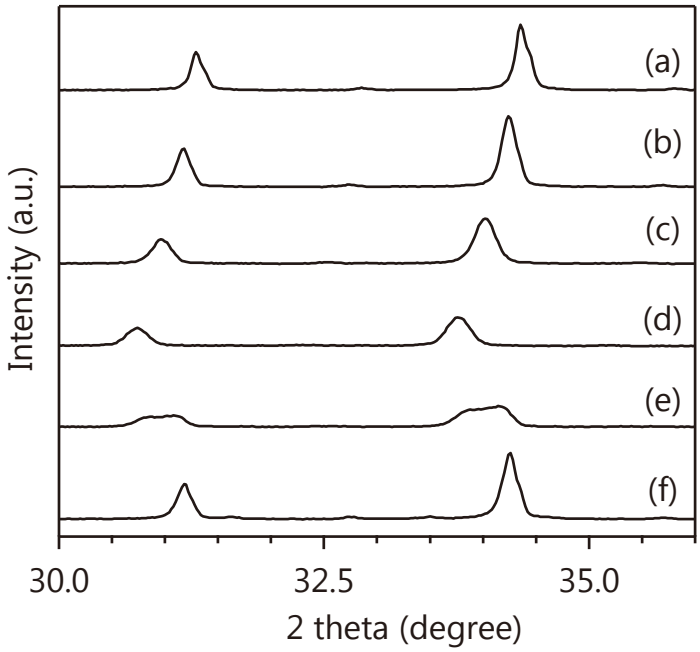

Figure 2.4 Enlarged view of the XRD patterns of sample prepared at (a) 500 ºC, (b) 600 ºC, (c) 700 ºC, (d) 800 ºC, (e) 900 ºC, and (f) 1000 ºC (flux, LiOH; solute concentration, 5 mol%; holding time, 10 h).

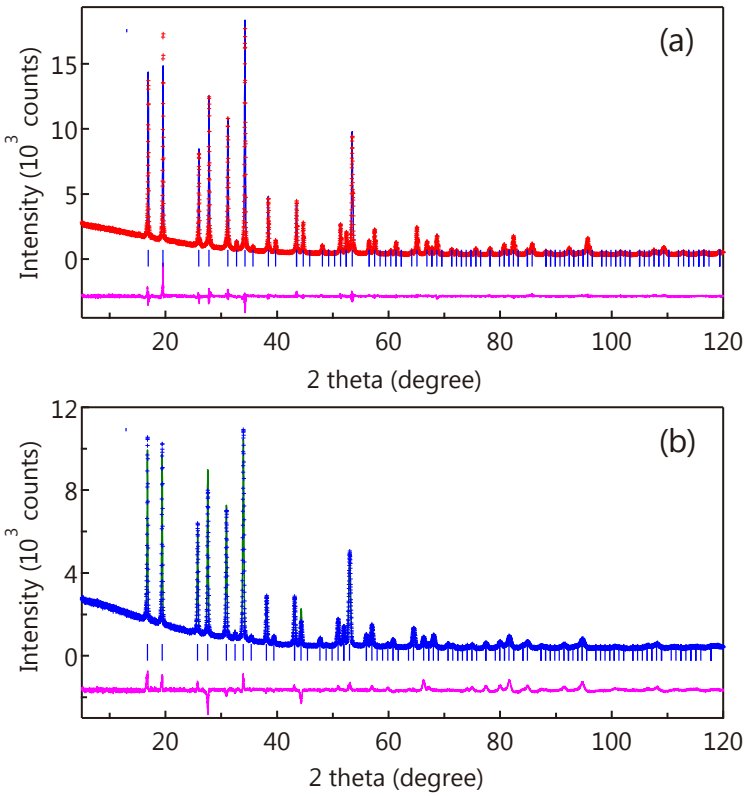

Figure 2.5 The observed (+), calculated (solid line), and their difference patterns (bottom) for the Rietveld refinement using XRD data of samples prepared at (a) 500 ºC, (b) 700 ºC. Flux, LiOH; solute concentration, 5 mol%; holding time, 10 h.

to $Li_5La_3Ta_2O_{12}$. At 1000 ºC (Runs 2-6), contrary, diffraction peaks were shifted back to higher angles (**Figure 2.2g**) and were attributed to $Li_5La_3Ta_2O_{12}$ phase. Enlarged view of XRD patterns in 2 theta range from 30 º to 36 º (**Figure 2.4**) clearly shows the peak shift.

The observed, calculated, and difference patterns for Rietveld refinement of products prepared at 500 ºC (Run 2-2) and 700 ºC (Run 2-4) are shown in **Figure 2.5**. The details of the structure refinement are listed in **Table 2.3**. The lattice parameters of $Li_5La_3Ta_2O_{12}$ and $Li_7La_3Ta_2O_{13}$ were determined to be a = 1.280601(12) nm and 1.29071(12) nm, which values are in good agreement with the literature values, 1.2804 nm and 1.286 nm, respectively.[10,19]

Table 2.3 Crystal Data and Details of the Structure Refinements for $Li_5La_3Ta_2O_{12}$ and $Li_7La_3Ta_2O_{13}$ Crystals

Empirical formula	$Li_5La_3Ta_2O_{12}$ (500 ºC, Run 2-2)	$Li_7La_3Ta_2O_{13}$ (700 ºC, Run 2-4)
system	cubic	cubic
a (nm)	1.280601(12)	1.29071(12)
R_{wp} (%)	4.99	9.00
R_e (%)	3.24	3.29
R_p (%)	3.72	5.61
GOF	1.5402	2.7329

Note that R_{wp} is weighted-profile R value with the contrubution of background, R_e is expected R value and reflects the quality of the data (*i.e.*, the counting statistics), and GOF is R_{wp}/R_e (goodness-of-fit).

Figure 2.6 shows the SEM images of the products grown at various holding temperatures range from 400 to 1000 ºC. The morphology of flux-grown crystals was markedly dependent on the temperature. The growth at 400 ºC yielded particles with

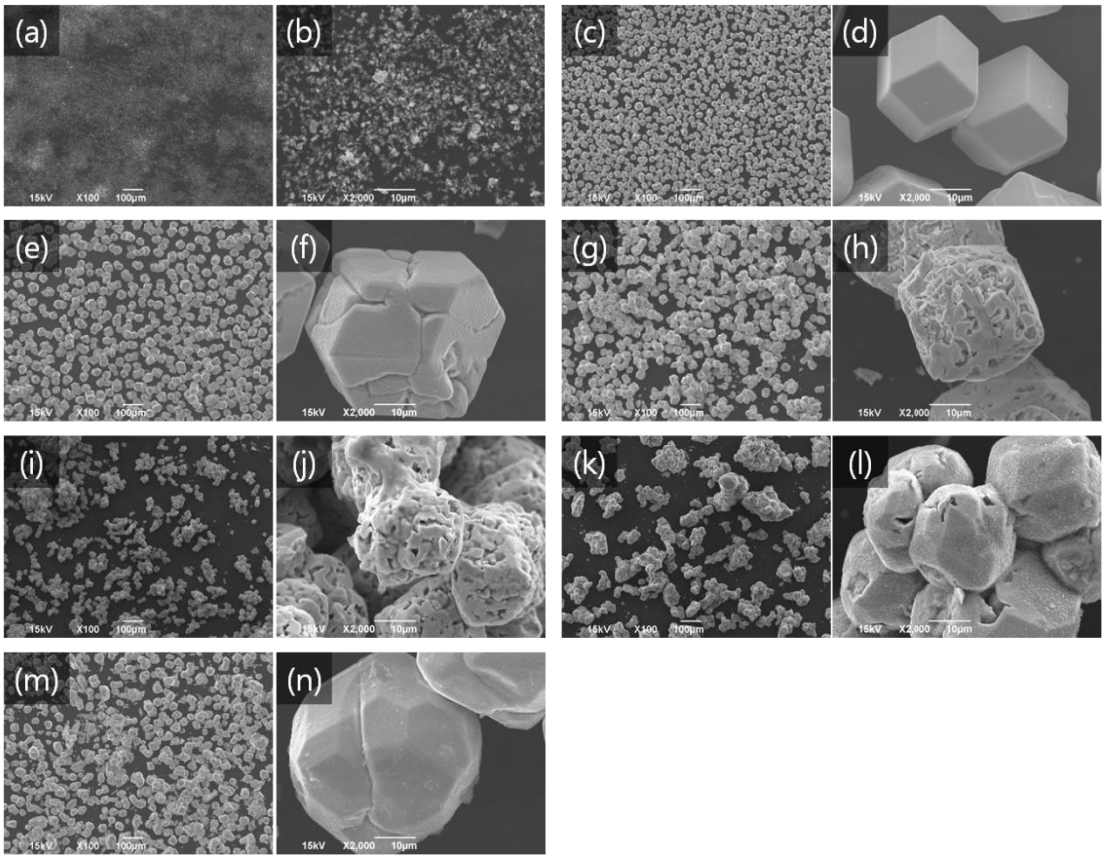

Figure 2.6 SEM images of samples prepared with different holding temperatures: (a, b) 400 ºC, (c, d) 500 ºC, (e, f) 600 ºC, (g, h) 700 ºC , (i, j) 800 ºC, (k, l) 900 ºC, and (m, n) 1000 ºC. Flux, LiOH; solute concentration, 5 mol%; holding time, 10 h.

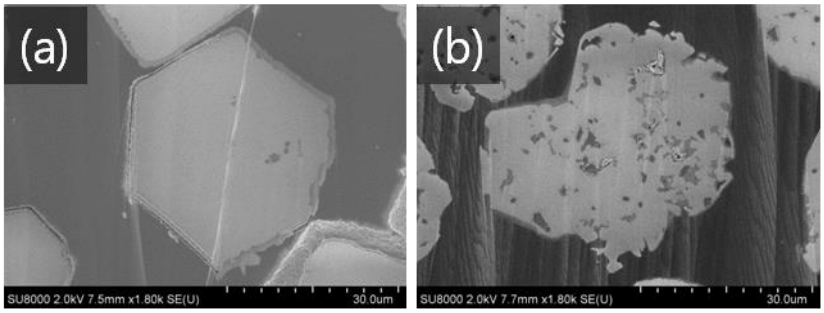

Figure 2.7 Sectional view of crystals prepared at (a) 500 ºC and (b) 700 ºC. Flux, LiOH; solute concentration, 5 mol%; holding time, 10 h.

undefined shapes, but the increase in temperature to 500 ºC produced uniform, idiomorphic single crystals with average size of ~ 36.5 μm (**Figure 2.6c**, **d**). A further increase in temperature to 600 ºC and 700 ºC led to a larger particle size and to significant porosity (**Figure 2.6e-g**). The pores formed in $Li_7La_3Ta_2O_{13}$ are clearly visible in **Figure 2.7**.

These data are indicative of the reaction of $Li_5La_3Ta_2O_{12}$ with Li_2O to form $Li_7La_3Ta_2O_{13}$. The holding time dependence at 700 ºC shown in **Figure 2.8** further supports this finding. Comparison of **Figure 2.8b** with **2.8c** supports the conclusion that the $Li_5La_3Ta_2O_{12}$ phase was already formed at 0 h, while $Li_7La_3Ta_2O_{13}$ and Li_7TaO_6

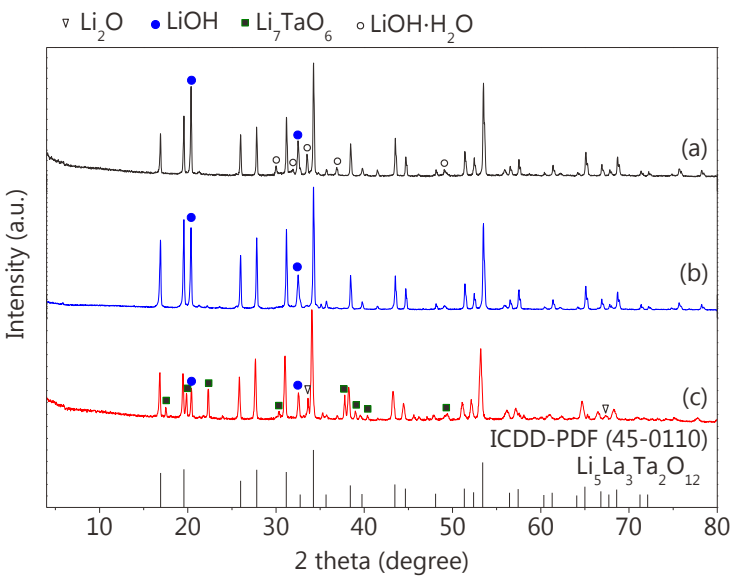

Figure 2.8 XRD patterns of samples without washing prepared at (a) 500 ºC for 10 h, 700 ºC for (b) 0 h and (c) 10 h (flux, LiOH; solute concentration, 5 mol%). The PDF pattern of $Li_5La_3Ta_2O_{12}$ extracted from the ICDD database is also shown.

crystal phases formed upon holding for 10 h at 700 ºC. This result indicates the decomposition of $Li_5La_3Ta_2O_{12}$ during the holding process. At 800 ºC, flux-grown crystals are porosity and aggregated (**Figure 2.6h**, **2.6i**), while increase in the temperature to 1000 ºC, the porosity dramatically decreased (**Figure 2.6j-n**).

The effect of the holding time at 500 ºC was then investigated, in order to understand the formation pathways of $Li_5La_3Ta_2O_{12}$. The holding temperature and solute concentration were 500 ºC and 5 mol%, respectively, and the growth conditions are summarized in **Table 2.1**. **Figure 2.9** and **2.10** show XRD patterns and SEM images of the crystals. Holding for 1 h resulted in coexisting $Li_5La_3Ta_2O_{12}$ and $LiLa_2TaO_6$ phases. Extending the holding time over 5 h provided a pure $Li_5La_3Ta_2O_{12}$ phase without byproducts, and the morphology of products changed from undefined particulate shapes to idiomorphic ones. Since the pseudo-perovskite-type $LiLa_2TaO_6$ was generated at an early stage of the reaction, this phase can be regarded as an intermediate for the $Li_5La_3Ta_2O_{12}$ formation. It is worth noting that the average crystal size increased gradually with time (37.2 μm for 5 h, 36.5 μm for 10 h, and 43.2 μm for 20 h), whereas the degree of flux evaporation was not affected and remained very low (< 5 wt.%), indicating that the evaporation of flux had no effect on crystal growth.

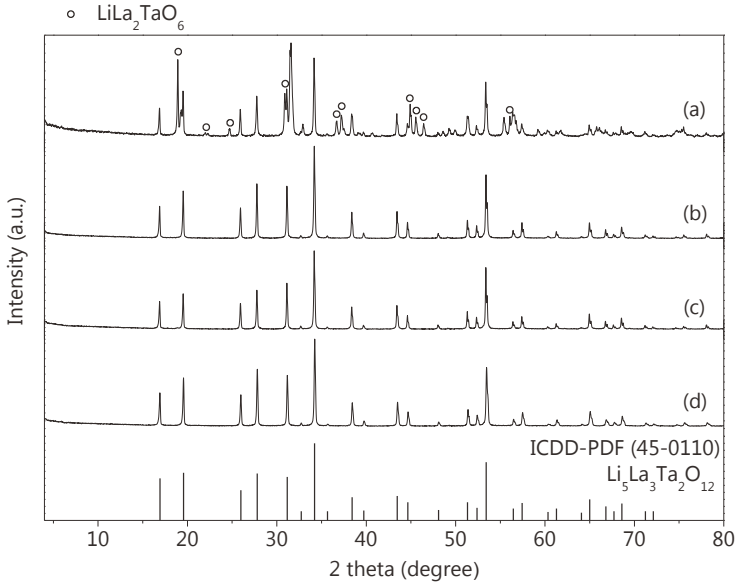

Figure 2.9 XRD patterns of flux-grown products for a holding time of (a) 1 h, (b) 5 h, (c) 10 h, and (d) 20 h. Flux, LiOH; solute concentration, 5 mol%; holding temperature, 500 ºC. The PDF pattern of $Li_5La_3Ta_2O_{12}$ extracted from the ICDD database is also shown.

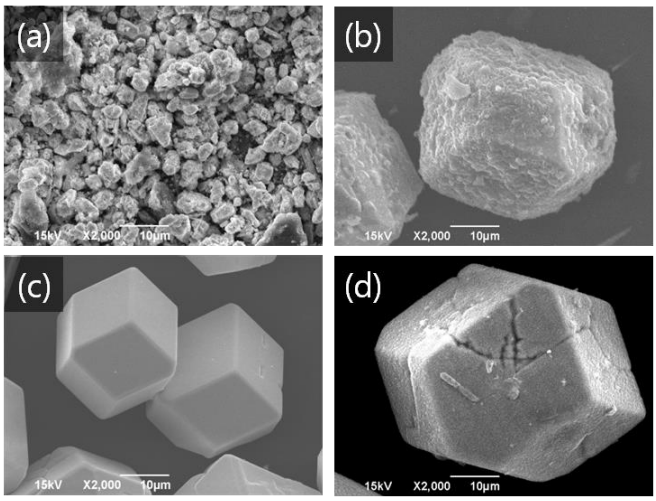

Figure 2.10 SEM images of samples prepared with different holding times: (a) 1 h, (b) 5 h, (c) 10 h, and (d) 20 h. Flux, LiOH; solute concentration, 5 mol%; holding temperature, 500 ºC.

2.3.2 Effect of cooling rate

In general, the cooling rate can affect supersaturation and promote crystal growth. **Figures 2.11** and **2.12** show the XRD patterns and SEM images of flux-grown $Li_5La_3Ta_2O_{12}$ crystals obtained with a cooling rate of 10 ºC·h^{-1} or by air-quenching. In

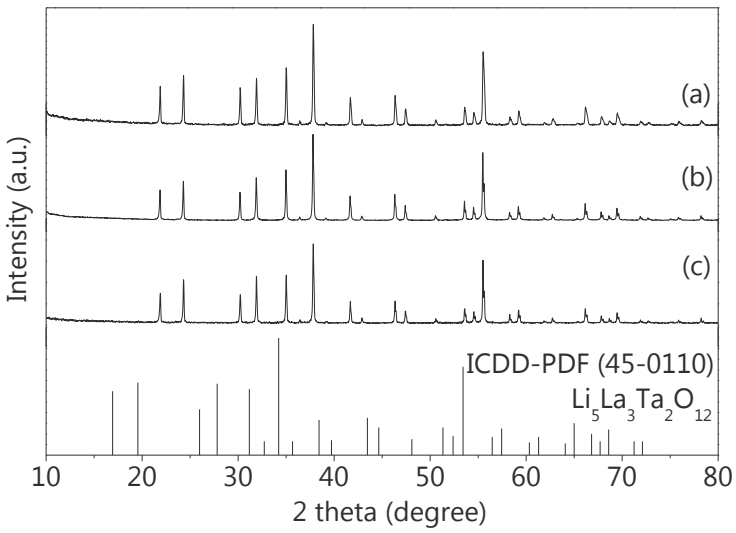

Figure 2.11 XRD patterns of crystals grown from different cooling rates: (a) 10 ºC·h^{-1}, (b) 200 ºC·h^{-1}, and (c) air quenching (> 9000 ºC·h^{-1}). Flux, LiOH; solute concentration, 5 mol%; holding temperature, 500 ºC; holding time, 10 h. The PDF pattern of $Li_5La_3Ta_2O_{12}$ extracted from the ICDD database is also shown.

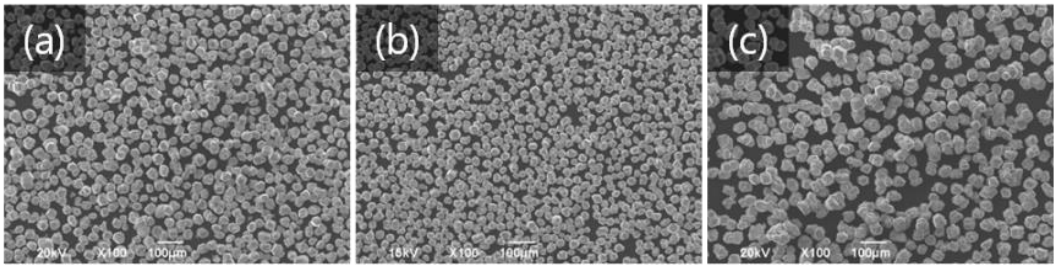

Figure 2.12 SEM images of crystals grown from different cooling rates: (a) 10 ºC·h^{-1}, (b) 200 ºC·h^{-1}, and (c) air quenching (> 9000 ºC·h^{-1}). Flux, LiOH; solute concentration, 5 mol%; holding temperature, 500 ºC; holding time, 10 h.

all cases, single-phase $Li_5La_3Ta_2O_{12}$ crystals with well-developed facets were obtained, indicating that the cooling rate has almost no influence on the phase and shape of the formed crystals. The crystal sizes were 31.6 μm, 36.5 μm, and 36.9 μm, respectively, for 10 ºC·h^{-1}, 200 ºC·h^{-1}, and air quenching, indicating that $Li_5La_3Ta_2O_{12}$ crystal growth did not occur during the cooling process. Based on the observed cooling rate as well as holding time dependence, it can be concluded that the $Li_5La_3Ta_2O_{12}$ crystal formation and growth are not only controlled by a dissolution and precipitation in which change the supersaturation caused by cooling, evaporation of flux and flow solute from a hotter to a cooler region are generally thought as driving force, but also by a chemical reaction between the solute components and the LiOH flux.

2.3.3 Effect of flux species

To determine the influence of LiOH flux, I compared the crystals discussed above with those grown from other fluxes with lower melting temperatures, such as NaOH, KOH, and $LiNO_3$, whose melting point is 250 ºC, 320 ºC, and 404 ºC, respectively. $Li_5La_3Ta_2O_{12}$ crystals were also grown by the SSR method at 500 ºC for 10 h for comparison. The growth conditions are summarized in **Table 2.2**, and the XRD patterns of the products are shown in **Figure 2.13**. The results of XRD patterns show that SSR method resulted in residual presence of the raw materials and small traces of $LiTaO_3$ and $LiLa_2TaO_6$. The use of other alkaline hydroxide fluxes (NaOH and KOH) resulted in formation of the other products, mainly due to the effect of foreign cations. The considerable difference between the crystals grown with LiOH and with the other flux systems or without flux could be due to the different degree of dissolution of solutes

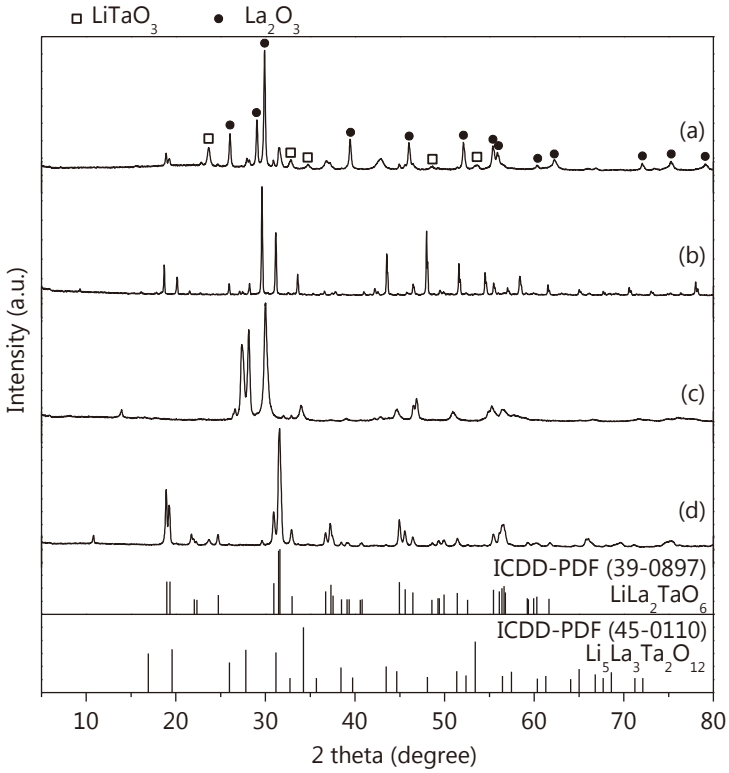

Figure 2.13 XRD patterns of samples prepared using (a) solid state reaction (SSR), (b) NaOH flux, (c) KOH flux, and (d) $LiNO_3$ flux methods. Solute concentration, 5 mol%; holding temperature, 500 ºC; holding time, 10 h. The PDF patterns of $LiLa_2TaO_6$ and $Li_5La_3Ta_2O_{12}$ extracted from the ICDD database are also shown.

(La_2O_3 and Ta_2O_5) and other kinds of alkaline components in the solvent. For instance, in general the solubility of oxides is lower in $LiNO_3$ than in LiOH.[17,21]

2.3.4 Effect of solute concentration

The effect of solute concentration on the crystal growth was then investigated, in order to understand the unique crystal shape of $Li_5La_3Ta_2O_{12}$. **Figure 2.14** shows the XRD patterns of crystals grown at solute concentrations of 1, 5, 10, 20, and 30 mol% (Runs 2-8, 2-2, 2-9, 2-10 and 2-11, in **Table 2.1**, respectively). A single $Li_5La_3Ta_2O_{12}$ phase was obtained in each run at 20 mol% or below. An increase in solute concentration to 30 mol% caused the occurrence of impurity $La(OH)_3$ and $LiLa_2TaO_6$ phases, as a result of insufficient supply of lithium source.

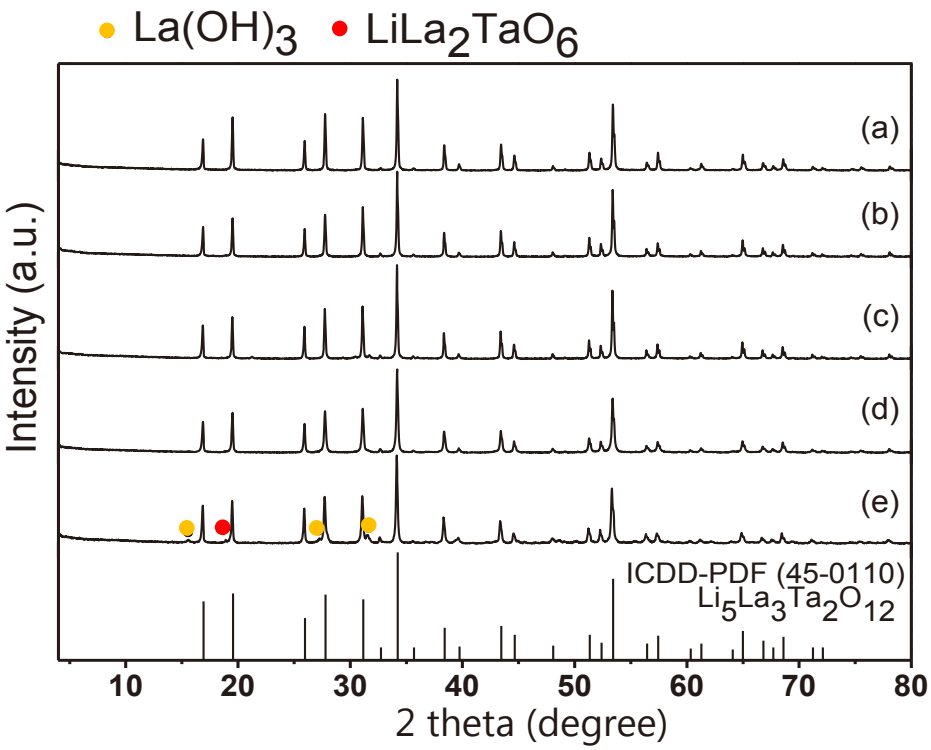

Figure 2.14 XRD patterns of samples prepared from different solute concentrations: (a) 1 mol%, (b) 5 mol%, (c) 10 mol%, (d) 20 mol%, and (e) 30 mol%. Flux, LiOH; holding temperature, 500 ºC; holding time, 10 h. The PDF pattern of $Li_5La_3Ta_2O_{12}$ extracted from the ICDD database is also shown.

The SEM images of $Li_5La_3Ta_2O_{12}$ crystals grown at various solute concentrations (**Figure 2.15**) highlight a change in particle morphology with increasing solute concentration. Relatively uniform particles of approximately the same size were obtained at 1 and 5 mol%. When the solute concentration reached 10 and 20 mol%, the crystals aggregated and their size became smaller (**Figure 2.15f, h**). Moreover, the crystal shape became undefined, a completely different behavior compared to crystals grown at low solute concentrations. This reduction in crystal size was attributed to the generation of a greater number of nuclei for higher solute concentrations.

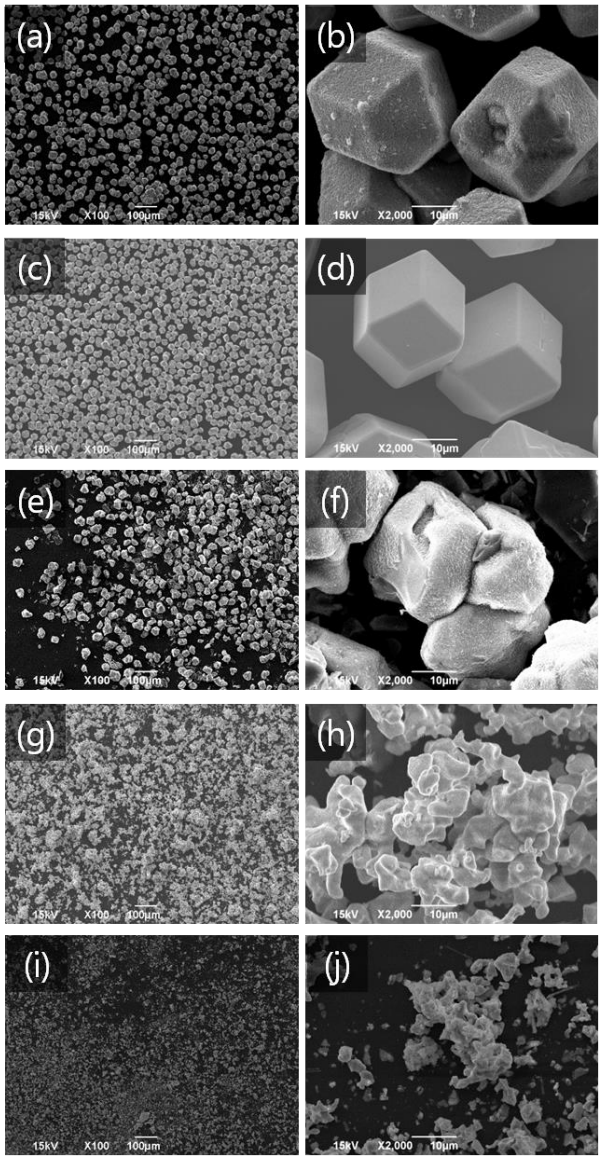

Figure 2.15 SEM images of samples prepared from different solute concentrations: (a, b) 1 mol%, (c, d) 5 mol%, (e, f) 10 mol%, (g, h) 20 mol%, and (i, j) 30 mol%. Flux, LiOH; holding temperature, 500 ºC; holding time, 10 h.

2.3.5 Growth manner for low temperature flux growth of $Li_5La_3Ta_2O_{12}$ Crystals

Based on the above results, herein I discuss the possible formation manner of idiomorphic $Li_5La_3Ta_2O_{12}$ single crystals with uniform size and particle shape from LiOH at low solute concentration. The crystal formation is schematically illustrated in **Figure 2.16**.

At the early stage of the SSR process, $LiLa_2TaO_6$ intermediates with pseudo-perovskite-type structure are formed around 500 ºC, as shown in Equation 2-1:

$$2\ La_2O_3 + Ta_2O_5 + 2\ LiOH \rightarrow 2\ LiLa_2TaO_6 + H_2O \qquad (2\text{-}1)$$

During the holding at 500 ºC, Ta_2O_5 was gradually dissolved in LiOH flux, and the resultant TaO_x species and LiOH reacted together with $LiLa_2TaO_6$ to form $Li_5La_3Ta_2O_{12}$, as illustrated in Equation 2-2:

$$6\ LiLa_2TaO_6 + Ta_2O_5 + 14\ LiOH \rightarrow 4\ Li_5La_3Ta_2O_{12} + 7\ H_2O \qquad (2\text{-}2)$$

No idiomorphic single crystals were formed in this step and the generated particles were markedly small (< 2 μm), as summarized in **Figure 2.9a** and **2.10a**. The

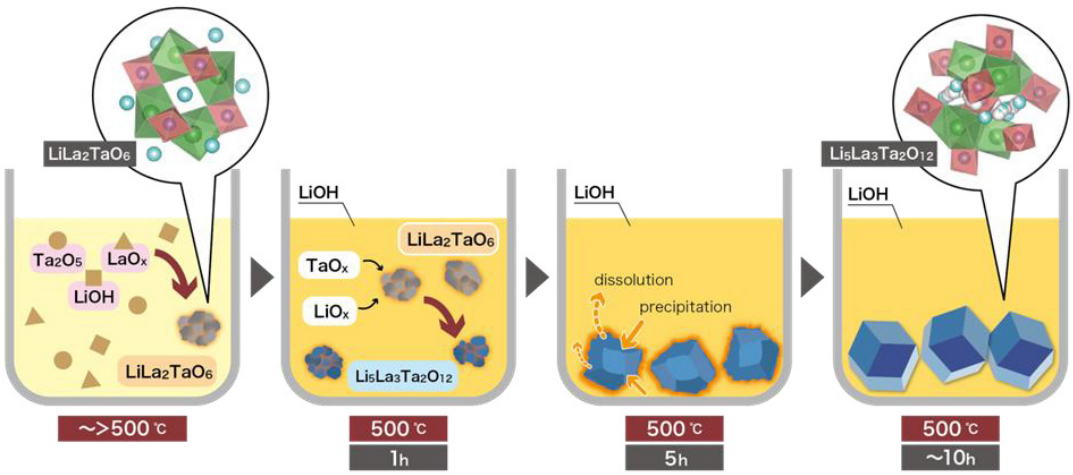

Figure 2.16 Schematic illustration of the proposed formation manner of idiomorphic $Li_5La_3Ta_2O_{12}$ single crystal. Flux, LiOH; solute concentration, 5 mol%; holding temperature, 500 ºC.

$Li_5La_3Ta_2O_{12}$ crystals were not completely dissolved in the LiOH flux during holding at 500 ºC, but part of the crystals, especially their surface, would dissolve and re-precipitate, leading to the formation of specific facets. Such repeated dissolution-precipitation processes combined with the chemical reactions of Equations 2-1 and 2-2 allow the formation of the idiomorphic $Li_5La_3Ta_2O_{12}$ crystals, which was highlighted in **Figure 2.10c**. Unfortunately, too long holding caused the rough surface of $Li_5La_3Ta_2O_{12}$ crystals (**Figure 2.10d**).

On the other hand, at 700 ºC the LiOH flux gradually decomposed to Li_2O and H_2O, according to Equation 2-3:

$$2\ LiOH \rightarrow Li_2O + H_2O \qquad (2\text{-}3)$$

The resultant Li_2O then reacted with $Li_5La_3Ta_2O_{12}$ to form lithium-rich $Li_7La_3Ta_2O_{13}$ on the bases of XRD result in **Figure 2.2d**. The reaction is shown in Equation 2-4:

$$Li_5La_3Ta_2O_{12} + Li_2O \rightarrow Li_7La_3Ta_2O_{13} \qquad (2\text{-}4)$$

The formation of pore in $Li_7La_3Ta_2O_{13}$ crystals (**Figure 2.6h**) could be due to the decomposition of $Li_5La_3Ta_2O_{12}$ and the addition reaction of Equation 2-4.

Finally, TEM analysis was used to investigate the crystal structure of the idiomorphic $Li_5La_3Ta_2O_{12}$ single crystals obtained from Run 2-2 in **Table 2.1**. **Figure 2.17a** shows the selected area electron diffraction (SAED) pattern of single crystals. Highly ordered SAED spots can be clearly observed, indicating high crystallinity. On the basis of the SAED pattern in **Figure 2.17a**, the $d_{21\text{-}1}$ spacing was determined to be 0.524 nm, which is in excellent agreement with the theoretical value of 0.523 nm.[20] **Figure 2.17b** shows a lattice image of the flux-grown $Li_5La_3Ta_2O_{12}$ single crystal, taken with the incident beam along the [120] direction. The absence of any obvious defects in these images further confirms the high crystallinity of the obtained single crystals.

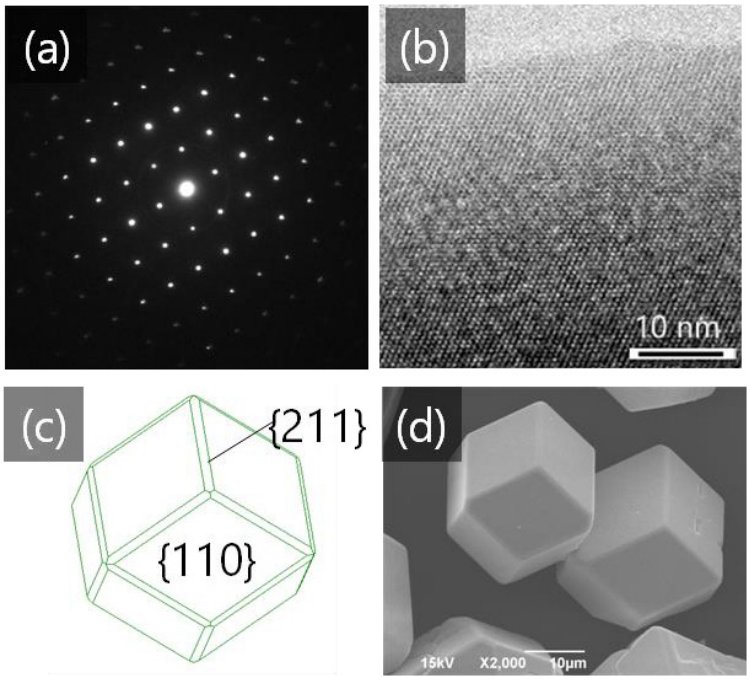

Figure 2.17 (a) SAED pattern, (b) lattice image, (c) schematic illustration, and (d) SEM image of $Li_5La_3Ta_2O_{12}$ crystals grown under optimum conditions. Flux, LiOH; holding temperature, 500 ºC, solute concentration, 5 mol%; holding time, 10 h.

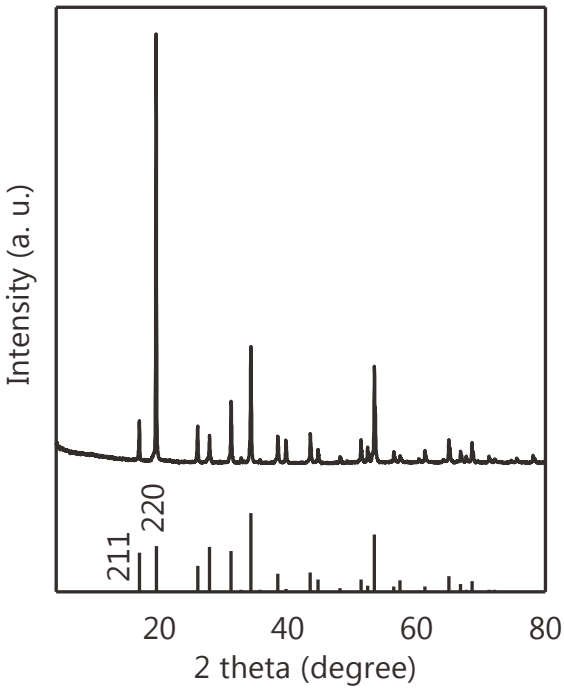

Figure 2.18 (Top) XRD pattern of $Li_5La_3Ta_2O_{12}$ single crystals without grinding and (bottom) Powder Diffraction File pattern of $Li_5La_3Ta_2O_{12}$ (# 45-0110) taken from the International Centre for Diffraction Data database. Flux, LiOH; solute concentration, 5 mol%; holding temperature, 500 ºC; holding time, 10 h.

The lattice parameter of the $Li_5La_3Ta_2O_{12}$ single crystals was determined to be a =

12.80601(12) Å from the XRD pattern in **Figure 2.2b**, which is consistent with the literature value of 12.804 Å.[10] **Figure 2.18** shows the XRD pattern of $Li_5La_3Ta_2O_{12}$ single crystals without previous grinding. The intensity ratio of {110} to {211} is 10.5, higher than that calculated from the corresponding International Center for Diffraction Data (ICDD) Powder Diffraction File (PDF) data (pattern # 45-0110, Int. {110} / Int. {211} = 1.2). This finding indicates that {110} faces are predominant on $Li_5La_3Ta_2O_{12}$ crystals. **Figure 2.17c** shows a schematic illustration of a $Li_5La_3Ta_2O_{12}$ single crystal, mainly exposing {110} and {211} faces, drawn using crystallographic data from the literature.[22] Notably, the illustration is in excellent agreement with the observed shape of the flux-grown $Li_5La_3Ta_2O_{12}$ single crystals (**Figure 2.17d**), leading us to conclude that $Li_5La_3Ta_2O_{12}$ single crystals are dominated by {110} and smaller-area {211} faces.

2.4 Conclusion

In this chapter I described the low-temperature growth of idiomorphic $Li_5La_3Ta_2O_{12}$ single crystals from LiOH flux and investigated their growth manner under different crystal growth conditions. $Li_5La_3Ta_2O_{12}$ crystals were grown at 500 ºC, and transformed to $Li_7La_3Ta_2O_{13}$ at 700 ºC as a result of the reaction of $Li_5La_3Ta_2O_{12}$ with Li_2O. The holding time dependence experiments indicated that the pseudo-perovskite-type $LiLa_2TaO_6$ is a key intermediate for the formation of $Li_5La_3Ta_2O_{12}$. On the other hand, the evaporation ratio and cooling rate did not affect the phase and morphology of crystals. Low solute concentrations (1 or 5 mol%) improved the shape and dispersity of the crystals. These results indicate that the idiomorphic $Li_5La_3Ta_2O_{12}$ crystals are formed from LiOH flux through the combination of the chemical reaction of Equation 3-2 with repeated dissolution-precipitation processes, as summarized in **Figure 2.16**. Because this represents a different crystal formation process compared to conventional flux growth, the present research has the potential to open a new avenue for the fabrication of other garnet-type materials.

References

(1) Cussen, E. J. The structure of lithium garnets: cation disorder and clustering in a new family of fast Li^+ conductors. *Chem. Commun.* **2006**, *4*, 412-413.

(2) Murugan, R.; Thangadurai, V.; Weppner, W. Fast Lithium Ion Conduction in Garnet-Type $Li_7La_3Zr_2O_{12}$. *Angew. Chem. Int. Ed.* **2007**, *46*, 7778–7781.

(3) Cussen, E. J.; Yip, T. W. S. A neutron diffraction study of the d^0 and d^{10} lithium garnets $Li_3Nd_3W_2O_{12}$ and $Li_5La_3Sb_2O_{12}$. *J. Solid State Chem.* **2007**, *180*, 1832–1839.

(4) Galven, C.; Fourquet, J. Instability of the Lithium Garnet $Li_7La_3Sn_2O_{12}$: Li^+/H^+ Exchange and Structural Study. *Chem. Mater.* **2011**, *23*, 1892–1900.

(5) Xu, M.; Park, M. S.; Lee, J. M.; Kim, T. Y.; Park, Y. S.; Ma, E. Mechanisms of Li^+ transport in garnet-type cubic $Li_{3+x}La_3M_2O_{12}$ (M = Te, Nb, Zr). *Phys. Rev. B* **2012**, *85*, 052301.

(6) Roof, I. P.; Smith, M. D.; Cussen, E. J.; zur Loye, H.-C. Crystal growth of a series of lithium garnets $Ln_3Li_5Ta_2O_{12}$ (Ln=La, Pr, Nd): Structural properties, Alexandrite effect and unusual ionic conductivity. *J. Solid State Chem.* **2009**, *182*, 295–300.

(7) Ohta, S.; Kobayashi, T.; Asaoka, T. High lithium ionic conductivity in the garnet-type oxide $Li_{7-X}La_3(Zr_{2-X}, Nb_X)O_{12}$ (X = 0–2). *J. Power Sources* **2011**, *196*, 3342–3345.

(8) Allen, J. L.; Wolfenstine, J.; Rangasamy, E.; Sakamoto, J. Effect of substitution (Ta, Al, Ga) on the conductivity of $Li_7La_3Zr_2O_{12}$. *J. Power Sources* **2012**, *206*, 315–319.

(9) Miara, L. J.; Ong, S. P.; Mo, Y.; Richards, W. D.; Park, Y.; Lee, J.; Lee, H. S.; Ceder, G. Effect of Rb and Ta Doping on the Ionic Conductivity and Stability of the Garnet $Li_{7+2x-y}(La_{3-x}Rb_x)(Zr_{2-y}Ta_y)O_{12}$ ($0 \leqslant x \leqslant 0.375$, $0 \leqslant y \leqslant 1$) Superionic Conductor: A First Principles Investigation. *Chem. Mater.* **2013**, *25*, 3048–3055.

(10) Hyooma, H.; Hayashi, K. Crystal structures of $La_3Li_5M_2O_{12}$ (M = Nb, Ta). *Mater. Res. Bull.* **1988**, *23*, 1399–1407.

(11) Il'ina, E. A.; Andreev, O. L.; Antonov, B. D.; Batalov, N. N. Morphology and transport properties of the solid electrolyte $Li_7La_3Zr_2O_{12}$ prepared by the solid-state and citrate–nitrate methods. *J. Power Sources* **2012**, *201*, 169–173.

(12) Bugaris, D.; zur Loye, H. -C. Materials Discovery by Flux Crystal Growth: Quaternary and Higher Order Oxides. *Angew. Chem. Int. Ed.* **2012**, *51*, 3780–3811.

(13) Oishi, S.; Teshima, K.; Kondo, H. Flux Growth of Hexagonal Bipyramidal Ruby Crystals. *J. Am. Chem. Soc.* **2004**, *126*, 4768–4769.

(14) Awaka, J.; Kijima, N.; Hayakawa, H.; Akimoto, J. Synthesis and structure analysis of tetragonal $Li_7La_3Zr_2O_{12}$ with the garnet-related type structure. *J. Solid State Chem.*, **2009**, *182*, 2046–2052.

(15) Tietz, F.; Wegener, T.; Gerhards, M. T.; Giarola, M.; Mariotto, G. Synthesis and Raman micro-spectroscopy investigation of $Li_7La_3Zr_2O_{12}$. *Solid State Ionics*, **2013**, *230*, 77–82.

(16) Kimijima, T.; Zettsu, N.; Onodera, H.; Yubuta, K.; Oishi, S.; Teshima, K. Low-temperature growth of idiomorphic cubic- phase $Li_7La_3Zr_2O_{12}$ crystals using LiOH flux. *CrystEngComm*, **2015**, *17*, 3487–3492.

(17) Mugavero, S. J.; Gemmill, W. R.; Roof, I. P.; zur Loye, H.-C. Materials discovery by crystal growth: Lanthanide metal containing oxides of the platinum group metals (Ru, Os, Ir, Rh, Pd, Pt) from molten alkali metal hydroxides. *J. Solid State Chem.* **2009**, *182*, 1950–1963.

(18) Mizuno, Y.; Wagata, H.; Onodera, H. Environmentally Friendly Flux Growth of High-Quality, Idiomorphic $Li_5La_3Nb_2O_{12}$ Crystals. *Cryst. Growth & Des.* **2013**, *13*, 479–484.

(19) Hayashi, K.; Noguchi, H.; Fugiwara, S. NEW PHASES IN La_2O_3-Li_2O-Ta_2O_5 SYSTEM. *Mat. Res. Bull.* **1986**, *21*, 289–293.

(20) Mazza, D. REMARKS ON A TERNARY PHASE IN THE La_2O_3-Me_2O_5-Li_2O SYSTEM (Me = Nb, Ta). *Mater. Lett.* **1988**, *7*, 205–207.

(21) Flood, H.; Förland, T. The Acidic and Basic Properties of Oxides. *Acta Chem. Scand.* **1947**, *1*, 592–604.

(22) Thangadurai, V.; Adams, S.; Weppner, W. Crystal Structure Revision and Identification of Li^+-Ion Migration Pathways in the Garnet-like $Li_5La_3M_2O_{12}$ (M = Nb, Ta) Oxides. *Chem. Mater.* **2004**, *12*, 2998–3006.

Chapter 3
Growth of platy β-Li_2TiO_3 crystals with exposed {001} facets from oxysalt fluxes

Chapter 3 Growth of platy β-Li_2TiO_3 crystals with exposed {001} facets from oxysalt fluxes

3.1 Introduction

Lithium metatitanate (β-Li_2TiO_3) has many practical applications such as in tritium breeders,[1,2] cathode materials for lithium ion batteries,[3] and a precursor for lithium ion adsorbents[4,5] due to its superior tritium diffusion and lithium ion intercalation properties. With respect to particle size, micrometer-sized β-Li_2TiO_3 crystals are preferred for tritium breeder and adsorbent applications, while the submicrometer- or nanometer-sized crystals are preferred in battery electrodes for quick charge and discharge processes. Li_2TiO_3 exists in three polymorphs named: α-, β-, and γ-Li_2TiO_3.[6] The α-phase is metastable and can be converted irreversibly to β-Li_2TiO_3 when heated to above 300 °C.[7] β-Li_2TiO_3 exhibits the monoclinic Li_2SnO_3-type structure with the space group of C2/c (Z = 8), as summarized in **Figure 3.1**.[8] The β-Li_2TiO_3 crystal consists of alternating pure Li layers and $LiTi_2$ layers as can be seen in the left panel in **Figure 3.1**. According to the refined structural data,[8,9] there exist three crystallographically inequivalent Li positions (Li(1), Li(2), and Li(3)) on 8f, 4d, and 4e Wyckoff sites, respectively, and two inequivalent Ti positions (Ti(1) and Ti(2)) on 4e sites (**Figure 3.1**). The reported crystal parameters of β-Li_2TiO_3 at 295 K are a = 5.0623(5) nm, b = 8.7876(9) nm, c = 9.7533(15) nm, and β = 100.212(11)°.[9]

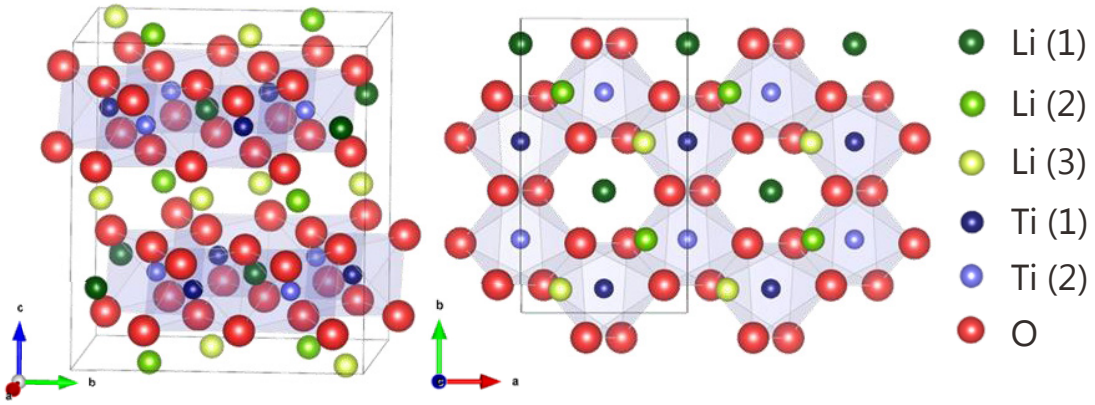

Figure 3.1 Crystal structure of β-Li_2TiO_3 visualized using the VESTA program.[10] Three crystallographically inequivalent Li positions on 8f, 4d, and 4e Wyckoff sites are represented by Li(1) (dark green ball), Li(2) (light green ball), and Li(3) (light yellow ball), respectively, and two inequivalent Ti positions on 4e sites are represented by Ti(1) (dark blue ball) and Ti(2) (light blue ball); and oxygen sits are depicted using red balls.

The Li^+ conductivity of β-Li_2TiO_3 has been studied using dc conductivity measurement,[11] solid state NMR spectroscopy,[12] and density functional theory (DFT) calculation.[13] Islam and Bredow reported that Li^+ migrates along the *ab* plane as well as in the direction perpendicular to the $LiTi_2$ layers.[13] Their calculated activation energies (~0.40 eV) for hopping perpendicular to the $LiTi_2$ layers (*i.e.,* along the *c* axis) are lower than that of direct Li^+ exchange between Li(1) and Li(2) within the *ab* plane (~0.45 eV), indicating the anisotropic nature of Li^+ conduction in the *β*-Li_2TiO_3 crystal. In contrast, Vijayakumar and coworkers reported lower activation energies (0.20–0.30 eV) for hopping within the *ab* plane.[12] The inconsistency between these two reports might be attributed to impurities and defects in the host β-Li_2TiO_3 crystals. Therefore, the preparation of high quality faceted β-Li_2TiO_3 crystals with controlled morphology could allow more accurate determination of their Li^+ diffusion property.

β-Li_2TiO_3 crystals have been prepared by solid-state reaction,[5] hydrothermal process,[14] sol-gel process,[15] and two-step flux method.[9] However, most of the resulting β-Li_2TiO_3 crystals possessed no faceted surface features and were aggregates of crystallites with a wide size distribution. The flux crystal growth is a liquid-phase

method that uses molten metals or metal salts as the solvent to enable efficient crystal growth below the melting points of the solutes.[16,17] High-quality crystals with faceted surface features have been prepared by flux method under suitable conditions. For instance, hexagonal nanoplate-like $LiCoO_2$ crystals,[18] octahedral-shaped $Li(Ni_{1/3}Co_{1/3}Mn_{1/3})O_2$ crystals,[19] and cuboidal $LiMnO_2$ crystals,[20] all with good electrochemical/adsorptive properties were grown from NaCl, Na_2SO_4, and LiCl-KCl fluxes, respectively. The particle shape and crystal phase of iron oxide could also be controlled by adding the appropriate alkali metal carbonate as a flux, thanks to the surface stabilization effect.[21] However, factors that control crystal shapes and faces and the corresponding detailed mechanism during flux crystal growth remain poorly understood. For growing of nanocrystals such as nanorods and nanobelts, it is well accepted that continuous, anisotropic nanocrystal growth is attributed to preferential adsorption of shape directing agents (such as polar molecules and amphiphilic ions) on the exposed surface of crystals.[22] Therefore, in the case of β-Li_2TiO_3, certain cations and/or anions in the flux could also act as shape directing agents and direct the growth of crystals by adsorption on the crystal surface.

In this study, I comprehensively studied the growth of idiomorphic β-Li_2TiO_3 crystals with faceted surface features from various alkali metal salt-based fluxes. I explored several flux growth conditions, namely the flux species, holding temperature, solute concentration, and holding time to obtain large, faceted β-Li_2TiO_3 crystals. The crystal growth process was then studied in the optimal flux of Na_2SO_4. The formation process of platy, {001}-faceted β-Li_2TiO_3 single crystals, is discussed based on the characterization results.

3.2 Experimental section

3.2.1 Flux growth of β-Li_2TiO_3 crystals

All reagents were purchased from Wako Pure Chemical Industries, Ltd. and used without further purification. $LiOH{\cdot}H_2O$ (99.0%) and TiO_2 (anatase, 98.0%) were

employed as solutes. LiCl (99.0%), NaCl (99.5%), KCl (99.5%), $Li_2SO_4 \cdot H_2O$ (99.0%), Na_2SO_4 (99.0%), or K_2SO_4 (99.0%) was employed as the flux. Typically, a stoichiometric mixture of $LiOH \cdot H_2O$ and TiO_2 was mixed with the flux, with the solute concentration (defined as the molar ratio between β-Li_2TiO_3 and the flux) in the range of 1–80 mol%. The flux growth conditions are summarized in **Table 3.1** and **Table 3.2**. A mixture of the solutes and flux (~10 g) was placed into an alumina crucible. The crucible was covered with a lid and heated in an electric furnace to the set temperature at a rate of 300 $°C \cdot h^{-1}$, and then was kept for a certain holding time. Afterwards, the crucible was cooled to 500 °C at a rate of 300 or 5 $°C \cdot h^{-1}$, and then naturally cooled to room temperature in air. The product was washed with distilled water at room temperature, and then dried in air at 100 °C. For comparison, β-Li_2TiO_3 crystals were also prepared via a solid-state reaction (Run 3-12 in **Table 3.1**).

Table 3.1 Growth Conditions for β-Li_2TiO_3 Crystals from Alkali Metal Salt-Based Fluxes.

Run	Holding temp. / ºC	Solute		Flux						Solute concentration (mol%)	Holding time / h	Cooling rate / ºC h^{-1}
		LiOH[a] / g	TiO_2 / g	Li_2SO_4[b] / g	Na_2SO_4 / g	K_2SO_4 / g	LiCl / g	NaCl / g	KCl / g			
3-1	1000	1.242	1.182	7.576	0	0	0	0	0	20	10	300
3-2	1000	1.146	1.091	0	7.763	0	0	0	0	20	10	300
3-3	1000	0.975	0.928	0	0	8.097	0	0	0	20	10	300
3-4	1000	2.518	2.396	0	0	0	5.087	0	0	20	10	300
4-5	1000	2.111	2.009	0	0	0	0	5.880	0	20	10	300
3-6	1000	1.817	1.730	0	0	0	0	0	6.453	20	10	300
3-7	900	1.146	1.091	0	7.763	0	0	0	0	20	10	300
3-8	1000	0.059	0.056	0	9.885	0	0	0	0	1	10	300
3-9	1000	0.582	0.554	0	8.864	0	0	0	0	10	10	300
3-10	1000	2.744	2.611	0	4.645	0	0	0	0	50	10	300
3-11	1000	4.211	4.007	0	1.782	0	0	0	0	80	10	300
3-12	1000	5.124	4.876	0	0	0	0	0	0	100	10	300
3-13	1000	1.146	1.091	0	7.763	0	0	0	0	20	0	300
3-14	1000	1.146	1.091	0	7.763	0	0	0	0	20	5	300
3-15	1000	1.146	1.091	0	7.763	0	0	0	0	20	30	300
3-16	1000	1.146	1.091	0	7.763	0	0	0	0	20	10	5

[a] LiOH H_2O, [b] Li_2SO_4 H_2O

Table 3.2 Growth Conditions for β-Li_2TiO_3 Crystals from Alkali Metal-Based Molybdate Fluxes

Run	Holding temp. / ºC	Solute		Flux			Solute concentration (mol%)	Holding time / h	Cooling rate / ºC h^{-1}
		LiOH[a] / g	TiO_2 / g	Li_2MoO_4 / g	Na_2MoO_4[b] / g	K_2MoO_4 / g			
4-17	1000	0.977	0.930	8.0934	0	0	20	10	300
4-18	1000	0.742	0.706	0	8.552	0	20	10	300
4-19	1000	0.752	0.715	0	0	8.533	20	10	300

[a] LiOH H_2O, [b] Na_2MoO_4 $2H_2O$

3.2.2 Characterization

X-ray diffraction (XRD) patterns were recorded on a Miniflex II powder diffractometer (Rigaku) with monochromated Cu K_α radiation (λ = 0.15418 nm, 30 kV, 20 mA). The XRD data for the Rietveld refinement were collected in the 2θ range from 5° to 150° with a step of 0.02° on a powder diffractometer (RIGAKU, SmartLab) using Cu K_α radiation (λ = 0.15418 nm, 40 kV, 40 mA). The whole pattern analysis of β-Li_2TiO_3 crystals grown at 1000 °C under optimal conditions (flux, Na_2SO_4; solute conc., 20 mol%; holding time, 10 h; cooling rate, 300 °C·h^{-1}) was carried out using the PDXL software (RIGAKU). Scanning electron microscopy (SEM, JEOL, JCM-5700) images were collected at an acceleration voltage of 15 kV. The average size of the β-Li_2TiO_3 crystals was analyzed by a laser diffraction particle size analyzer (SALD-7100, SHIMADZU). Transmission electron microscopy (TEM, TOPCON, EM-002B) data were obtained at an acceleration voltage of 200 kV. For the TEM observation and analysis of the dominate facet(s) of β-Li_2TiO_3 crystals, a typical platy crystal was selected and milled to 5 μm × 5 μm × 100 nm in size by using a focused ion beam apparatus (FIB, JIB-4000, JEOL). The TEM image and selected area electron diffraction (SAED) pattern were taken with the incident beam parallel to the exposed dominant facet. For chemical analysis, the crystals were dissolved in 2 mM HF solution, and the supernatant was analyzed by inductively coupled plasma-optical emission spectrometry (ICP-OES, SII, SPS5510).

3.3 Results and discussion

3.3.1 Effects of different fluxes on the growth of β-Li_2TiO_3 crystals

In general, the flux growth of crystals depends on several factors. The cation and anion

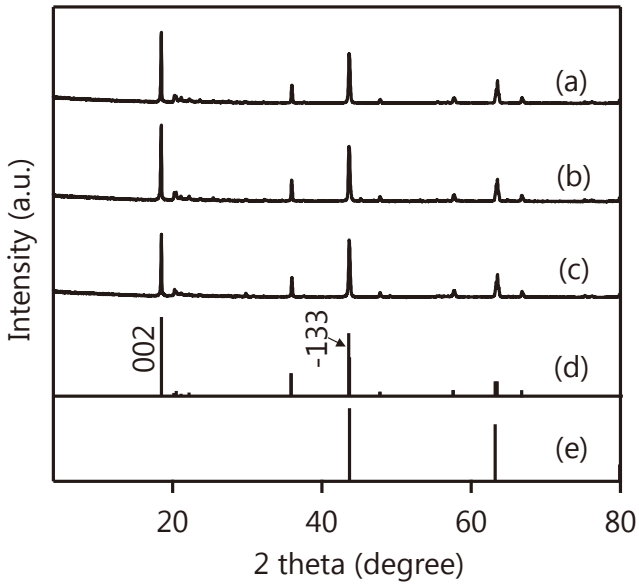

Figure 3.2 XRD patterns of β-Li_2TiO_3 crystals grown from (a) Li_2SO_4, (b) Na_2SO_4, and (c) K_2SO_4 fluxes. Solute concentration, 20 mol%; holding temperature, 1000 ºC; holding time, 10 h; cooling rate, 300 ºC h^{-1}. The Powder Diffraction File (PDF) patterns of (d) β-Li_2TiO_3 (# 33-0831) and (e) α-Li_2TiO_3 (# 03-1024) are taken from the ICDD database.

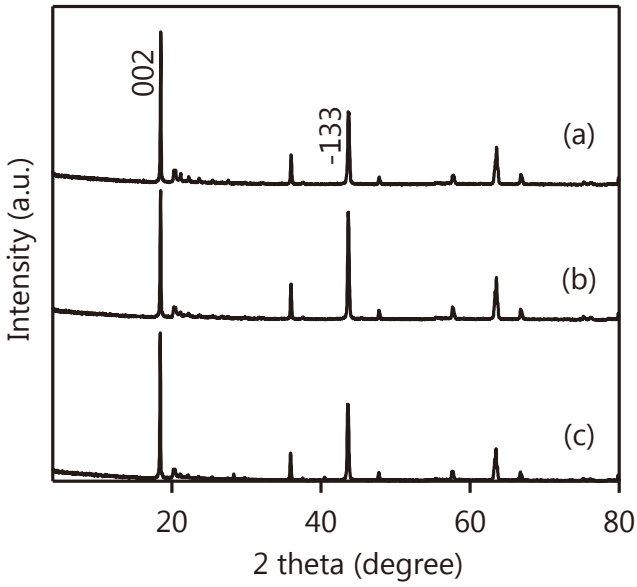

Figure 3.3 XRD patterns of β-Li_2TiO_3 crystals grown from (a) LiCl, (b) NaCl, and (c) KCl fluxes. Solute concentration, 20 mol%; holding temperature, 1000 ºC; holding time, 10 h; cooling rate, 300 ºC h^{-1}.

in the flux, melting point of the flux, and growth conditions all can influence the ability of the flux to dissolve the solutes.[16,17] I first examined the effect of different alkali metal salt-based fluxes in order to find the best one for faceted crystal growth. LiCl, NaCl, KCl, $Li_2SO_4 \cdot H_2O$, Na_2SO_4, and K_2SO_4 were employed as the flux with a holding

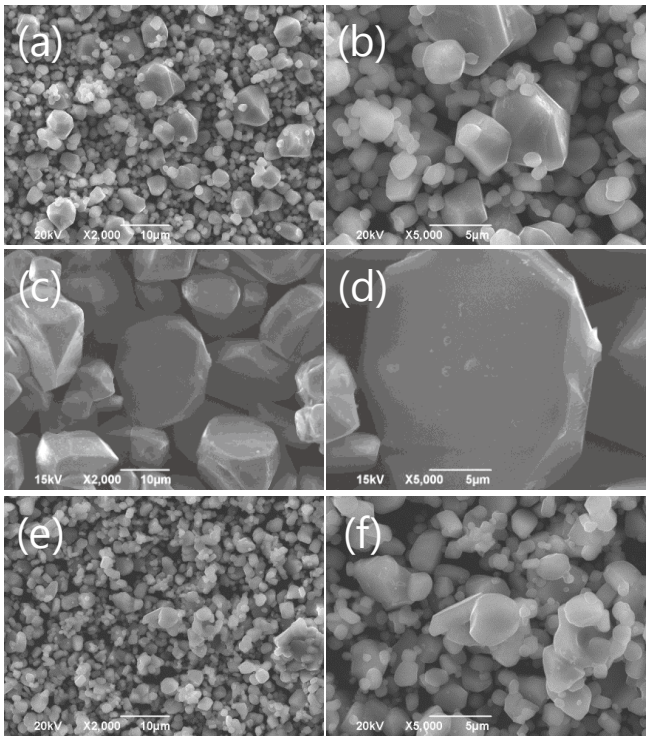

Figure 3.4 SEM images of β-Li_2TiO_3 crystals grown from (a, b) Li_2SO_4, (c, d) Na_2SO_4, and (e, f) K_2SO_4 flux. Solute concentration, 20 mol%; holding temperature, 1000 ºC; holding time, 10 h; cooling rate, 300 ºC h^{-1}.

temperature of 1000 °C, a solute concentration of 20 mol%, and a holding time of 10 h.

Figure 3.2 and **Figure 3.3** show the XRD patterns of the flux-grown crystals. All the diffraction peaks were assigned to the β-Li_2TiO_3 phase, indicating single-phase β-Li_2TiO_3 crystals for each flux. **Figure 3.4** and **Figure 3.5** show the SEM images of the crystals grown from each flux. The crystals grown from LiCl, NaCl, KCl, and $Li_2SO_4 \cdot H_2O$ fluxes were monodispersed β-Li_2TiO_3 crystals with undeveloped and inhomogeneous shapes. In contrast, the use of Na_2SO_4 or K_2SO_4 flux led to the formation of plate-like β-Li_2TiO_3 crystals with faceted surface features (**Figures 3.4d** and **3.4f**). This sharp difference in the crystal morphology could be attributed to the solubilities of the solutes in different fluxes and capping effect of foreign cations, which will be explained in the final part of the RESULTS AND DISCUSSION in this chapter.

Figure 3.6 shows the average particle size of β-Li_2TiO_3 crystals grown in the different fluxes. Platy β-Li_2TiO_3 crystals with lateral size of ~15.0 μm and an aspect ratio of 3.5 were grown from the Na_2SO_4 flux, and they are typically 2–5 times larger

than those grown in other fluxes (3.0–6.0 μm). It follows that Na_2SO_4 flux is the best medium under the present growth conditions for large, faceted β-Li_2TiO_3 crystals.

A common cation and anion between the solutes and the flux often have a positive impact on the flux crystal growth, because the polarizabilities of the solvent and solute

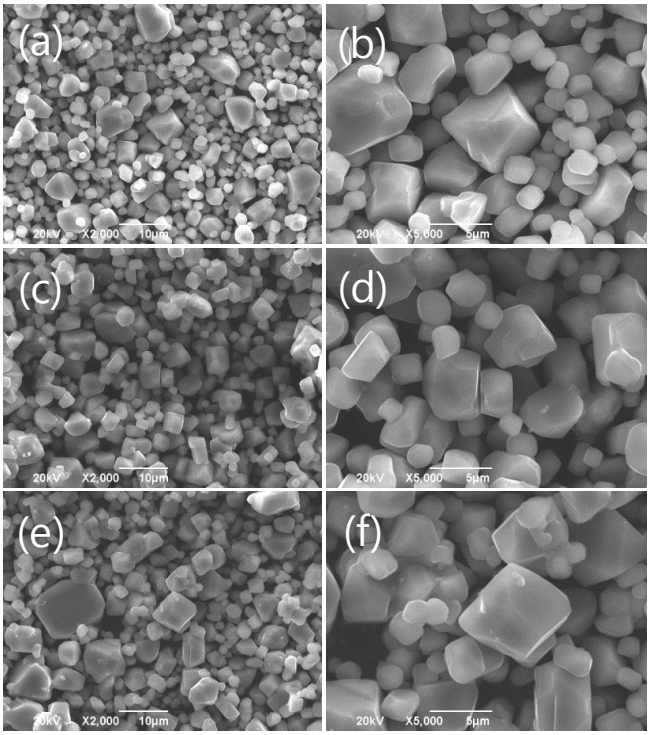

Figure 3.5 SEM images of β-Li_2TiO_3 crystals grown from (a, b) LiCl, (c, d) NaCl, and (e, f) KCl flux. Solute concentration, 20 mol%; holding time, 1000 ºC; holding time, 10 h.

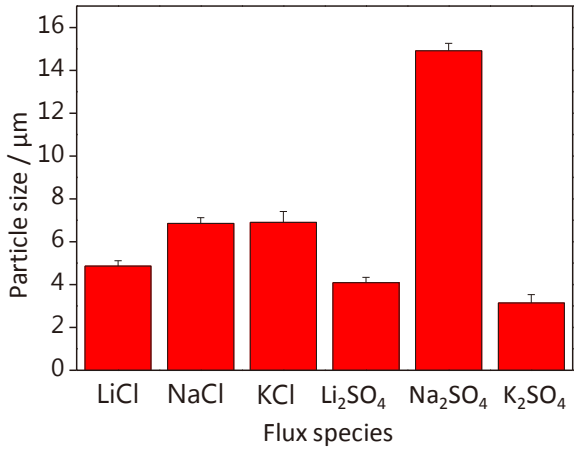

Figure 3.6 Average particle size of grown β-Li_2TiO_3 crystals using different flux species. Solute concentration, 20 mol%; holding temperature, 1000 ºC; holding time, 10 h; cooling rate, 300 ºC h^{-1}. The average crystal size was analyzed by a laser diffraction particle size analyzer.

are well matched in such cases. Namely, the appropriate flux can promote the dissolution of solutes by (i) stabilizing the metal complexes that act as intermediate for the product crystals in solution, (ii) increasing the metastable window in which supersaturation can exist, and (iii) affecting the crystal nucleation and thereby the crystal morphology.[16] For the growth of oxide crystals, the solvation of O^{2-} ions is crucial for making them available for constructing the framework of single crystals.[23] Hayashi and coworkers reported that the solubility of the precursor oxides in the sulfate based flux is much higher than that in the halide-based flux, resulting in changes in the particle shape.[24] On the other hand, Cortese and coworkers reported that the flux containing larger alkali metal cations is superior for solvating O^{2-}.[25] Taking into accounts the two findings from literatures, the observed efficient crystal growth in Na_2SO_4 flux could be attributed to the capability of Na_2SO_4 for both dissolving the precursor and product oxides and solvating O^{2-} ions. It should be added to note that the melting point of K_2SO_4 (1062 °C) is higher than the present holding temperature of 1000 °C, which might suppress efficient crystal growth. The SEM images in **Figures 3e** and **3f** show that the crystals grown in K_2SO_4 flux were monodispersed, which is in sharp contrast to the aggregated crystals prepared through the conventional solid-state reaction.[5] This contrast indicates that the K_2SO_4 mixture was molten or partly molten during the crystal growth thanks to the coexistence of TiO_2 and LiOH, both of which might lower the melting point of K_2SO_4.

In summary, Na_2SO_4 was found to be the best choice among various sulfate- and halide-based fluxes for growing large, platy β-Li_2TiO_3 crystals with faceted surface features. I explore the optimal crystal growth conditions in Na_2SO_4 flux in terms of solute concentration and holding time, and study the corresponding growth process.

3.3.2 Growth of β-Li_2TiO_3 crystals from Na_2SO_4 flux

I first studied the flux growth of β-Li_2TiO_3 crystals from Na_2SO_4 flux at 900 °C, because the melting point of Na_2SO_4 is 880 °C. **Figures 3.7** and **3.8** show the XRD pattern and SEM image of the resulting β-Li_2TiO_3 crystals, respectively. All the diffraction peaks can be indexed to β-Li_2TiO_3 phase with minor impurity phases. However, the crystals were aggregates of particulates 1.0–10.0 μm in size with no faceted surface features. Comparing the crystals grown at 900 and 1000 °C (**Figure 3.8** *vs* **Figures 3.4c and**

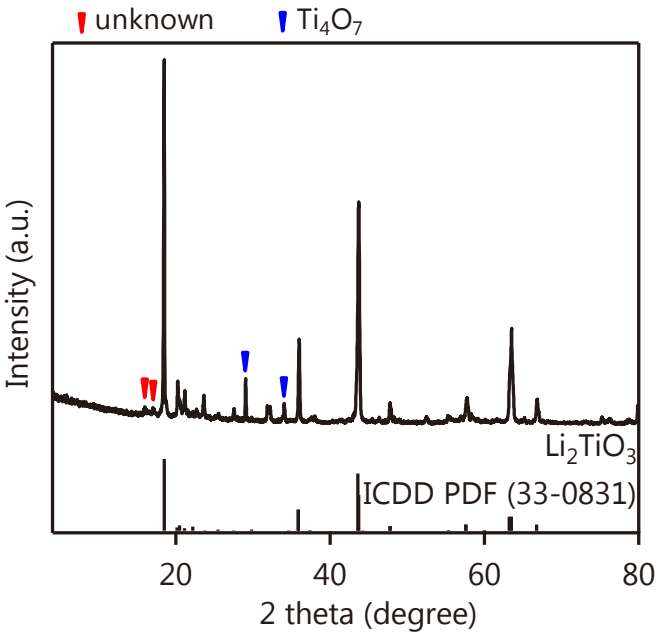

Figure 3.7 XRD pattern of β-Li_2TiO_3 crystals grown at 900 ºC. Flux, Na_2SO_4; solute concentration, 20 mol%; holding time, 10 h; cooling rate, 300 ºC h^{-1}.

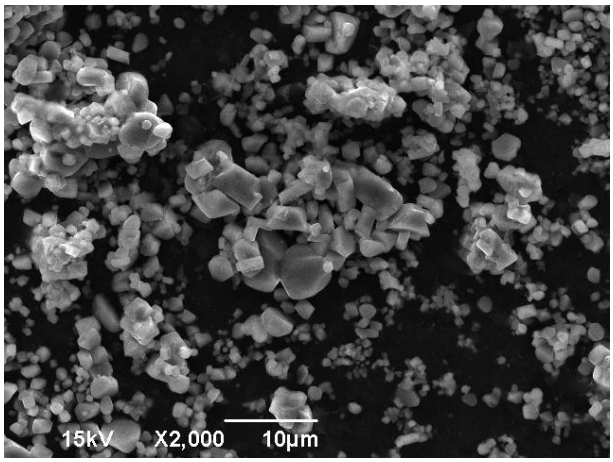

Figure 3.8 SEM image of β-Li_2TiO_3 crystals grown at 900 ºC. Flux, Na_2SO_4; solute concentration, 20 mol%; holding time, 10 h.

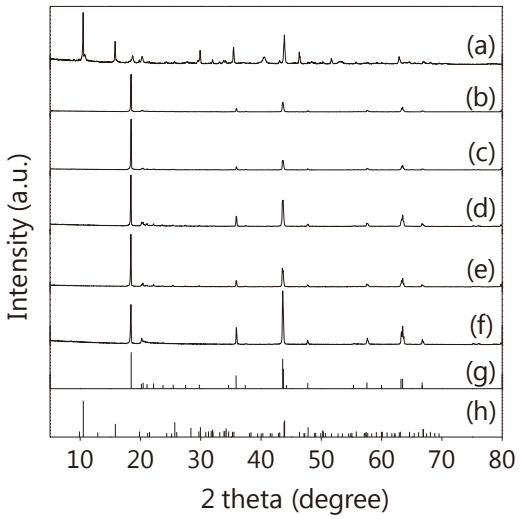

Figure 3.9 Powder XRD patterns of β-Li_2TiO_3 crystals grown from a Na_2SO_4 flux with solute concentrations of (a) 1, (b) 10, (c) 20, (d) 50, (e) 80, and (f) 100 mol%. Holding temperature, 1000 ºC; holding time, 10 h; cooling rate, 300 ºC h^{-1}. Patterns in (g) and (h) are the Powder Diffraction File (PDF) patterns of β-Li_2TiO_3 (# 33-0831) and $Na_2Ti_3O_7$ (# 31-1329) taken from the ICDD database, respectively.

3.4d), we conclude that the Na_2SO_4 flux works better at 1000 °C.

Next, I looked for the optimal solute concentrations for growing highly-faceted crystals from the Na_2SO_4 flux, with the holding temperature and time being 1000 °C and 10 h, respectively. **Figure 3.9** contains the XRD patterns of flux-grown crystals with solute concentrations of 1, 10, 20, 50, 80, and 100 mol% (Runs 3-8, 3-9, 3-2, 3-10, 3-11, and 3-12 in **Table 3.1**, respectively). Run 3-12 (100 mol%) corresponds to the condition for solid-state reaction method. At 1 mol%, the main diffraction peaks were assigned to the monoclinic $Na_2Ti_3O_7$ phase, while crystals grown at or above 10 mol% can be indexed as β-Li_2TiO_3 phase without impurity phases. ICP-OES analysis of the resulting β-Li_2TiO_3 crystals indicated that the Na/Li molar ratio in the crystals grown in Run 3-2 (**Table 3.1**) was ~0.005; therefore, the Na^+ ions were hardly incorporated into the lattice of the grown crystals.

Figure 3.10 shows the SEM images of β-Li_2TiO_3 crystals grown at the solute concentrations of 10, 20, 50, 80, and 100 mol% from the Na_2SO_4 flux. At 10 and 20 mol%, platy crystals with well-developed facets were grown, with the lateral particle size of ~15.0 μm and the aspect ratio of about 3.5 (**Figures 3.10a**, **3.10b**, **3.4c**, and

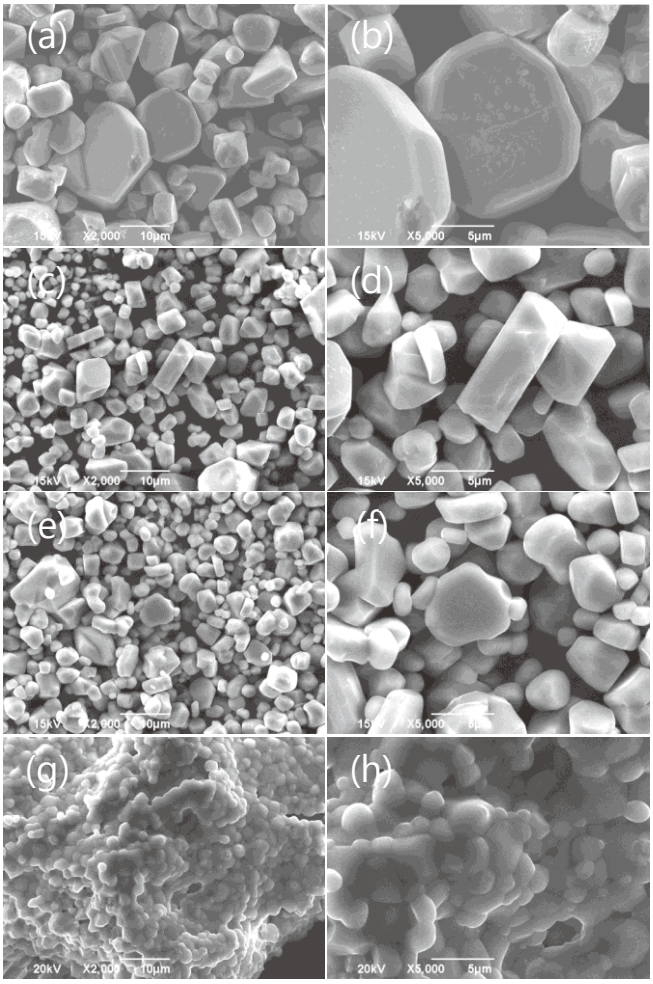

Figure 3.10 SEM images of β-Li_2TiO_3 crystals grown from Na_2SO_4 flux with solute concentrations of (a, b) 10, (c, d) 50, (e, f) 80, and (g, h) 100 mol%. Holding temperature, 1000 °C; holding time, 10 h. The SEM images of the crystals grown at the solute concentration of 20 mol% are shown in **Figures 3.4 c** and **d**.

3.4d). Increasing the solute concentrations to 50 and 80 mol% reduced both the particle size and the areas of the exposed faceted surface features (**Figures 3.10c–f**). At 100 mol%, only aggregated and irregular particles ~1.0 μm in size were yielded (Figures **3.10g and 3.10h**).

Figure 3.11 shows the effect of the solute concentration on the average particle size of the grown β-Li_2TiO_3 crystals, which was measured with a laser diffraction particle size analyzer. The average size of β-Li_2TiO_3 crystals decreased almost monotonically from ~15.0 to ~6.0 μm with increasing solute concentrations.

Herein I discuss the changes in the particle size and shape of β-Li_2TiO_3 crystals grown using different solute concentrations. The final crystal size is expected to depend

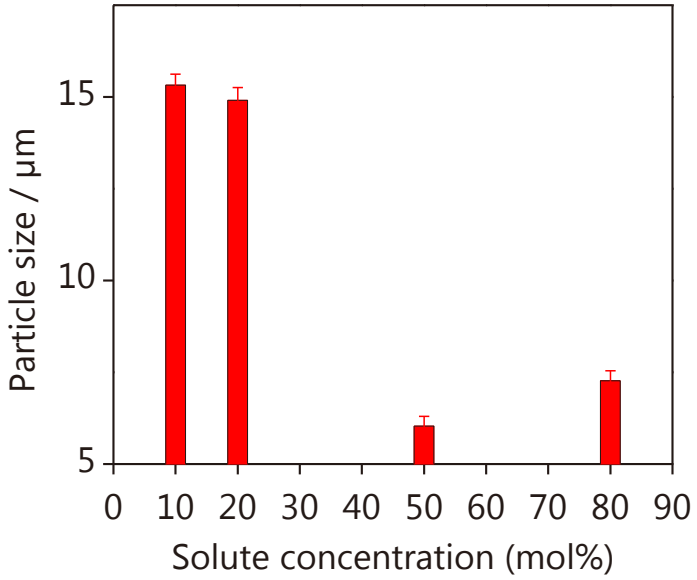

Figure 3.11 Solute concentration dependence of average particle size of β-Li_2TiO_3 crystals grown from a Na_2SO_4 flux. Holding temperature, 1000 ºC; holding time, 10 h; cooling rate, 300 ºC h^{-1}. The average particle size was analyzed by a laser diffraction particle size analyzer.

on the formation frequency of the β-Li_2TiO_3 nuclei as well as growth rate of the β-Li_2TiO_3 crystals from the flux. As the solute concentration increases, more β-Li_2TiO_3 nuclei are formed. The formed nuclei are then dissolved and recombined to yield larger crystals through the so-called Ostwald ripening process. The formation of large β-Li_2TiO_3 crystals at solute concentrations of 10–20 mol% could be due to the Ostwald ripening. On the other hand, the shapes of the grown crystal particles could be explained by the interaction between the specific surface of β-Li_2TiO_3 crystals and the flux species (*e.g.*, Li^+, Na^+, and SO_4^{2-}). One possible explanation for the platy crystal morphology at 20 mol% is the adsorption of Na^+ on the specific surface, which could suppress the crystal growth along the *c*-axis. A detailed explanation of this point is given in the next section. Similar preferential adsorption of ions and molecules that leads to anisotropic growth of crystals is recognized in the crystal growth of oxides, oxynitrides, and fluorides.[21,26-28]

Then, I examined the effect of the holding time (Runs 3-2, 3-13, 3-14, and 3-15 in **Table 3.1**) on the growth of β-Li_2TiO_3 crystals, in order to understand the growth mechanism of the platy crystals. **Figure 3.12** shows the XRD patterns of flux-grown

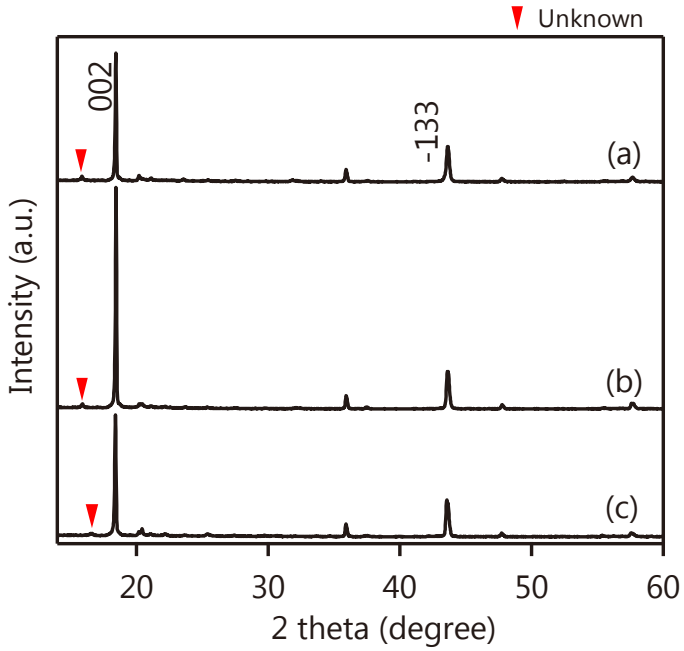

Figure 3.12 XRD patterns of β-Li_2TiO_3 crystals flux-grown for (a) 0, (b) 5, and (c) 30 h. Flux, Na_2SO_4; solute concentration, 20 mol%; holding temperature, 1000 ºC; cooling rate, 300 ºC h^{-1}. In comparison the XRD pattern of flux-grown β-Li_2TiO_3 crystals for 10 h is shown in **Figure 3.2b**.

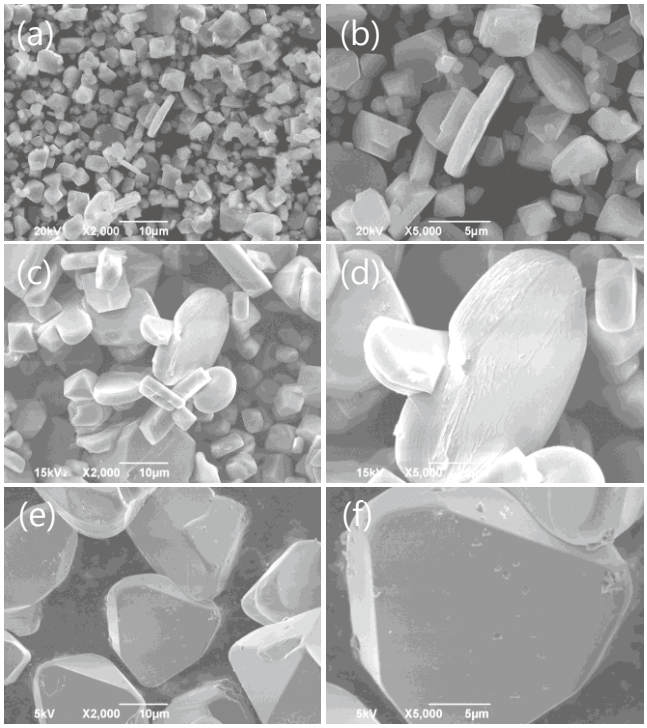

Figure 3.13 SEM images of β-Li_2TiO_3 crystals grown in Na_2SO_4 flux for (a, b) 0 and (c, d) 5 h. Solute concentration, 20 mol%; holding temperature, 1000 °C. The SEM images of crystals grown for 10 h are shown in **Figures 3.4c** and **3.4d**.

crystals with holding time ranging from 0 to 30 h at the solute concentration of 20 mol%.

These crystals prepared with different holding times have nearly the same diffraction patterns.

Figure 3.13 shows the SEM images of β-Li_2TiO_3 crystals grown at 1000 °C for the holding times of 0, 5, and 30 h. The crystal size increased up to ~15 μm with increasing holding time, although the change was small after 10 h. At 0 h, both platy and spherical

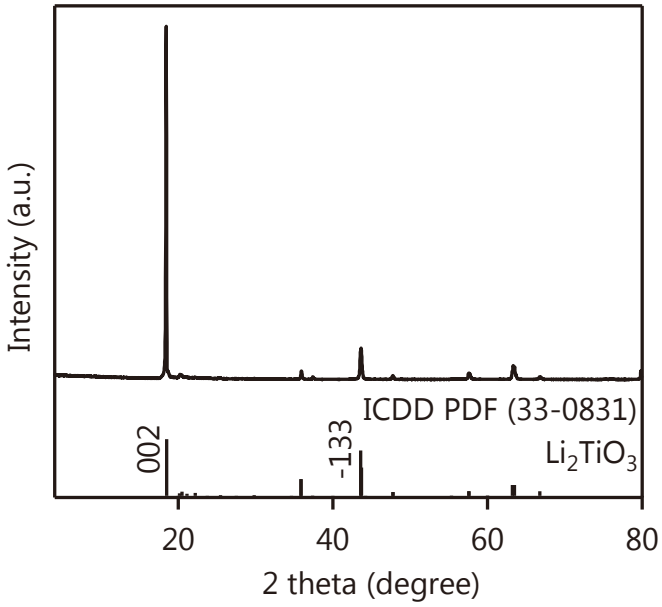

Figure 3.14 XRD pattern of β-Li_2TiO_3 crystals grown from a Na_2SO_4 flux with a cooling rate of 5 ºC h^{-1} together with the Powder Diffraction File (PDF) pattern of β-Li_2TiO_3 (# 33-0831). Solute concentration, 20 mol%; holding temperature, 1000 ºC; holding time, 10 h. In comparison the XRD pattern of β-Li_2TiO_3 crystals grown with a cooling rate of 300 ºC h^{-1} is shown in **Figure 3.2b**.

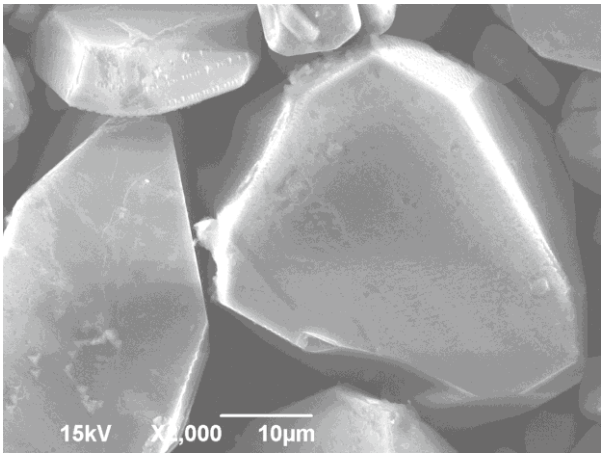

Figure 3.15. SEM image of β-Li_2TiO_3 crystals grown from a Na_2SO_4 flux with a cooling rate of 5 ºC h^{-1}. Solute concentration, 20 mol%; holding temperature, 1000 ºC, holding time, 10 h. In comparison the SEM image of β-Li_2TiO_3 crystals grown with a cooling rate of 300 ºC h^{-1} is shown in **Figure 3.4c**.

β-Li_2TiO_3 crystals were formed (**Figures 3.13a** and **3.13b**). When the holding time was increased to 5–30 h, large, faceted β-Li_2TiO_3 crystals (10.0–15.0 μm in lateral size) were formed instead.

The effect of cooling rate (Runs 3-2 and 3-16 in **Table 3.1**) on the growth of the β-Li_2TiO_3 crystals was examined, in order to investigate the growth process in the Na_2SO_4 flux system. **Figure 3.14** shows the XRD patterns of crystals grown at 1000 °C with a cooling rate of 5 ºC h^{-1} and reference. All diffraction peaks are indexed as the single phase of β-Li_2TiO_3. In the SEM image of the same sample (**Figure 3.15**), the crystal size was about 20.0–30.0 μm in the lateral direction, which was two times larger than that (10.0–15.0 μm) grown with the cooling rate of 300 ºC h^{-1}. The diving force of crystal growth is the concentration or temperature gradient induced by the cooling. Therefore, a slower cooling rate suppressed the formation of β-Li_2TiO_3 crystal nuclei, allowing the efficient growth of larger crystals.

3.3.3 Possible growth mechanism of platy and faceted β-Li_2TiO_3 crystals from Na_2SO_4 flux

I carried out TEM analysis on the β-Li_2TiO_3 crystals grown with solute concentration of 20 mol% for 10 h (Run 3-2 in **Table 3.1**) to determine the crystal plane of the exposed

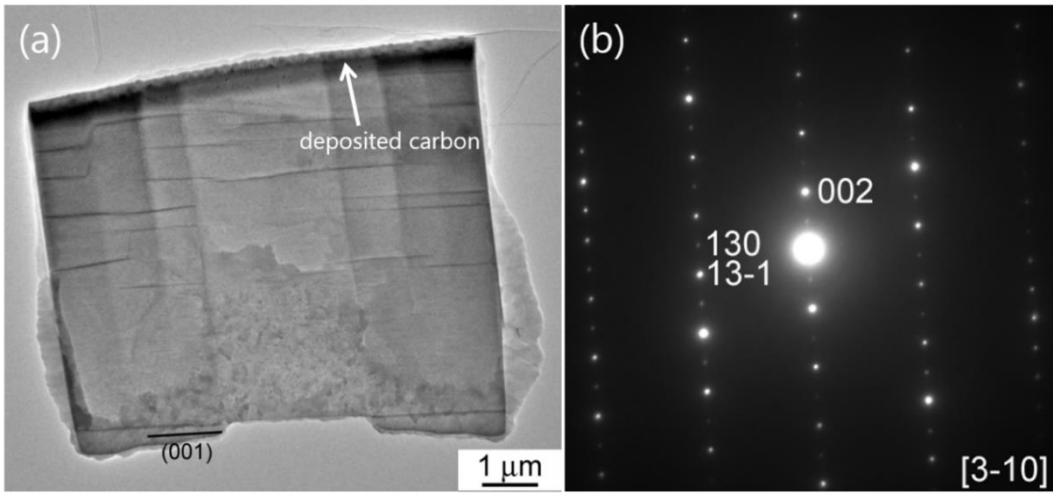

Figure 3.16 (a) TEM image and (b) the corresponding SAED pattern of the cross section of a plate-like β-Li_2TiO_3 crystal grown from Na_2SO_4 flux. Solute concentration, 20 mol%; holding temperature, 1000 ºC; holding time, 10 h; cooling rate, 300 ºC h^{-1} (Run 3-2 in **Table 3.1**).

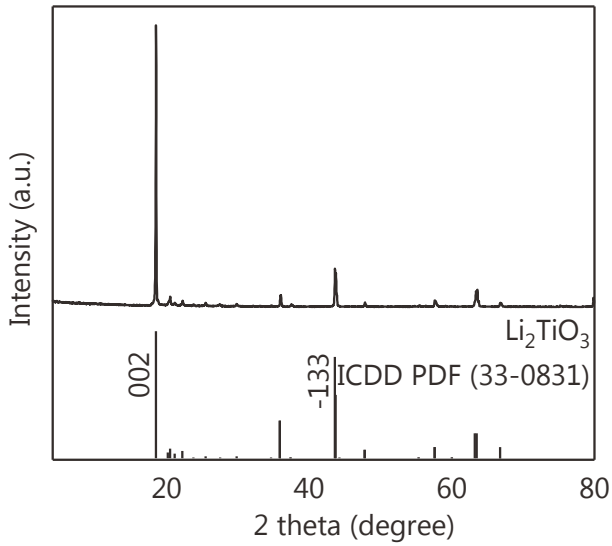

Figure 3.17 XRD pattern of faceted β-Li_2TiO_3 crystals flux-grown at 1000 ºC without grinding together with the powder diffraction file (PDF) pattern of β-Li_2TiO_3 taken from the ICDD database. Solute concentration, 20 mol%; holding time, 10 h; cooling rate, 300 ºC h^{-1}.

surface of crystals. One typical platy β-Li_2TiO_3 particle was selected and processed as described in the experimental section. **Figure 3.16** shows the obtained bright-field TEM image and SAED pattern. The highly ordered diffraction spots, taken along the [3-10] direction, indicate that the crystal possessed a single crystalline nature. The analysis of the exposed facets indicated that the dominant exposed crystal plane is the {001} plane. **Figure 3.17** shows the XRD pattern of the corresponding unmilled β-Li_2TiO_3 crystals. The intensity ratio of (002) to (-133) diffraction peak in the XRD pattern is 6.3, a value that is markedly higher than that obtained from the International Centre for Diffraction Data (ICDD) Powder Diffraction File (PDF # 33-0831, ~1.3). This result indicated again the anisotropic growth of β-Li_2TiO_3 crystals. From electron and X-ray diffraction, it can be concluded that the dominant facet of the present β-Li_2TiO_3 crystals is {001} plane.

The Rietveld refinement was carried out to obtain lattice parameters of the Na_2SO_4 flux-grown β-Li_2TiO_3 crystals (Run 3-2 in **Table 3.1**). **Figure 3.18** shows the experimental and calculated patterns, as well as their difference. The refinement results are summarized in **Table 3.3**. The lattice parameters of these crystals were determined to be a = 5.133(13) nm, b = 8.89(2) nm, c = 9.86(2) nm, and β = 99.935(17)º. These values are in good agreement with the literature values of a = 5.0623(5) nm, b = 8.7876(9) nm, c = 9.7533(15) nm, and β = 100.212(11)º.[9]

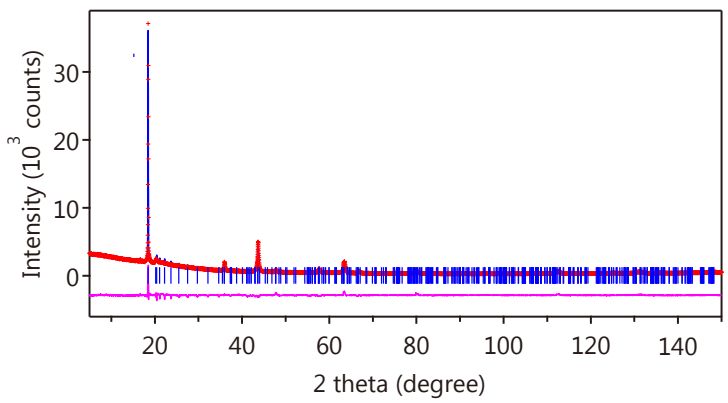

Figure 3.18 The observed (+ in red), calculated (blue vertical line), and the difference (pink line) profiles of β-Li_2TiO_3 grown at 1000 °C for the Rietveld refinement. The vertical lines in blue show positions calculated for the Bragg reflection. Solute conc., 20 mol%, holding time, 10 h; cooling rate, 300 ºC h^{-1}.

Table 3.3 Crystal Data and Rietveld Refinement Results for the Flux-Grown β-Li_2TiO_3 with Solute Concentration of 20 mol% for 10 h (Run 3-2 in **Table 3.1**)

Empirical chemical formula	Li_2TiO_3
system	monoclinic
a (nm)	5.133(13)
b (nm)	8.89(2)
c (nm)	9.86(2)
β (°)	99.935(17)
R_{wp} (%)[a]	7.13
R_e (%)[b]	3.49
R_p (%)	4.69
GOF[c]	2.04

[a] R_{wp} is a weighted-profile R value with the contrubution of background, [b] R_e is an expected R value and reflects the quality of the data (*i.e.*, the counting statistics), [c] GOF is R_{wp}/R_e (goodness-of-fit).

According to the runs using different solute concentrations and holding times, the possible growth mechanism of the platy, {001}-faceted β-Li_2TiO_3 crystals, was deduced. At 900 °C (Run 3-7, **Table 3.1**), the Na_2SO_4 flux began to melt and the solutes reacted with each other to yield particulate β-Li_2TiO_3 crystals via solid state reaction. These particles have undefined morphology and a wide size distribution as shown in **Figure 3.8**. The reason is that, near the melting point of Na_2SO_4 (880 °C), the β-Li_2TiO_3 crystals are barely dissolved in the flux, and the Ostwald ripening process cannot

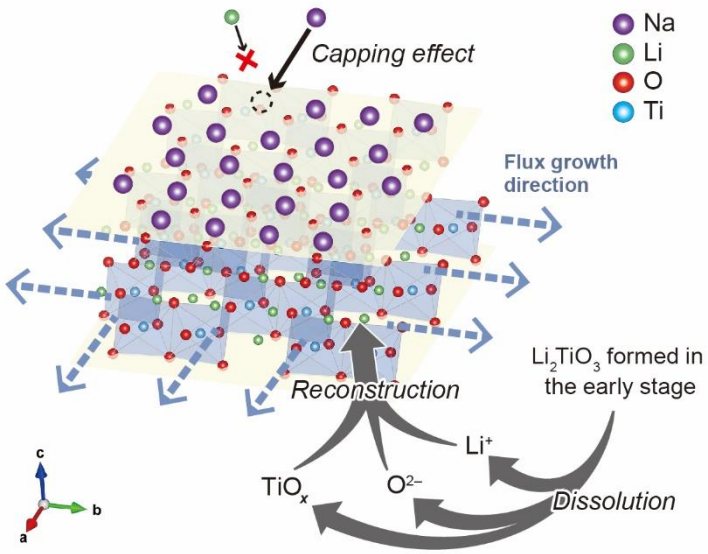

Figure 3.19 Schematic of growth mechanism for platy, {001}-faceted β-Li_2TiO_3 single crystals from Na_2SO_4 flux.

proceed. At 1000 °C, three processes are simultaneously accelerated in the Na_2SO_4 flux: (i) the reactant (solute) diffusion, (ii) the dissolution and redeposition of resultant β-Li_2TiO_3 crystals (Ostwald ripening), and (iii) the crystallization and growth of {001}-faceted β-Li_2TiO_3 crystals were simultaneously accelerated in the Na_2SO_4 flux. The solvation of the O^{2-} ions by the Na_2SO_4 flux can be correlated with process (iii).

Figure 3.19 schematically illustrates the possible growth mechanism of the platy {001}-faceted β-Li_2TiO_3 crystals from a Na_2SO_4 flux. At the early stage of faceted β-Li_2TiO_3 crystal growth, aggregated crystals 1.0–10.0 μm in size are formed between 900 and 1000 °C. With an increase in holding temperature to 1000 °C and holding time to 10 h, the aggregated crystals are partly dissolved in the flux to yield Li^+, O^{2-}, and $[TiO_{2+x}]^{x-}$ species. The resulting O^{2-} ions are solvated by the sulfate anions. Under the low solute concentration (10-20 mol%), the Li^+ as well as dominant Na^+ are enforced to attach to the negatively-charged {001} surfaces of β-Li_2TiO_3 crystals as a result of electrostatic interaction. The adsorption and ion exchange reactions reach equilibrium, and the Na^+ cations are preferentially adsorbed on the {001} surfaces. This capping behavior could be due to the higher adsorption enthalpy of Na^+ on the surface compared with Li^+,[29] as a result of the larger ionic radii of Na^+ (0.102 nm versus 0.076 nm for Li^+ in six coordination).[30] Owing to this capping effect and the high solubility of solutes in the Na_2SO_4 flux, the Li^+ ions are forced to migrate to the side surfaces of the crystals, where they react with the dissolved $[TiO_{2+x}]^{x-}$ and O^{2-} species for efficient construction of the Li_2TiO_3 frameworks. This reconstruction reaction leads to the observed anisotropic, {001}-faceted crystal growth. These concerted effects of sodium cations and sulfate anions would be the key for the growth of {001}-faceted β-Li_2TiO_3 crystals in the present study.

3.4 Conclusions

The flux growth of β-Li_2TiO_3 crystals from alkali metal salt-based fluxes was systematically studied. Among various fluxes (LiCl, NaCl, KCl, Li_2SO_4, K_2SO_4, and Na_2SO_4), Na_2SO_4 was found most suitable for growing large, faceted β-Li_2TiO_3 crystals,

owing to its capability to dissolve the precursor and product oxides and solvate the resulting O^{2-} ions. The runs conducted using Na_2SO_4 at 1000 °C indicated that the solute concentration of 20 mol% was favorable for growing platy, faceted β-Li_2TiO_3 crystals with a lateral size of ~15.0 μm and an aspect ratio of ~3.5. Crystals grown under these conditions (Na_2SO_4, 1000 °C, and 20 mol% solute) with variable holding times and cooling rate demonstrated the anisotropic growth of the faceted crystals. A slower cooling rate leads to the growth of large, faceted crystals. TEM images with clear electron diffraction spots showed that the resulting β-Li_2TiO_3 crystals were single crystals with dominating {001} facets. This unique anisotropic growth of β-Li_2TiO_3 crystals could be explained by the concerted effects of Na^+ capping the {001} crystal planes of β-Li_2TiO_3, and the dissolution of oxides and solvation of O^{2-} ions by SO_4^{2-} in the flux.

References

(1) Avila, R. E.; Pena, L. A.; Jimenez, J. C. Surface desorption and bulk diffusion models of tritium release from Li_2TiO_3 and Li_2ZrO_3 pebbles. *J. Nucl. Mater.* **2010**, *405*, 244–251.

(2) Kawagoe, T.; Nishikawa, M.; Baba, A.; Beloglazov, S. Surface inventory of tritium on Li_2TiO_3. *J. Nucl. Mater.* **2001**, *297*, 27–34.

(3) Padhy, R.; Rao A., N.; Parashar, S. K. S.; Parashar, K.; Chaudhuri, P. Sintering effect on electrical properties of Li_2TiO_3. *Solid State Ionics* **2014**, *256*, 29–37.

(4) Zhang, L.; Zhou, D.; He, G.; Wang, F.; Zhou, J. Effect of crystal phases of titanium dioxide on adsorption performance of H_2TiO_3-lithium adsorbent. *J. Mater. Lett.* **2014**, *135*, 206–209.

(5) Chitrakar, R.; Makita, Y.; Ooi, K.; Sonoda, A. Lithium recovery from salt lake brine by H_2TiO_3. *Dalton Trans.* **2014**, *43*, 8933–8939.

(6) Kleykamp, H. Phase equilibria in the Li-Ti-O system and physical properties of Li_2TiO_3. *Fusion Eng. Des.* **2002**, *61–62*, 361–366.

(7) Laumann, A.; Fehr, K. T.; Boysen, H.; Hoelzel, M.; Holzapfel, M. Temperature-dependent structural transformations of hydrothermally synthesized cubic Li_2TiO_3 studied by *in-situ* neutron diffraction. *Zeitschrift fur Krist.* **2011**, *226*, 53–61.

(8) Dorrian, J. F.; Newnham. R. E. Refinement of the Structure of Li_2TiO_3. *Mat. Res. Bull.* **1969**, *4*, 179–184.

(9) Kataoka, K.; Takahashi, Y.; Kijima, N.; Nagai, H.; Akimoto, J.; Idemoto, Y.; Ohshima, K. Crystal growth and structure refinement of monoclinic Li_2TiO_3. *Mater. Res. Bull.* **2009**, *44*, 168–172.

(10) Momma, K.; Izumi, F. VESTA 3 for three-dimensional visualization of crystal, volumetric and morphology data. *J. Appl. Cryst*. **2011**, *44*, 1272–1276.

(11) Fehr, T.; Schmidbauer, E. Electrical conductivity of Li_2TiO_3 ceramics. *Solid State Ionics* **2007**, *178*, 35–41.

(12) Vijayakumar, M.; Kerisit, S.; Yang, Z.; Graff, G. L.; Liu, J.; Sears, J. A; Burton, S. D.; Rosso, K. M.; Hu, J. Combined ^{6,7}Li NMR and Molecular Dynamics Study of Li Diffusion in Li_2TiO_3. *J. Phys. Chem. C* **2009**, *113*, 20108–20116.

(13) Islam, M. M.; Bredow, T. Lithium Diffusion Pathways in β-Li_2TiO_3: A Theoretical Study. *J. Phys. Chem. C* **2016**, *120*, 7061–7066.

(14) Zhang, Q. H.; Li, S. P.; Sun, S. Y.; Yin, X. S.; Yu, J. G. Lithium selective adsorption on low-dimensional titania nanoribbons. *Chem. Eng. Sci.* **2010**, *65*, 165–168.

(15) Deptuła, A.; ŁAda, W.; Olczak, T.; Sartowska, B.; Chmielewski, A. G.; Alvani, C.; Casadio, S. Preparation of lithium titanate by sol-gel method. *Nukleonika* **2001**, *46*, 95–100.

(16) Bugaris, D. E.; zur Loye, H.-C. Materials Discovery by Flux Crystal Growth: Quaternary and Higher Order Oxides. *Angew. Chem. Int. Ed.* **2012**, *51*, 3780-3811.

(17) Kanatzidis, M. G., Pottgen, R., Jeitschko W. The Metal Flux: A Preparative Tool for The Exploration of Intermetallic Compounds. *Angew. Chem. Int. Ed.* **2005**, *44*, 6996–7023.

(18) Mizuno, Y.; Zettsu, N.; Yubuta, K.; Sakaguchi, T.; Saito, T.; Wagata, H.; Oishi, S.; Teshima, K. Fabrication of $LiCoO_2$ Crystal Layers Using a Flux Method and Their Application for Additive-Free Lithium-Ion Rechargeable Battery Cathodes. *Cryst. Growth Des.* **2014**, *14*, 1882–1887.

(19) Kimijima, T.; Zettsu, N.; Teshima, K. Growth Manner of Octahedral-Shaped $Li(Ni_{1/3}Co_{1/3}Mn_{1/3})O_2$ Single Crystals in Molten Na_2SO_4. *Cryst. Growth Des.* **2016**, *16*, 2618–2623.

(20) Hayashi F.; Kurokawa, S.; Shiiba H.; Wagata, H.; Yubuta, K.; Oishi S., Nishikiori, H.; Teshima, K. Exceptional Flux Growth and Chemical Transformation of Metastable Orthorhombic $LiMnO_2$ Cuboids into Hierarchically-Structured Porous. $H_{1.6}Mn_{1.6}O_4$ Rods as Li Ion Sieves. *Cryst. Growth Des.* **2016**, *16*, 6178–6185.

(21) Mann, A. K. P.; Fu, J.; DeSantis, C. J.; Skrabalak, S. E. Spatial and Temporal Confinement of Salt Fluxes for the Shape-Controlled Synthesis of Fe_2O_3 Nanocrystals. *Chem. Mater*. **2013**, *25*, 1549–1555.

(22) Bakshi, M. S. How Surfactants Control Crystal Growth of Nanomaterials. *Cryst. Growth Des*. **2016**, *16*, 1104−1133.

(23) Boltersdorf J., King, N., Maggard, P. A. Flux-Mediated Crystal Growth of Metal Oxides: Synthetic Tunability of Particle Morphologies, Sizes, and Surface Features for Photocatalysis Research. *CrystEngComm* **2015**, *17*, 2225-2241

(24) Hayashi, Y.; Kimura, T.; Yamaguchi, T. Preparation of acicular NiZn-ferrite powders. *J. Mater. Sci.* **1986**, *21*, 2876–2880.

(25) Cortese, A. J.; Abeysinghe, D.; Wilkins, B.; Smith, M. D.; Rassolov, V.; zur Loye, H.-C. Oxygen Anion Solubility as a Factor in Molten Flux Crystal Growth, Synthesis, and Characterization of Four New Reduced Lanthanide Molybdenum Oxides: $Ce_{4.918(3)}Mo_3O_{16}$, $Pr_{4.880(3)}Mo_3O_{16}$, $Nd_{4.910(3)}Mo_3O_{16}$, and $Sm_{4.952(3)}Mo_3O_{16}$. *Cryst. Growth Des.* **2016**, *16*, 4225−4231.

(26) Sullivan, I.; Sahoo, P. P.; Fuoco, L.; Hewitt, A. S.; Stuart, S.; Dougherty, D.; Maggard, P. A. Cu-Deficiency in the *p*-Type Semiconductor $Cu_{5-x}Ta_{11}O_{30}$: Impact on Its Crystalline Structure, Surfaces, and Photoelectrochemical Properties. *Chem. Mater.* **2014**, *26*, 6711– 6721.

(27) Hojamberdiev, M.; Yubuta, K.; Vequizo, J. J. M.; Yamakata, A.; Oishi, S.; Domen, K.; Teshima, K. NH_3-Assisted Flux Growth of Cube-like $BaTaO_2N$ Submicron Crystals in a Completely Ionized Nonaqueous High-Temperature Solution and Their Water Splitting Activity. *Cryst. Growth Des.* **2015**, *15*, 4663–4671.

(28) Zhao, Q., Shao, B., Lü, W., Jia, Y., Lv, W., Jiao, M., You, H. Ba_2GdF_7 Nanocrystals: Solution-Based Synthesis, Growth Mechanism, and Luminescence Properties. *Cryst. Growth Des.* **2014**, *14*, 1819–1826.

(29) Xiao, X., Hayashi, F., Shiiba, H., Selcuk, S., Ishihara, K., Namiki, K., Shao, L., Nishikiori, H., Selloni, A., Teshima, K. Platy $KTiNbO_5$ as a Selective Sr Ion

Adsorbent: Crystal Growth, Adsorption Experiments, and DFT Calculations. *J. Phys. Chem. C* **2016**, *120*, 11984–11992.

(30) Shannon, R. D. Revised Effective Ionic Radii and Systematic Studies of Interatomic Distances in Halides and Chalcogenides. *Acta Crystallogr. Sect. A* **1976**, *32*, 751–767.

Chapter 4
Growth of platy $KTiNbO_5$ crystals from KNO_3 flux as a selective strontium ion adsorbent

Chapter 4 Growth of platy $KTiNbO_5$ crystals from KNO_3 flux as a selective strontium ion adsorbent

4.1 Introduction

Nuclear power is an attractive form of energy because of its high efficiency and no greenhouse gas emission, but it creates tremendous amounts of waste containing radioactive ions (~2300 tons per year).[1] Among the radioactive nuclides, $^{90}Sr^{2+}$ (a byproduct of nuclear fission reactions) is one of the most hazardous and long-lived byproducts (half-life = ~29 years).[1] Therefore, selective removal of radioactive Sr^{2+} ions from aqueous wastes is an important challenge in energy and environmental science. Understanding the interface processes between adsorbates and adsorption sites of adsorbents is central to selective removal applications. Similar to cyclic organic compounds, such as crown ethers,[2] calixarenes,[3] and cucurbiturils,[4] supramolecules,[5] and metal-organic frameworks,[6] certain inorganic layered compounds can selectively capture target ions, although information about the capture mechanism is still limited.[7]

Compared with organic resins that are potentially damaged by the hydrolysis of functional groups under extreme conditions, inorganic ion-exchangers show superior chemical stability and specific ion selectivity without any special treatments thanks to their unique rigid porous frameworks (*i.e.*, tunnel, layered, and cage structures). Accordingly, various natural and synthetic inorganic ion-exchangers have been investigated for separation of Sr^{2+} ions from radioactive wastes, such as aluminosilicates,[8] titanosilicates (often called crystalline silicotitanate),[9] Sandia octahedral molecular sieves ($Na_2Nb_{2-x}(Ti/Zr)_xO_{6-x}(OH)_x \cdot H_2O$ (x = 0–0.4)),[10] Sb-doped silicates,[11] layered metal sulfides,[12,13] layered titanates ($Na_4Ti_9O_{20} \cdot nH_2O$[14] and $Na_2Ti_3O_7$),[15] niobate ($K_4Nb_6O_{17}$),[16] and thiostannate.[17] The chemical and adsorption

properties of these ion exchangers are summarized in **Table 4.1**. The key issues for $^{90}Sr^{2+}$ ion exchangers are their selectivity for the Sr^{2+} ion and their chemical stability under low pH conditions, because waste effluent is a HNO_3-based acidic solution containing other ions, including the Na^+ ion.[9] Most ion exchangers are ineffective under practical conditions because some of their framework components (*i.e.*, Al, Mn, and S species) readily dissolve in acidic conditions. Therefore, new durable and selective adsorbents are needed.

Potassium titanium niobate ($KTiNbO_5$, KTN) is a layered material that is widely used as a solid acid[21] and a photocatalyst[22], but has not been investigated as a selective ion-exchanger. KTN is composed of two different MO_6 (M = Ti or Nb) metalate layers of octahedra that share edges with each other, and potassium cations are located in the corner of the gallery to compensate for the negatively-charged frameworks.[23] The zigzag layered nanostructure of KTN is similar to that of sodium titanate, $Na_2Ti_3O_7$, which can capture Sr^{2+} ions at the corner positions of interlayers, even though with an efficiency of only 19% of the theoretical cation-exchange capacity (CEC).[15] I thus expect that the distorted subnanometer-sized pockets constructed by eight terminal oxygen ions of $(Nb/Ti)O_6$ octahedral units are favorable adsorption sites for Sr^{2+} (see **Figure 4.1)**. In addition, the high oxidation state of Nb(V) in KTN increases the charge density of the anionic slabs with respect to $Na_2Ti_3O_7$. The resulting increase in the electrostatic interaction between exchanged cations and anionic slabs is expected to improve the preference for Sr^{2+} ions in comparison to a pure titanate.

Table 4.1 Sr^{2+} Ion Exchange Properties of Reported Inorganic Ion-Exchangers.

Entry	Sample	Cation exchange capacity (mmol g^{-1})		pH	Volume/mass ratio	$[Sr^{2+}]$	$[Na^+]$	Time	K_d^{Sr}	ref.
		Theoretical	Experimental		($mL \cdot g^{-1}$)	(ppm)	(ppm)	(h)	(10^3 $mL \cdot g^{-1}$)	
2-1	Zeolite A ($Na_2Al_2Si_3O_{10} \cdot 2H_2O$)	2.65	3.46	—[a]	5000	50–150	0	2	—[a]	8
2-2	$HK_3(TiO)_4(SiO_4)_3 \cdot 4H_2O$	—[a]	—[a]	9.6	—[a]	—[a]	0	72	52.0	18
2-3				11.2	200	<1	5	24	57.6	19
2-4	$Na_2Ti_2O_3SiO_4 \cdot 2H_2O$	3.55	3.24	~6.0	200	88	2300	240	7.8	9
2-5				~2.3	200	88	0	240	4.5	
2-6	$Na_2Nb_{1.6}Ti_{0.4}O_{5.6}(OH)_{0.4} \cdot H_2O$	—[a]	—[a]	~7.0	100	20	0	12	99.8	10
2-7				~6.0	600	20	0	4	1000.0	
2-8				~7.0	200	20	2300	4	~0.1	
2-9	$[Sb_2O_5(H_2SiO_3)_6] \cdot nH_2O$	~2.60	1.35	1.0	100–200	trace	0	~96	35.5	11
2-10				2.5	100–200	trace	2300	~96	16.0	
2-11	$K_{1.9}Mn_{0.95}Sn_{2.05}S_6 \cdot 2H_2O$	~1.60	0.90	3.2	971	4	0	12	24.9	12
2-12				~7.0	1000	5	0	12	152.0	
2-13				~13.0	971	5	2300	12	450.0	
2-14	$K_{1.8}Mg_{0.9}Sn_2S_6$	1.87	0.99	~7.0	1000	5	0	12	21.0	20
2-15				~3.0	1000	5	0	12	63.3	
2-16				~3.0	200	20	0	4	<1.0	
2-17	$K_{2x}Sn_{4-x}S_{8-x}$	1.45	1.16	~7.0	1000	7	2300	15	0.6	13
2-18				~2.0	1000	7	0	15	4.2	
2-19	$Na_4Ti_9O_{20} \cdot nH_2O$	2.65	2.31	6.0	100	88	0	72	56.0	14
2-20				14.4	200	<1	117300	24	0.3	19
2-21	$Na_2Ti_3O_7$	3.31	0.63	~7.0	1000	53	0	48	11.0	15
2-22				~6.0	1000	54	2300	48	0.6	
2-23	$K_4Nb_6O_{17}$	2.03	1.78[b]	6.0–7.0	1000	200	2300	48	0.6	16
2-24	$(Me_2NH_2)_{4/3}(Me_3NH)_{2/3}Sn_3S_7 \cdot 1.25H_2O$	—[a]	0.74	~7.0	1000	12	115000	12	<0.1	17

[a] Not reported, [b] Ion exchange experiments were carried out at 65 °C.

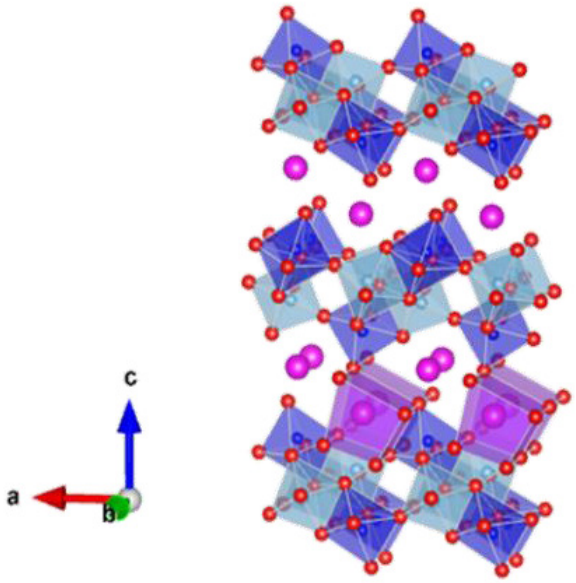

Figure 4.1 Crystal structure of $KTiNbO_6$ (orthorhombic, a = 6.447 Å, b = 3.798 Å, c = 18.389 Å). Octahedra in the gallery of $KTiNbO_6$ (purple) represent ion-exchangeable sites, in which one K^+ ion is surrounded by eight oxygen ions of $(Nb/Ti)O_6$. Crystal structure of KTN is visualized using the VESTA program.

In this work, I show that platy KTN grown from KNO_3 flux is an efficient material for the selective removal of Sr^{2+} ions at moderate temperatures. KTN exhibits remarkable durability and exceptionally high Sr^{2+}/Na^+ selectivity under low pH conditions and high concentration of Na^+ ion. The formation energies of various cation-exchanged KTN adsorbents with and without intercalated water molecules are determined by DFT calculations to understand the high preference for Sr^{2+}. The origin of the high affinity for Sr^{2+} is discussed based on the experimental and theoretical results.

4.2 Experimental section

4.2.1 Growth of $KTiNbO_5$ crystals

KTN samples were prepared according to the literature[24] but using KNO_3 (99.0%) as flux instead of KCl. A stoichiometric mixture of K_2CO_3 (99.5%), TiO_2 (anatase, 98.0%), and Nb_2O_5 (99.9%) was used as the solute, wherein the solute concentration was 20 mol%. All of the reagents were purchased from Wako Pure Chemical Industries unless

specified otherwise. Three samples of a mixture of solute and flux (~15 g) were placed in platinum crucibles with platinum lids. The crucibles were placed in an electric furnace, and then heating at 45 °C·h^{-1} and maintained at 500, 600, or 700 °C for 10 h. The samples are called KTN_{flux}-500, -600, and -700, according to the heating temperature. The products were washed with hot water (~80 °C) and then dried in air. For comparison, KTN crystals were also prepared using the solid-state reaction (SSR) method at 1100 °C for 24 h (KTN_{SSR}).[25]

4.2.2 Characterization

X-ray diffraction (XRD) patterns were recorded on a Miniflex II powder diffractometer (Rigaku) operating at 30 kV and 20 mA using Cu K_α radiation (λ = 0.15418 nm). Raman spectra were collected with a HR-Revolution spectrometer (Horiba Jobin Yvon) with a visible laser (λ = 523 nm, 50 mW). Field-emission scanning electron microscopy (FE-SEM) images were recorded at an acceleration voltage of 15 kV on a JSM-7600F spectrometer (JEOL). N_2 adsorption isotherms were obtained at −196 °C using a Belsorp Mini II sorption analyzer (BEL Japan). The KTN samples were degassed at 200 °C for 5 h prior to analysis. Thermogravimetry–differential thermal analysis (TG-DTA, Rigaku, Thermo Plus EVOII TG8120) was used to analyze the water content in the samples at a heating rate of 10 °C min^{-1}.

4.2.3 Sr^{2+} adsorption experiments

Sr^{2+} adsorption isotherms were measured by equilibrating 1.0 g of sample in 1000 mL of $SrCl_2$ aqueous solution ($[Sr^{2+}]_{initial}$ = 25–500 ppm) with stirring at room temperature. The residual $[Sr^{2+}]$ concentration was determined by inductively coupled plasma-optical emission spectrometry (ICP-OES, SPS5510, SII) after sample separation. The pH of the solution was maintained at ~7.5 using dilute HCl solution.

The Sr^{2+} adsorption isotherm was analyzed by the following three models:[26,27]

Langmuir model $$q = \frac{q_L b_L C_e}{1 + b_L C_e} \quad (4\text{-}1)$$

Freundlich model $$q = K_F C_e^{\frac{1}{n_F}} \quad (4\text{-}2)$$

Langmuir–Freundlich (LF) model $$q = \frac{q_{LF} \left(b_{LF} C_e\right)^{\frac{1}{n_{LF}}}}{1 + \left(b_{LF} C_e\right)^{\frac{1}{n_{LF}}}} \quad (4\text{-}3)$$

where q (mg·g^{-1}) is the amount of cation adsorbed at equilibrium concentration, q_L and q_{LF} are the maximum adsorbed amounts of sorbent for the Langmuir and LF models, b_L and b_{LF} are the Langmuir and LF constants, C_e (mmol·L^{-1}) is the equilibrium concentration, K_F is the Freundlich constant, and n_F and n_{LF} are constants.

The distribution coefficient K_d was used to evaluate the preference for Sr^{2+}:

$$K_d = \frac{\left(C_0 - C_e\right)}{C_e} \frac{V}{m} \quad (4\text{-}4)$$

where C_0 and C_e are the initial and equilibrium [Sr^{2+}] (mmol·L^{-1}), V is the volume (mL) of the testing solution, and m is the amount of ion-exchanger (g).

The separation factor $SF_{Sr/Na} = K_d^{Sr}/K_d^{Na}$ was calculated to evaluate the Sr^{2+}/Na^{+} selectivity. The pH dependence of K_d for Sr^{2+} (K_d^{Sr}) was investigated as follows: 100 mg of sample was dispersed in 100 mL of 2 ppm Sr^{2+} solution (initial pH = ~1–10). The initial pH of the Sr^{2+} solutions was adjusted by dilute HCl or NaOH solution. The mixtures were shaken for 18 h, followed by centrifugation for separation. The effect of [Na^{+}] on K_d was measured using the batch method with [Sr^{2+}] = 2 ppm, [Na^{+}] = 0–5000 mmol·L^{-1}, volume/mass ratio 1000 mL·g^{-1}, pH = ~7.5 or 14.0, room temperature, and shaking time 18 h.

4.2.4 DFT calculations

All calculations were performed using a supercell of 64 atoms (corresponding to $Z = 8$ of formula units) with the orthorhombic lattice of KTN. The calculated lattice constants for $KTiNbO_5$ are 6.441, 3.796 and 18.454 Å, in good agreement with the experimental values of 6.447, 3.797 and 18.431 Å, respectively.[20] To evaluate the formation energy E^F of cation-substituted KTN, The following ion-exchange reaction were considered:

$$K_8Ti_8Nb_8O_{40} + M + xH_2O \rightarrow M^{II}K_6Ti_8Nb_8O_{40}\cdot xH_2O + 2K \quad (4\text{-}5)$$

where M is Sr, Ca, Mg, or 2Na, and x = 0–2. For simplicity, zero temperature and vacuum conditions, and calculated E^F from the expression were also assumed

$$E^F = E(MK_6Ti_8Nb_8O_{40}\cdot xH_2O) + 2E(K) - 8E(KTiNbO_5) - E(M) - xE(H_2O) \quad (4\text{-}6)$$

where E(X) is the total energy of species X given by DFT. In particular, for K and M the total energy of the metallic phase at $T = 0$ K was used, rather than the chemical potentials of aqueous K^+ and M^{2+} ions. Nonetheless, as shown in the following, the simple expression, Eq. (4-6), is found sufficient for understanding the selectivity of our KTN samples.

For the DFT calculations, the Vienna *ab initio* simulation package[28,29] with the generalized gradient approximation (GGA-PBEsol)[30] and projector-augmented wave method was used.[31] The energy cutoff was 500 eV and a (4 × 3 × 1) k-point mesh was used; notice that the number of atoms in the supercell times the number of sampled k-points is larger than 1000.

4.3 Results and discussion

4.3.1 Flux growth of $KTiNbO_5$ crystals

The XRD patterns of KTN_{flux}-500, -600, and -700 are shown in **Figure 4.2**. KTN_{flux}-500 and -600 exhibit the characteristic peaks associated with the layered structure at ~9.6 °. In the pattern of KTN_{flux}-500 (**Figure 4.2(a)**), there is one peak assignable to the starting TiO_2 anatase at ~26 °. However, increasing the temperature to 600 °C resulted in this peak disappearing and instead production of single-phase KTN (**Figure 4.2b**). Unfortunately, at the higher temperature treatment of 700 °C, the peaks of the layered structure of KTN are not present (**Figure 4.2c**). It should be noted that the present optimum temperature (600 °C) is 500 °C lower than that for KTN prepared by SSR at 1100 °C.[25] For comparison, the XRD pattern of KTN_{SSR} is shown in **Figure 4.3**.

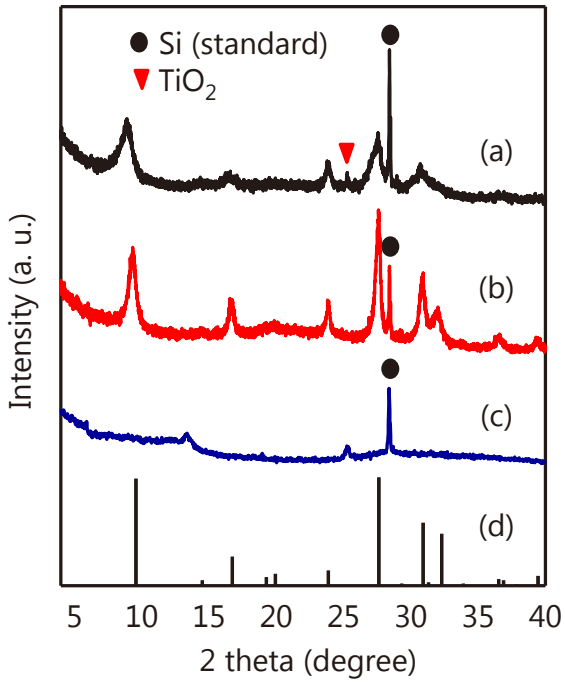

Figure 4.2 XRD patterns of KTN crystals grown from KNO_3 flux at (a) 500, (b) 600, (c) 700 °C, and (d) Powder Diffraction File pattern of KTN (#54-1155) taken from the International Centre for Diffraction Data database.

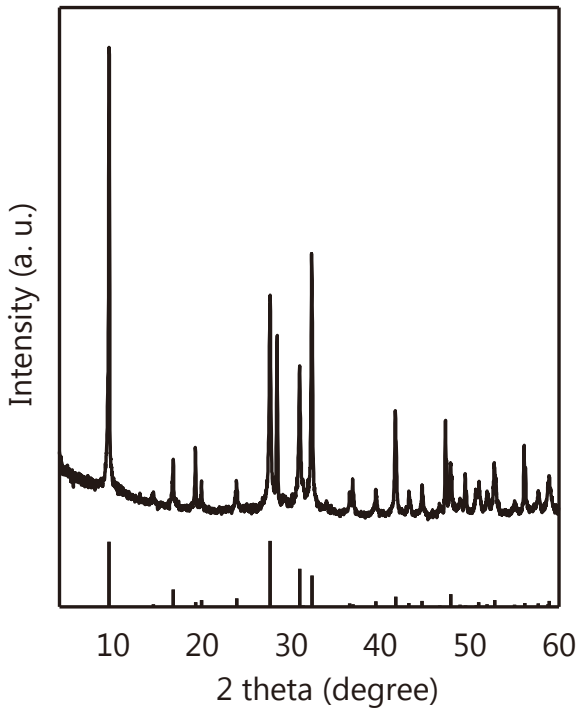

Figure 4.3 (Top) XRD pattern of the $KTiNbO_5$ crystal prepared by the solid-state reaction method and (bottom) Powder Diffraction File pattern of $KTiNbO_5$ (#54-1155) is taken from the International Centre for Diffraction Data database.

Figure 4.4a and **4.4b** show SEM images of KTN_{flux}-500 and -600. The particle morphologies of KTN_{flux}-500 and -600 are both flaky, wherein the particles are very thin (10–30 nm) and the lateral sizes are from several hundred nanometers to ~1 μm. These characteristics of KTN_{flux} are completely different from that those of KTN_{SSR} (**Figure 4.4c**), which consists of blocky particles with sizes of ~10 μm. The nitrogen adsorption isotherms of KTN_{flux}-500, KTN_{flux}-600, and KTN_{SSR} are shown in **Figure 4.5**. The Brunauer–Emmett–Teller (BET) surface areas of KTN_{flux}-500 and -600 are 86 and 48 $m^2 \cdot g^{-1}$, respectively, while that of KTN_{SSR} is <1 $m^2 \cdot g^{-1}$ (an accurate BET surface area was not obtained under the same measurement conditions). This large difference in the surface area is correlated with the crystal growth method. Namely, the use of the KNO_3 flux method enables efficient, anisotropic crystal growth at lower temperature than the SSR method, leading to 10–30 nm thick particles. The large surface area and plate-like morphology of KTN_{flux} are amenable to rapid removal of Sr^{2+} ion, which will be explained in the next section.

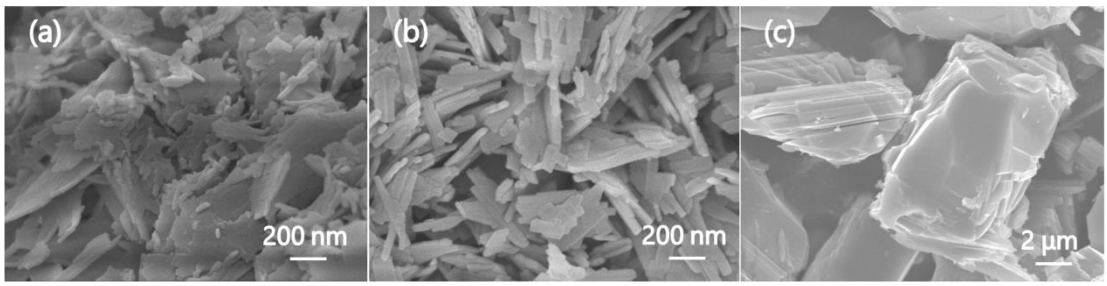

Figure 4.4 FE-SEM images of KTN crystals grown from KNO_3 flux at (a) 500 and (b) 600 °C, and (c) prepared by SSR at 1100 °C.

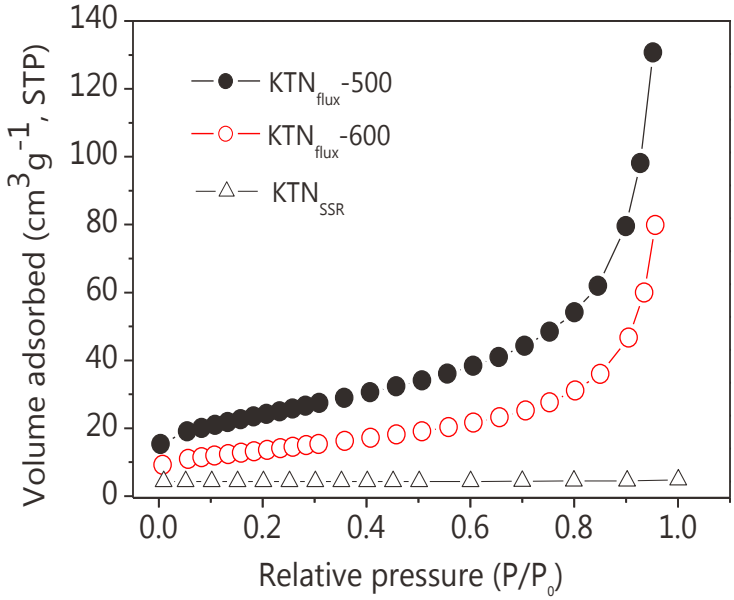

Figure 4.5 Nitrogen adsorption isotherms on $KTiNbO_5$ grown from KNO_3 flux at 500 (KTN_{flux}-500) and 600 °C (KTN_{flux}-600), and that prepared by the solid-state reaction method at 1100 °C (KTN_{SSR}). The BET surface areas of KTN_{flux}-500 and KTN_{flux}-600 are 86 and 48 $m^2\ g^{-1}$, respectively, while that of KTN_{SSR} is <1 $m^2\ g^{-1}$.

4.3.2 Sr^{2+} adsorption on $KTiNbO_5$ crystals

Figure 4.6 shows the Sr^{2+} adsorption isotherm on KTN_{flux}-600. The isotherm is classified as a type-L curve according to the Giles classification.[26] The isotherm was analyzed using the Langmuir, Freundlich, and Langmuir–Freundlich (LF) models.

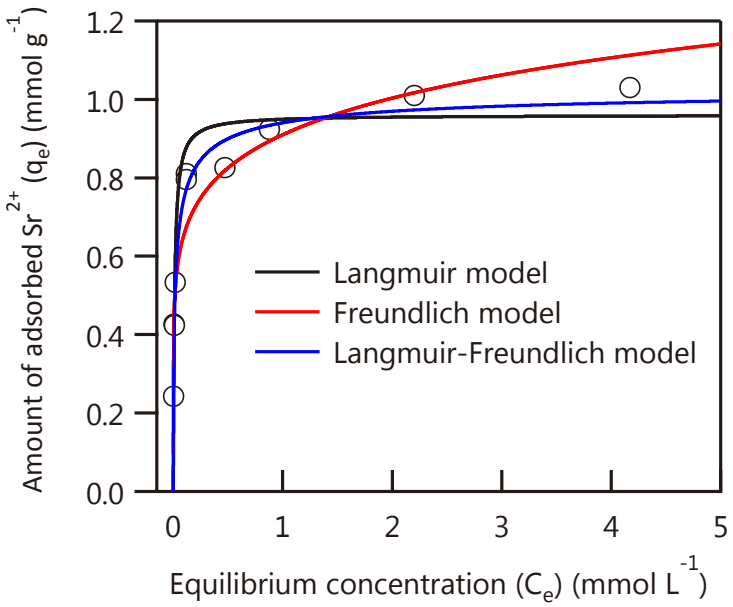

Figure 4.6 Equilibrium adsorption isotherm for adsorption of Sr^{2+} on KTN grown from KNO_3 at 600 °C. The lines represent the fitting of the data with Langmuir (black), Freundlich (red) and Langmuir–Freundlich (blue) isotherm models. Conditions: pH ~7.5, volume/mass ratio ~1000 mL·g^{-1}, $[Sr^{2+}]_{initial}$ = 25–500 ppm, room temperature.

The fitting results are summarized in **Table 4.2** and the simulated curves are shown in **Figure 4.6**. The sum of mean squared errors for the Langmuir and Freundlich models are 0.94 and 0.89. These relatively low values could be associated to the presence of several types of adsorption sites in the interlayers and on the surface. Note that the Langmuir model fits the data better than the Freundlich model. The Freundlich model assumes that adsorption occurs on a heterogeneous surface, where the adsorption energy exponentially decreases with decreasing number of adsorption sites.[27] In contrast, the Langmuir model assumes that all adsorption sites are equivalent and homogenous and a monolayer forms on the surface, and the adsorption energy is independent of the occupation of adsorption sites. The experimental isotherm is best fitted by the LF model, which is a three-parameter hybrid model that is capable of dealing with both homogeneous and heterogeneous ion-exchange sites. These fitting results indicate that most of the adsorption sites on KTN_{flux}-600 are homogeneous and inherently present in the interlayers. The maximum Sr^{2+} ion-exchange capacity of KTN_{flux}-600 was determined to be 1.04 mmol·g^{-1} according to the LF fitting. This capacity is 54% of the theoretical CEC of KTN (1.92 mmol·g^{-1} for bivalent ions based

on the chemical formula), and is comparable with those of existing efficient Sr^{2+} adsorbents (see **Table 4.1**).

Table 4.2 Fitting Parameters for the Langmuir, Freundlich, and Langmuir–Freundlich (LF) Models for $KTiNbO_5$ Grown from KNO_3 Flux at 600 °C[a]

Model	q_L (mmol·g^{-1})	b_L (L·mmol^{-1})	K_F	n_F	q_{LF} (mmol·g^{-1})	b_{LF} (L·mmol^{-1})	n_{LF}	R^2
Langmuir	0.96	89	-	-	-	-	-	0.94
Frendlich	-	-	0.91	7.1	-	-	-	0.89
LF	-	-	-	-	1.04	54	1.7	0.97

[a] q_L and q_{LF} are the maximum adsorbed amount of sorbent for the Langmuir and LF models, b_L and b_{LF} are the Langmuir and LF constants, K_F is the Freundlich constant, and n_F and n_{LF} are constants.

Next, the kinetic curve for the Sr^{2+} adsorption was measured on KTN_{flux}-500 and -600 for a low Sr^{2+} concentration of 25 ppm (the maximum Sr^{2+} ion-exchange capacity is ~0.28 mmol·g^{-1} for this concentration). For comparison, KTN_{SSR} was also used as an adsorbent. The Sr^{2+} adsorption kinetic curves are shown in **Figure 4.7**, where the initial pH was ~7.5. The Sr^{2+} ion-exchange reaction reached equilibrium within 1 and 3 h on KTN_{flux}-500 and -600, respectively, and more than 50% of the equilibrium amount of Sr^{2+} was adsorbed on KTN_{flux}-500 in 10 min. In contrast, it took ~25 h to reach equilibrium on KTN_{SSR}. We analyzed the kinetic curves on the KTN samples using the pseudo-first-order kinetic curve (Eq. (4-7)):[32]

$$q_t = q_e (1 - e^{-kt}) \qquad (4\text{-}7)$$

, where q_t and q_e (mmol·g^{-1}) are the amount of Sr^{2+} absorbed at time t and equilibrium, and k is the first-order rate constant (h^{-1}).

The determined kinetic parameters are summarized in **Table 4.3**. The k values for KTN_{flux}-500 and -600 are 4.89 and 1.52 h^{-1}, which are one order of magnitude higher than for KTN_{SSR} (0.19 h^{-1}). In general, ion-exchange rates increase with increasing exposed surface area of the adsorbent because of increasing number of accessible

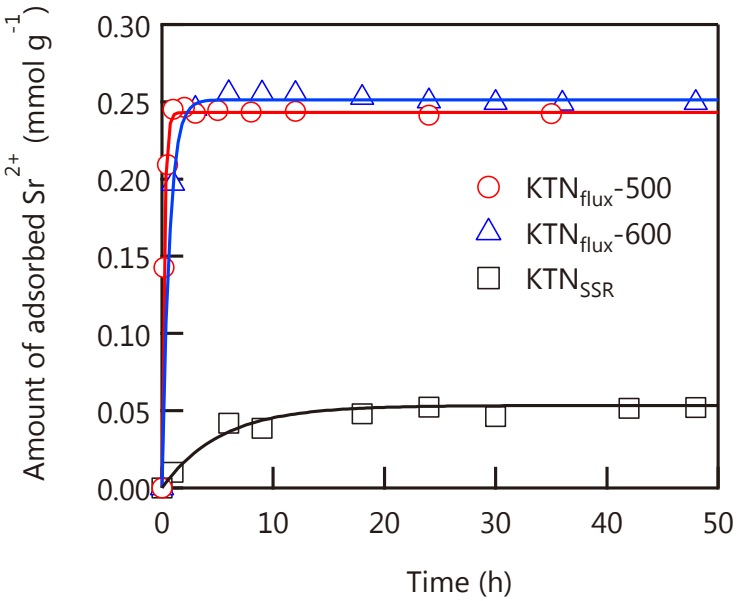

Figure 4.7 Kinetics curves of Sr^{2+} adsorption on KTN prepared by the KNO_3 flux method and SSR method. Conditions: pH ~7.5, volume/mass ratio ~1000 mL·g^{-1}, $[Sr^{2+}]_{initial}$ = ~25 ppm, room temperature.

adsorption sites. The higher first-order rate constants for KTN_{flux} compared with KTN_{SSR} are attributed to the platy morphology and larger surface areas.

Table 4.3 Pseudo-First-Order Kinetic Parameters for KTN Grown from KNO_3 Flux at 500 (KTN_{flux}-500) and 600 °C (KTN_{flux}-600), and by SSR (KTN_{SSR})[a]

Sample	k (h^{-1})	q_e ($mmol \cdot g^{-1}$)	R^2
KTN_{flux}-500	4.894	0.24	0.996
KTN_{flux}-600	1.529	0.25	0.998
KTN_{SSR}	0.190	0.05	0.940

[a]Adsorption conditions: pH ~7.5, volume/mass ratio ~1000 $mL \cdot g^{-1}$, $[Sr^{2+}]_{initial}$ = ~25 ppm, room temperature.

The distribution coefficient K_d^{Sr} for Sr^{2+} on KTN_{flux}-600 was then investigated at low Sr^{2+} concentration (~2 ppm) and in a wide pH range from 0.5 to 10.0. The K_d^{Sr} value indicates the selectivity of KTN for Sr^{2+}. **Figure 4.8** shows the K_d values for KTN_{flux}-600 as a function of pH. The K_d^{Sr} values were kept 4 × 10^4 $mL \cdot g^{-1}$ at pH = 3.0–10.0 and then decreased with decreasing the pH. K_d^{Sr} is still relatively high at low pH = ~1.9

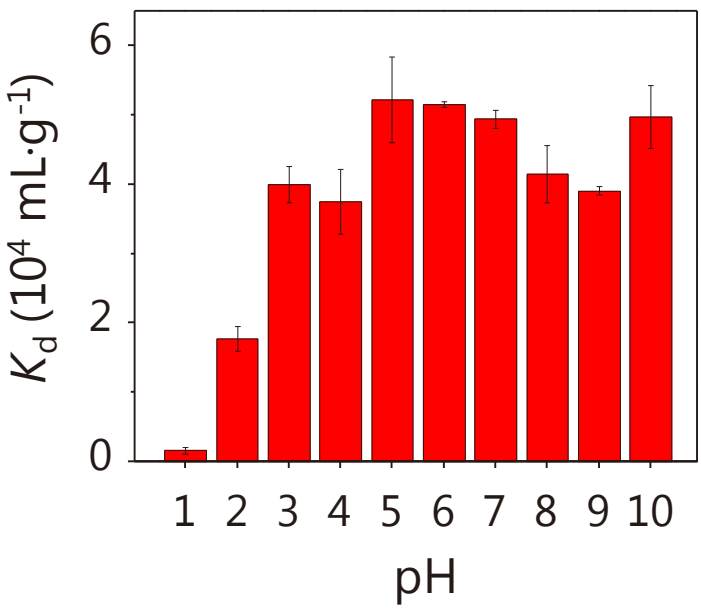

Figure 4.8 Distribution coefficient of Sr^{2+} (K_d) for KTN grown at 600 °C as a function of pH. Three or more experiments were performed under the same conditions for each point to check the reproducibility. Conditions: pH 0.5–10.0, $[Sr^{2+}]_{initial}$ = ~2 ppm, volume/mass ratio ~1000 $mL \cdot g^{-1}$, ion-exchange time 18 h; room temperature.

(K_d = 1.78 × 10^4 mL·g^{-1}). The reported K_d^{Sr} values of the efficient Sr^{2+} adsorbents KMS-1[12] and $Na_4Ti_9O_{20}\cdot xH_2O$[14] are 517 mL·$g^{-1}$ (pH ~2.1, [Sr^{2+}] = 4 ppm, volume/mass ratio 1000 mL·g^{-1}) and 32 mL·g^{-1} (pH ~2.0, [Sr^{2+}] = 87.6 ppm, volume/mass ratio 100 mL·g^{-1}), respectively. The K_d^{Sr} value for KTN_{flux}-600 is 2–4 orders of magnitude greater than those for these efficient Sr^{2+} adsorbents, showing the remarkably high affinity of KTN_{flux} for Sr^{2+} under acidic conditions. At pH = ~0.5, no framework species (< 0.05 mol%), such as Nb(V) and Ti(IV), leached from KTN_{flux}-600, indicating the remarkable chemical stability of KTN_{flux}.

The XRD pattern of KTN_{flux}-600 after ion exchange at pH = ~0.5 is shown in **Figure 4.9**. The diffraction peak associated with the layered structure is observed at about 9 ° after the Sr^{2+} ion-exchange reaction, indicating preservation of the layered structure during the Sr^{2+} ion-exchange process.

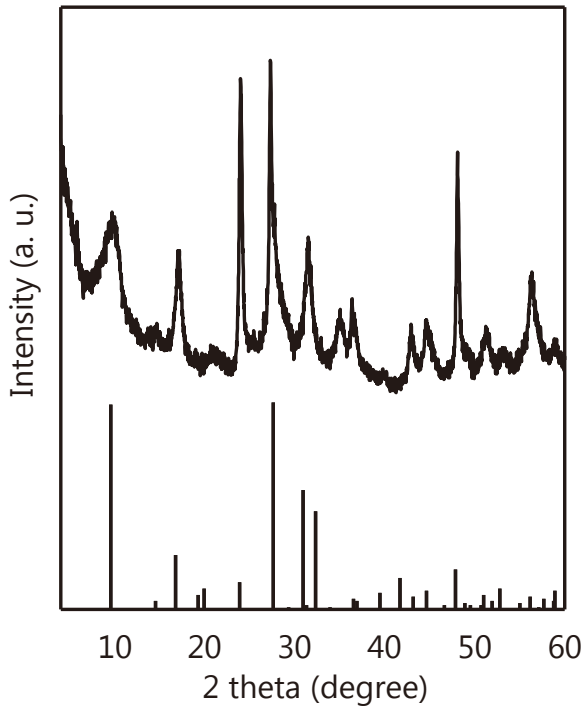

Figure 4.9 (Top) XRD pattern of $KTiNbO_5$ grown from KNO_3 flux at 600 °C after Sr^{2+} ion-exchange and (bottom) Powder Diffraction File pattern of reference $KTiNbO_5$ (#54-1155) is taken from the International Centre for Diffraction Data database. Conditions: pH ~0.5, $[Sr^{2+}]_{initial}$ = ~2 ppm, volume/mass ratio ~1000 mL g^{-1}, ion-exchange time 18 h.

Competitive Sr^{2+} adsorption experiments were then performed with high concentrations of Na^+, because Na^+ is the most abundant cation in nuclear waste.[9] To evaluate the Sr^{2+}/Na^+ selectivity, the distribution coefficients K_d^{Sr} and K_d^{Na} as well as the separation factor $SF_{Sr/Na} = K_d^{Sr}/K_d^{Na}$ were determined under various ion-exchange conditions. The $SF_{Sr/Na}$ value is an indicator of whether an adsorbent can distinguish Sr^{2+} from Na^+. Typically, the SF value should be >100 for an efficient separation system. The results for KTN_{flux}-600 are listed in **Table 4.4**. The $SF_{Sr/Na}$ values for KTN_{flux}-600 at pH = ~7.5 are 90, 374, and 1112 at Na^+ concentrations of 1, 10, and 100 mmol·L^{-1} (**Table 4.4**, Entry (2-1)–(2-4)), respectively. The selectivity of KTN_{flux}-600 for Sr^{2+} in the presence of Na^+ under highly basic condition (pH = 14.0) was also investigated. The K_d^{Sr} and $SF_{Sr/Na}$ values for KTN_{flux}-600 are 189959 mL·g^{-1} and 3220 (**Table 4.4**, Entry (4-5)). Compared with other inorganic exchangers (**Table 4.1**, Entries (4-4), (4-8), (4-17), (4-20), (4-22), and (4-23)), KTN_{flux}-600 shows exceptionally high Sr^{2+}/Na^+ selectivity under high concentrations of Na^+. The origin of such high preference for Sr^{2+} will be discussed in the next section.

Table 4.4 Distribution Coefficients (K_d) of Sr^{2+} and Na^+ and Separation Factors ($SF_{Sr/Na}$) for KTN Grown from KNO_3 Flux at 600 °C

Entry	[Na^+] (mmol·L^{-1})	K_d^{Sr} (mL·g^{-1})	K_d^{Na} (mL·g^{-1})	SF
4-1[a]	0	51501	—	—
4-2[a]	1	40946	454	90
4-3[a]	10	24706	66	374
4-4[a]	100	12617	11	1112
4-5[b]	5000	189959	59	3220

[a]Conditions: initial pH ~7.5, $[Sr^{2+}]_{initial}$ = ~2 ppm, volume/mass ratio ~1000 mL·g^{-1}, room temperature. [b]Conditions: initial pH ~14.0, $[Sr^{2+}]_{initial}$ = ~2 ppm, $[Na^+]_{initial}$ = ~115000 ppm, volume/mass ratio ~1000 mL·g^{-1}, room temperature.

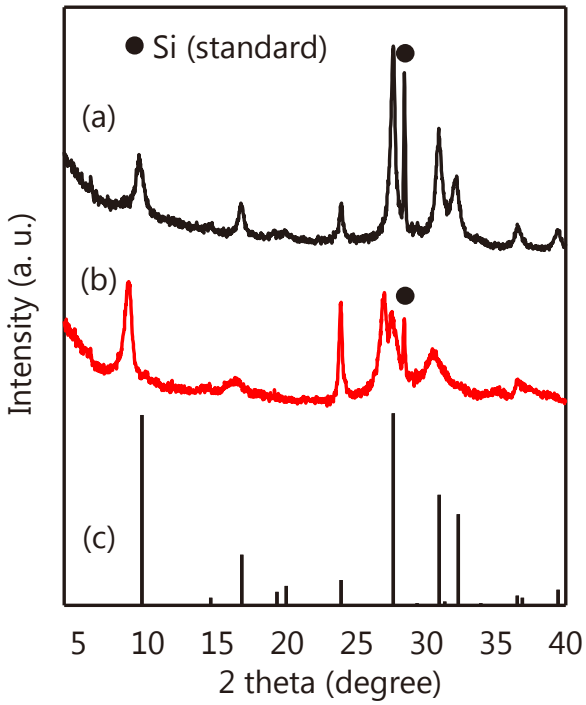

Figure 4.10 XRD patterns of $KTiNbO_5$ grown from KNO_3 flux at 600 °C (a) before and (b) after Sr^{2+} ion-exchange, and (c) the powder diffraction file pattern of reference $KTiNbO_5$ (#54-1155) is taken from the International Centre for Diffraction Data database. Conditions: pH ~7.5, volume/mass ratio ~1000 mL·g^{-1}, $[Sr^{2+}]_{initial}$ = 500 ppm, room temperature.

To understand the Sr^{2+} ion-exchange behavior in KTN, XRD and TG-DTA profiles of KTN_{flux}-600 were recorded before and after the Sr^{2+} ion exchange. **Figure 4.10** shows the XRD patterns of KTN_{flux}-600 before and after ion exchange. After Sr^{2+} adsorption, the peak owing to (002) diffraction was shifted to a lower angle, resulting in expansion of the interlayer from 0.942 to 1.025 nm. This expansion led to splitting of the (200)/(013) peaks around 27 °.

Figure 4.11a shows the TG-DTA profiles of KTN_{flux}-600 before and after Sr^{2+} ion exchange. Before ion exchange, the weight loss of parent KTN_{flux}-600 was less than 0.3 wt.%. In contrast, after ion exchange, there are two overlapping weight loss peaks at 40–100 and 100–250 °C in the profile of Sr^{2+}-substituted KTN. The weight loss can be attributed to desorption of water adsorbed on the surface and intercalated in the interlayers, according to the endothermic reactions. The weight loss resulting from the latter was ~2.5 wt.%, which corresponds to the nominal chemical formula

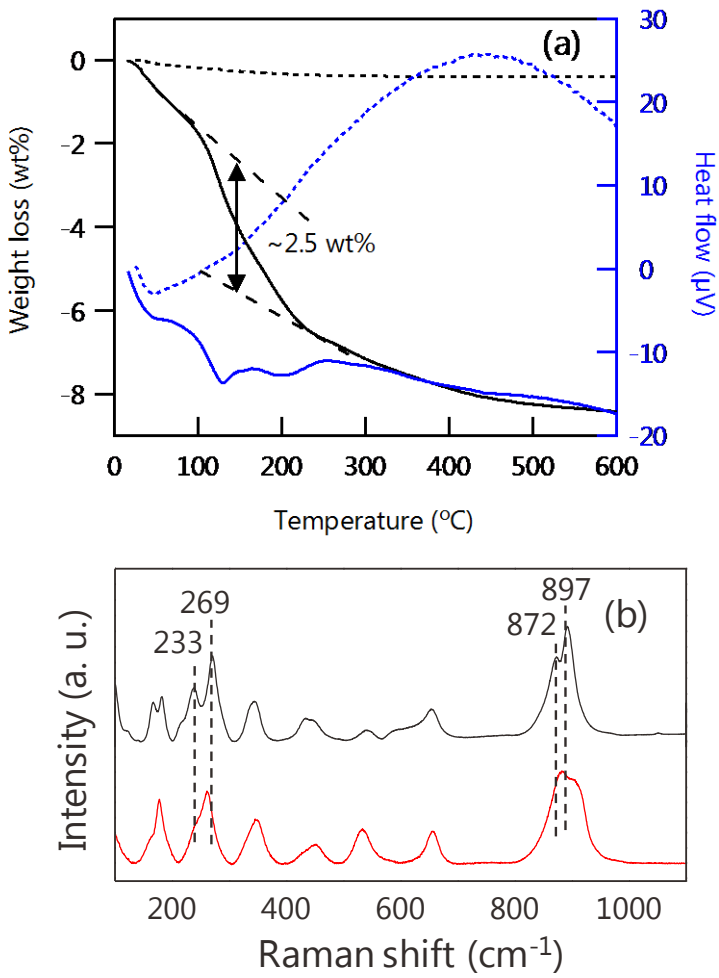

Figure 4.11 (a) TG-DTA profiles of KTN grown at 600 °C (KTN_{flux}-600) before (dashed line) and after (solid line) Sr^{2+} ion exchange and (b) Raman spectra of KTN_{flux}-600 before (black) and after (red) Sr^{2+} ion exchange. Conditions: pH ~7.5, $[Sr^{2+}]_{initial}$ = ~500 ppm, volume/mass ratio ~1000 mL·g^{-1}, room temperature.

$Sr_{0.27}K_{0.46}TiNbO_5 \cdot 0.36H_2O$ based on elemental analysis. Because the radius of Sr^{2+} (0.126 nm) is less than that of K^+ (0.151 nm),[33] the observed increment in the interlayers can be explained by the intercalation of water molecules.

Figure 4.11b shows Raman spectra of KTN_{flux}-600 before and after Sr^{2+} ion exchange for $[Sr^{2+}]$ = 500 ppm. Before ion exchange, there are bands at 237, 269, 873, and 897 cm^{-1}. The bands at 233, 269, and 897 cm^{-1} are assigned to stretching/bending vibrations of TiO_6 octahedra and those at 872 and 897 cm^{-1} are because of stretching/bending vibrations of NbO_6.[34] After ion exchange, the bands between 800 and 1000 cm^{-1} are broader, the band intensity at ~875 cm^{-1} increases, and that at ~900 cm^{-1} decreases, showing that the peaks of terminal Nb=O and Ti=O bonds shift to lower

wavenumbers and thereby change the relative intensity ratio of the peak at 872 cm^{-1} to that at 897 cm^{-1}. This spectrum change could be due to the replacement of K^+ by Sr^{2+} accompanying intercalation of water molecules. Namely, Sr^{2+} substitution and water intercalation can weaken the terminal Nb=O and Ti=O bonds by the interaction of Sr^{2+} and hydrogen species of water with terminal oxygen ions of $(Nb/Ti)_6$ octahedra.[35]

4.3.3 Structural modeling of adsorption sites in $KTiNbO_5$

To understand the high affinity of KTN for Sr^{2+}, we calculated the formation energies E^F for the alkali/alkaline-earth-cation-exchanged KTN by DFT. We first investigated the effect of cation size and valence on the formation energy using Sr^{2+}, Na^+, Ca^{2+}, Mg^{2+}, and K^+. **Figure 4.12a** shows the formation energies of cation-exchanged KTN as a function of the ionic radius of the cation (we recall that our computed E^F refers to $T = 0$ K, vacuum conditions, and 8 $KTiNbO_5$ formula units). The formation energy for cation-exchanged KTN decreases with increasing ionic radius, and is independent of the cation valence, indicating that the confinement of larger cations within the gallery is more favorable. In particular E^F is only ~0.3 eV for Sr^{2+}. The inclusion of configurational and vibrational entropic contributions under experimental conditions (25 °C, in aqueous solution) should further reduce this value thus making the substitution of K^+ by Sr^{2+} quite favorable.

Next, we investigated the effect of water molecule intercalation on the cation-exchange reaction. **Figure 4.12b** shows the effect of water molecule intercalation on the formation energies for Sr^{2+}- and Na^+-substituted KTNs with 0–2 water molecule(s) per supercell ($Z = 8$). **Figure 4.12c** shows changes in the c lattice parameter and unit cell volume for Sr^{2+} and Na^+ ion-exchanged KTN with increasing number of intercalated water molecules per supercell. There are three points to be noted. First, the c parameter and unit cell volume for Sr^{2+} ion-exchanged KTN increase with increasing number of water molecules (**Figure 4.12c**), which agrees well with the XRD patterns shown in **Figure 4.10**. The size of the cation and the interstitial/vacancy site space formed through the ion-exchange reaction could be responsible for the differences in

the *c* parameter and unit cell volume between the Sr^{2+} and Na^+ ion-exchanged KTN samples. Second, the formation energies of Sr^{2+} ion-exchanged KTNs are lower than those of $2Na^+$ ion-exchanged KTNs in all cases irrespective of the number of H_2O molecules, indicating the high affinity of KTN for Sr^{2+} even in the presence of water molecules in the gallery. The third point is that the formation energies of $Sr^{2+}/2Na^+$ ion-exchanged KTNs without water molecules are lower than those of the corresponding KTN with water molecules. We note however that the present static (T = 0 K) calculations do not allow for a full reorganization of the water molecules, including, *e.g.*, the possible formation of intermolecular H-bonds. This limitation can be overcome by finite temperature molecular dynamics simulations, which we plan to carry out in the near future. To determine the local structure of the adsorption sites on the KTN samples, we analyzed the coordination mode of exchangeable cations, including K^+ ions in the gallery. According to the crystal structure of KTN shown in **Figure 4.1**, the subnanometer-sized space constructed by eight apical oxygen ions of different MO_6 (M = Ti, Nb) units forms a monocapped octahedron. This can be considered as a distorted sub-nanopocket of ~3 Å in size responsible for selective Sr^{2+} adsorption, because the oxygen–oxygen distances of the cages and galleries of zeolites and smectite clays with ion-exchange abilities are from ~3 to ~6 Å.[36]

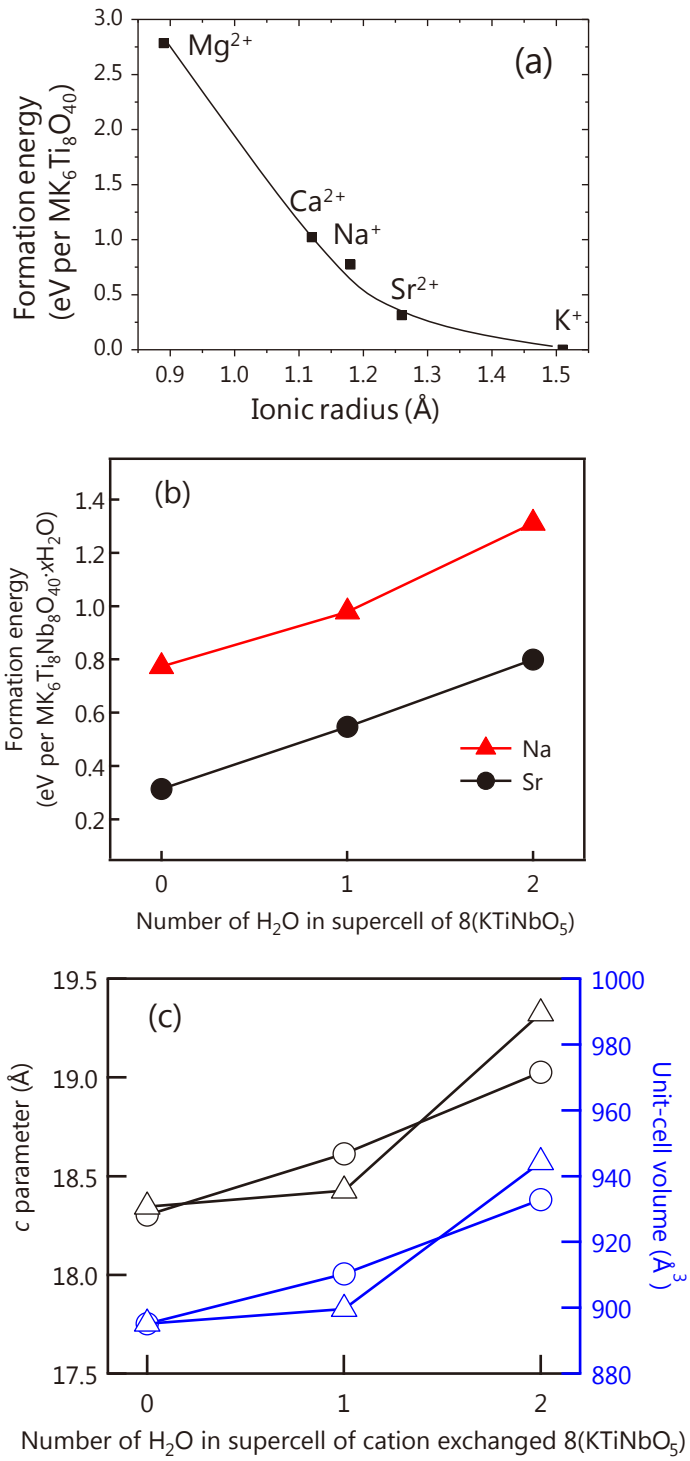

Figure 4.12 (a) Effect of ionic radius on the formation energy of alkali/alkaline earth ion-substituted KTN (M = Mg^{2+}, Ca^{2+}, Sr^{2+}, $2Na^+$ or $2K^+$). (b) Effect of intercalated water molecules on the formation energy of alkali/alkaline earth ion-substituted KTN accompanying water molecules (M = Sr^{2+}, $2Na^+$; $x = 0, 1, 2$). (c) c lattice parameter and unit cell volume of $SrK_6Ti_8Nb_8O_4\cdot xH_2O$ (black and blue triangles) and $Na_2K_6Ti_8Nb_8O_4\cdot xH_2O$ (black and blue circles) as a function of the number of water molecules in the supercell.

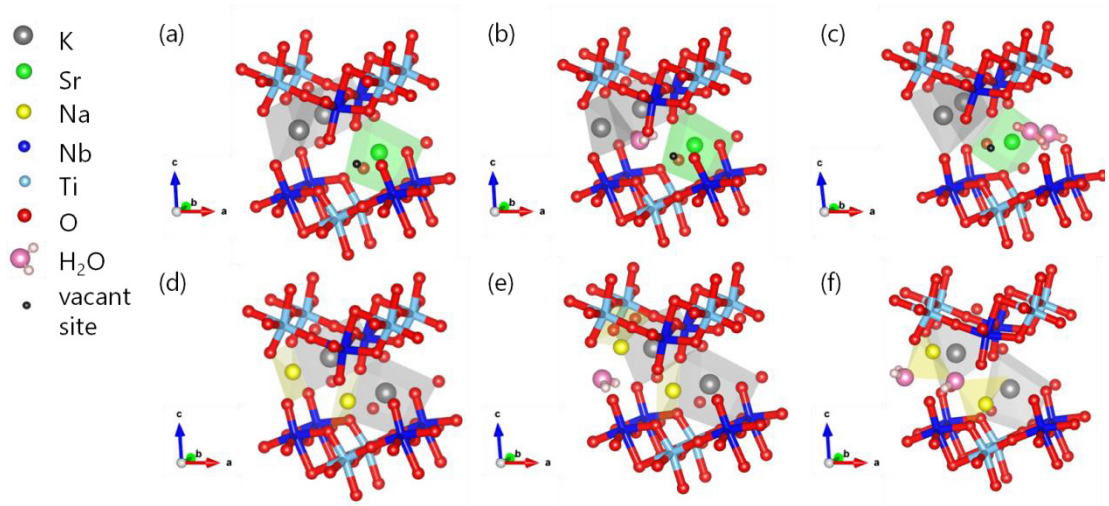

Figure 4.13 Local structures of Sr^{2+}- and Na^{+}-substituted KTN with and without intercalated water molecules: (a) $SrK_6Ti_8Nb_8O_{40}$, (b) $SrK_6Ti_8Nb_8O_{40}\cdot H_2O$, (c) $SrK_6Ti_8Nb_8O_{40}\cdot 2H_2O$, (d) $Na_2K_6Ti_8Nb_8O_{40}$, (e) $Na_2K_6Ti_8Nb_8O_{40}\cdot H_2O$, and (f) $Na_2K_6Ti_8Nb_8O_{40}\cdot 2H_2O$. Light gray spheres K, green spheres Sr, yellow spheres Na, blue Nb, light blue Ti, pink spheres O in H_2O, red spheres O, light pink spheres H, and black sphere vacant site. Polyhedra constructed by oxygen species of MO_6 (M = Ti, Nb) framed by rectangles and H_2O in the gallery represent the coordination mode of ion-exchangeable cations, which can be viewed as subnanometer-sized pockets binding K^+ (light grey), Sr^{2+} (light green), and Na^+ (light yellow). The crystal structures and fractional coordinates of each atom are summarized in **Figure 4.14** and **Tables 4.5, 4.6**. Crystal structures of KTN-based intercalates are visualized using the VESTA program.

Figure 4.13 and **Figure 4.14** show the local and crystal structures of Sr^{2+} and $2Na^+$ ion-exchanged KTN with and without intercalated water molecules optimized by DFT. First, we consider the result for the Sr^{2+} ion-exchanged KTN system. The exchange of one Sr^{2+} ion for two K^+ ions without water molecules resulted in formation of one vacant sub-nanopocket site (**Figure 4.13a**, small black sphere) neighboring the site binding the Sr^{2+} ion (**Figure 4.13a**, green sphere). The introduced Sr^{2+} was captured in the sub-nanopocket built from eight apical oxygen ions of different $(Nb/Ti)O_6$ octahedra. With progress in ion exchange, the coordination number of the original K^+ ion neighboring the vacant pocket decreased from eight (parent KTN) to six. Upon addition of one water molecule into the supercell, the water occupies the interstitial site between vacant site and K^+ ion, wherein it interacts with the terminal oxygen ions of

metalate slabs through (pseudo)hydrogen bonds. The K^+ ion neighboring the water-trapped site moves away from the introduced water (by ~0.5 Å) as a result of electrostatic repulsion: see gray polyhedra in **Figure 4.13b**. The intercalation of water into the gallery changes the coordination mode of this remaining K^+ ion bound to four apical oxygen ions of $(Nb/Ti)O_6$ units and one oxygen atom of the intercalated water molecule. As a result, introduction of water into the gallery can decrease the binding strength of K^+ ions in the pocket.

Addition of a second water molecule into the supercell further changes the coordination mode of exchangeable cations. This is accompanied by a rearrangement of the layered structure consisting of polyanionic slabs and counter cations. Namely, the *c* parameter increases with intercalation of water molecules (**Figure 4.12c**), and each slab slides by ~1 Å (**Figure 4.14**) across each sub-nanopocket. The introduction of two water molecules into the supercell changes the coordination mode of both K^+ and Sr^{2+}: all K^+ ions are surrounded by seven apical oxygen ions of $(Nb/Ti)O_6$ units, and the Sr^{2+} ion is surrounded by five apical oxygen ions of $(Nb/Ti)O_6$ and two oxygen

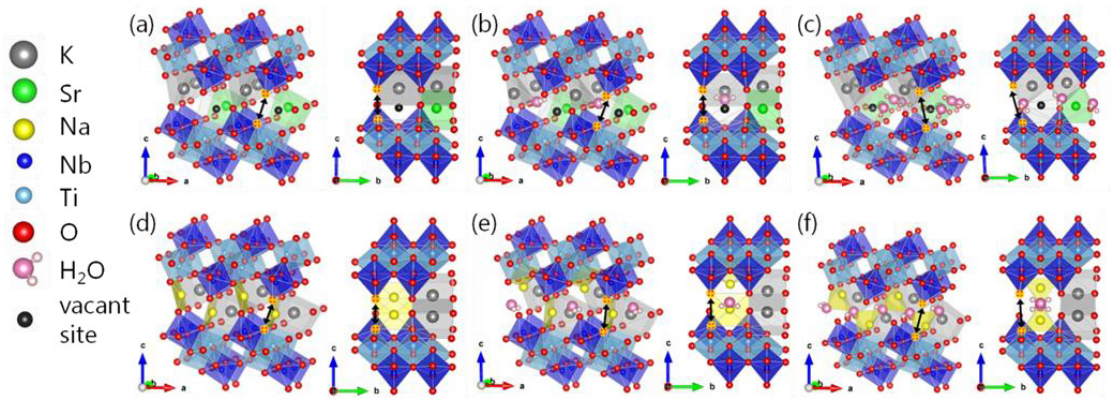

Figure 4.14 Optimized crystal structures of Sr^{2+}- and Na^+-substituted KTN with and without intercalated water molecules: (a) $SrK_6Ti_8Nb_8O_{40}$, (b) $SrK_6Ti_8Nb_8O_{40}\cdot H_2O$, (c) $SrK_6Ti_8Nb_8O_{40}\cdot 2H_2O$, (d) $Na_2K_6Ti_8Nb_8O_{40}$, (e) $Na_2K_6Ti_8Nb_8O_{40}\cdot H_2O$, and (f) $Na_2K_6Ti_8Nb_8O_{40}\cdot 2H_2O$. Gray spheres K, green spheres Sr, yellow spheres Na, blue Nb, light blue Ti, pink spheres O in H_2O, red spheres O, and light pink spheres H. Polyhedra constructed by oxygen species of MO_6 (M = Ti, Nb) and H_2O in the gallery represent the coordination mode of ion-exchangeable cations, which can be viewed as subnanometer-sized pockets binding K^+, Sr^{2+}, and Na^+. The black lines with arrows show the degree of shift of anionic slabs along the *a* and *b* axes. Crystal structures of KTN-based intercalates are visualized using the VESTA program.

atoms of different water molecules. It follows that in the absence/presence of water, the captured Sr^{2+} ion is confined within the distorted sub-nanopocket constructed by 7-8 oxygen species of anionic slabs and intercalated water, forming a monocapped heptahedron or octahedron.

Next, we examine the Na^+ ion-exchanged KTN system. When one Na^+ ion is exchanged with the K^+ ion in the absence of water, the Na^+ ion moves close to the center of the oxygen square unit of the $(Nb/Ti)O_6$ octahedron because the ionic radius of Na^+ (1.18 Å) is markedly smaller than that of K^+ (1.51 Å) (**Figure 4.13d**).[33] This structural arrangement forces the coordination number of Na^+ to be four, which is significantly lower than that of Sr^{2+} (eight) in the KTN samples. The addition of one water molecule into the supercell ($Z = 8$) forces the introduced Na^+ ion to move close to the introduced water molecule without change in its coordination number (**Figure 4.13e**). The two hydrogen atoms of the water molecule interact with apical oxygen ions of different NbO_6 octahedra through pseudo-hydrogen bonding. In contrast, the Na^+ ion moves to the center of another square unit constructed by the apical oxygen ions of NbO_6 that is adjacent to the square unit binding the Na^+ ion. The introduction of two water molecules into the supercell further changes the coordination modes. The hydrogen atoms of the two intercalated water molecules interact with the apical oxygen ions of NbO_6 octahedra (**Figure 4.13f**). The Na^+ ions move to the edge of the oxygen square unit, and interact with both the oxygen ions bridged by the Nb and Ti species, and another two oxygen atoms of individual intercalated water molecules. In this coordination state, slabs do not slide across the sub-nanopockets, which is in sharp contrast to the Sr^{2+} ion-exchanged KTN system.

Comparison of the Sr^{2+} and $2Na^+$ ion-exchanged KTN systems reveals two important aspects for selective Sr^{2+} adsorption in the sub-nanopocket of KTN. The first aspect is the so-called size matching effect,[37] originating from confinement within the sub-nanopocket built up from oxygen species of anionic metalate frameworks and intercalated water molecules. In exceptional cases, certain alkali ions (*i.e.*, K^+) are

strongly captured in the interlayer of clay compounds,[37] but in general larger cations are more stable in the gallery/cavity of layered materials because the electrostatic interaction between cation and anionic slabs increases with increasing cation size.[38] The smaller the exchanged cation, the lower the coordination number as a result of the disproportionate fitting of metal ions within the sub-nanopockets. This explains the observed trends in **Figure 4.12** for cation-exchanged KTN.

The second aspect is related to the solvation effect by solvents used as a medium. The coordination mode of cations in the gallery of KTN can change with intercalation of water molecules because of structural rearrangement of the layered structure. In the case of the Sr^{2+} ion-exchanged KTN system, the binding strength of both K^+ and Sr^{2+} within the sub-nanopockets decreases because of misalignment of anionic infinite slabs induced by intercalation of water. In addition, the coordination mode of exchangeable cations in the sub-nanopocket also varies depending on the size of the co-intercalated ion. For instance, with water in the gallery, the local structure of the adsorption site binding Sr^{2+} is completely different from that binding Na^+. In the former, Sr^{2+} is trapped in the center of the sub-nanopocket forming a heptahedron cage, and in the latter Na^+ is captured in the center of the oxygen square unit (**Figure 4.13c** vs. **Figure 4.13f**). Similarly, diverse changes in structural coordination and arrangement, which depend on the type of intercalated species and co-intercalated solvents, are found also in FeSe-based intercalates.[39,40] These results clearly indicate the complexity of binding mode for the captured ions within the gallery of layered materials, especially in the presence of solvents like water.

Table 4.5 Fractional Coordinates of Each Atom in $SrK_6Ti_8Nb_8O_{40}$, $SrK_6Ti_8Nb_8O_{40}\cdot H_2O$, and $SrK_6Ti_8Nb_8O_{40}\cdot 2H_2O$ Optimized by *ab initio* DFT Calculations

	$SrK_6Ti_8Nb_8O_{40}$[a]			$SrK_6Ti_8Nb_8O_{40}\cdot H_2O$[b]			$SrK_6Ti_8Nb_8O_{40}\cdot 2H_2O$[c]		
Atoms	*x*	*y*	*z*	*x*	*y*	*z*	*x*	*y*	*z*
Sr1	0.284	0.125	0.691	0.302	0.126	0.687	0.101	0.183	0.696
K1	0.790	0.125	0.812	0.800	0.126	0.808	0.713	0.071	0.828
K2	0.756	0.625	0.798	0.601	0.626	0.781	0.712	0.569	0.810
K3	0.220	0.375	0.193	0.232	0.375	0.192	0.212	0.366	0.190
K4	0.220	0.875	0.193	0.232	0.877	0.192	0.211	0.867	0.190
K5	0.720	0.374	0.308	0.728	0.375	0.306	0.728	0.375	0.299
K6	0.720	0.876	0.308	0.728	0.877	0.306	0.727	0.876	0.299
Ti1	0.322	0.125	0.033	0.337	0.126	0.033	0.288	0.098	0.038
Ti2	0.321	0.625	0.031	0.339	0.626	0.032	0.287	0.599	0.038
Ti3	0.682	0.375	0.965	0.694	0.375	0.964	0.632	0.341	0.973
Ti4	0.682	0.875	0.965	0.694	0.876	0.964	0.635	0.839	0.973
Ti5	0.176	0.375	0.536	0.182	0.376	0.534	0.217	0.403	0.518
Ti6	0.176	0.875	0.536	0.183	0.876	0.534	0.215	0.905	0.519
Ti7	0.821	0.125	0.467	0.823	0.126	0.466	0.853	0.142	0.452
Ti8	0.822	0.625	0.468	0.824	0.627	0.467	0.855	0.644	0.452
Nb1	0.773	0.125	0.110	0.788	0.126	0.109	0.753	0.108	0.111
Nb2	0.772	0.625	0.110	0.790	0.626	0.109	0.751	0.608	0.111
Nb3	0.231	0.371	0.886	0.239	0.371	0.888	0.169	0.328	0.901
Nb4	0.231	0.879	0.886	0.238	0.880	0.887	0.171	0.830	0.899
Nb5	0.723	0.371	0.613	0.733	0.372	0.611	0.771	0.409	0.586
Nb6	0.723	0.879	0.613	0.733	0.881	0.611	0.768	0.911	0.589
Nb7	0.274	0.125	0.390	0.276	0.126	0.389	0.293	0.136	0.379
Nb8	0.275	0.625	0.391	0.278	0.626	0.390	0.295	0.636	0.380
O1	0.068	0.125	0.073	0.084	0.126	0.073	0.041	0.104	0.075
O2	0.066	0.625	0.070	0.082	0.626	0.070	0.039	0.605	0.075
O3	0.936	0.376	0.925	0.950	0.372	0.925	0.883	0.335	0.940
O4	0.936	0.874	0.925	0.950	0.879	0.925	0.881	0.836	0.935
O5	0.429	0.361	0.575	0.435	0.365	0.572	0.480	0.411	0.555
O6	0.429	0.889	0.575	0.435	0.888	0.572	0.480	0.907	0.553
O7	0.569	0.125	0.427	0.572	0.126	0.425	0.593	0.139	0.414
O8	0.567	0.625	0.430	0.569	0.626	0.429	0.593	0.638	0.416
O9	0.645	0.125	0.989	0.658	0.126	0.989	0.601	0.093	0.995
O10	0.643	0.625	0.988	0.657	0.626	0.988	0.601	0.593	0.996
O11	0.358	0.376	0.008	0.371	0.377	0.008	0.319	0.346	0.015
O12	0.358	0.874	0.008	0.371	0.875	0.008	0.320	0.845	0.015
O13	0.857	0.376	0.492	0.859	0.378	0.491	0.891	0.397	0.476

O14	0.857	0.874	0.492	0.859	0.875	0.491	0.891	0.896	0.475
O15	0.140	0.125	0.510	0.145	0.126	0.507	0.180	0.150	0.493
O16	0.141	0.625	0.514	0.144	0.626	0.512	0.177	0.650	0.495
O17	0.466	0.125	0.121	0.480	0.126	0.120	0.447	0.109	0.121
O18	0.463	0.625	0.120	0.479	0.626	0.119	0.445	0.611	0.121
O19	0.539	0.374	0.877	0.550	0.369	0.878	0.474	0.331	0.889
O20	0.539	0.876	0.877	0.549	0.883	0.879	0.477	0.826	0.889
O21	0.031	0.350	0.624	0.038	0.346	0.622	0.091	0.404	0.600
O22	0.031	0.900	0.624	0.038	0.907	0.622	0.083	0.934	0.600
O23	0.967	0.125	0.379	0.969	0.126	0.378	0.983	0.133	0.368
O24	0.966	0.625	0.381	0.968	0.626	0.380	0.983	0.630	0.369
O25	0.845	0.125	0.206	0.856	0.126	0.204	0.837	0.119	0.202
O26	0.844	0.625	0.205	0.860	0.626	0.204	0.836	0.620	0.202
O27	0.166	0.331	0.792	0.190	0.336	0.791	0.055	0.299	0.813
O28	0.166	0.919	0.792	0.189	0.915	0.791	0.090	0.830	0.809
O29	0.642	0.340	0.706	0.638	0.329	0.702	0.755	0.389	0.680
O30	0.642	0.910	0.706	0.638	0.923	0.702	0.738	0.948	0.682
O31	0.346	0.125	0.295	0.348	0.125	0.294	0.350	0.125	0.288
O32	0.349	0.625	0.296	0.350	0.626	0.295	0.351	0.626	0.289
O33	0.241	0.125	0.923	0.254	0.126	0.923	0.187	0.084	0.932
O34	0.239	0.625	0.913	0.257	0.626	0.912	0.182	0.583	0.929
O35	0.763	0.375	0.078	0.777	0.376	0.078	0.734	0.354	0.081
O36	0.763	0.875	0.078	0.777	0.876	0.077	0.737	0.854	0.080
O37	0.263	0.375	0.423	0.265	0.376	0.421	0.287	0.389	0.409
O38	0.263	0.875	0.423	0.265	0.875	0.421	0.285	0.889	0.409
O39	0.731	0.125	0.576	0.733	0.126	0.573	0.785	0.157	0.557
O40	0.737	0.625	0.586	0.739	0.626	0.584	0.793	0.658	0.562
O41				0.978	0.626	0.738	0.370	0.430	0.711
O42				0.066	0.519	0.748	0.381	0.989	0.739
H1				0.065	0.734	0.748	0.296	0.479	0.669
H2							0.518	0.403	0.696
H3							0.502	0.946	0.711
H4							0.298	0.892	0.759

[a] a = 6.42888 Å, b = 7.58985 Å, c = 18.34494 Å, α = 90.0000°, β = 89.6289°, and γ = 90.0000°

[b] a = 6.43360 Å, b = 7.58843 Å, c = 18.42701 Å, α = 90.0135°, β = 89.8310°,and γ = 90.0156°

[c] a = 6.44545 Å, b = 7.60347 Å, c = 19.32395 Å, α = 93.0491°, β = 93.1747°, and γ = 90.1517°

Table 4.6 Fractional Coordinates of Each Atom in $Na_2K_6Ti_8Nb_8O_{40}$,

$Na_2K_6Ti_8Nb_8O_{40}\cdot H_2O$, and $Na_2K_6Ti_8Nb_8O_{40}\cdot 2H_2O$ Optimized by *ab initio* DFT Calculations

	$Na_2K_6Ti_8Nb_8O_{40}$[a]			$Na_2K_6Ti_8Nb_8O_{40}\cdot H_2O$[b]			$Na_2K_6Ti_8Nb_8O_{40}\cdot 2H_2O$[c]		
Atoms	*x*	*y*	*z*	*x*	*y*	*z*	*x*	*y*	*z*
Na1	0.634	0.125	0.796	0.680	0.132	0.850	0.662	0.140	0.855
Na2	0.134	0.125	0.704	0.143	0.128	0.712	0.039	0.011	0.713
K1	0.779	0.625	0.807	0.770	0.630	0.811	0.807	0.679	0.811
K2	0.228	0.375	0.192	0.218	0.377	0.196	0.220	0.382	0.199
K3	0.228	0.875	0.192	0.218	0.877	0.196	0.221	0.883	0.200
K4	0.728	0.375	0.308	0.726	0.375	0.310	0.728	0.384	0.309
K5	0.728	0.875	0.308	0.726	0.876	0.310	0.731	0.883	0.309
K6	0.279	0.625	0.693	0.280	0.627	0.696	0.319	0.631	0.665
Ti1	0.325	0.125	0.032	0.304	0.130	0.036	0.300	0.132	0.047
Ti2	0.329	0.625	0.030	0.301	0.630	0.037	0.299	0.635	0.047
Ti3	0.681	0.374	0.962	0.658	0.384	0.972	0.638	0.386	0.983
Ti4	0.681	0.876	0.962	0.659	0.878	0.972	0.651	0.883	0.982
Ti5	0.181	0.374	0.538	0.198	0.372	0.535	0.214	0.376	0.522
Ti6	0.181	0.876	0.538	0.197	0.874	0.534	0.203	0.880	0.524
Ti7	0.825	0.125	0.468	0.839	0.124	0.467	0.846	0.130	0.458
Ti8	0.829	0.625	0.470	0.841	0.624	0.466	0.849	0.628	0.459
Nb1	0.778	0.125	0.108	0.763	0.129	0.114	0.763	0.129	0.119
Nb2	0.781	0.625	0.107	0.760	0.629	0.115	0.762	0.629	0.119
Nb3	0.226	0.373	0.886	0.200	0.381	0.893	0.172	0.390	0.912
Nb4	0.226	0.877	0.886	0.200	0.880	0.893	0.189	0.893	0.910
Nb5	0.726	0.373	0.614	0.748	0.376	0.608	0.765	0.368	0.595
Nb6	0.726	0.877	0.614	0.747	0.871	0.608	0.755	0.869	0.594
Nb7	0.278	0.125	0.392	0.285	0.124	0.391	0.289	0.131	0.386
Nb8	0.281	0.625	0.393	0.287	0.624	0.391	0.291	0.633	0.387
O1	0.073	0.125	0.071	0.052	0.130	0.075	0.053	0.132	0.084
O2	0.073	0.625	0.069	0.052	0.629	0.077	0.050	0.629	0.083
O3	0.936	0.383	0.923	0.907	0.376	0.931	0.888	0.384	0.947
O4	0.936	0.867	0.923	0.907	0.888	0.931	0.896	0.888	0.944
O5	0.436	0.383	0.577	0.458	0.379	0.570	0.471	0.386	0.559
O6	0.436	0.867	0.577	0.457	0.866	0.569	0.464	0.866	0.561
O7	0.573	0.125	0.429	0.582	0.124	0.428	0.589	0.129	0.421
O8	0.573	0.625	0.431	0.583	0.624	0.428	0.590	0.631	0.422
O9	0.648	0.125	0.987	0.623	0.130	0.992	0.614	0.133	0.004
O10	0.644	0.625	0.985	0.626	0.630	0.995	0.611	0.634	0.004
O11	0.362	0.375	0.007	0.340	0.380	0.014	0.333	0.385	0.024
O12	0.362	0.875	0.007	0.339	0.879	0.014	0.333	0.884	0.024

O13	0.862	0.375	0.493	0.875	0.373	0.490	0.885	0.377	0.480
O14	0.862	0.875	0.493	0.875	0.875	0.490	0.885	0.878	0.481
O15	0.148	0.125	0.513	0.162	0.123	0.509	0.174	0.128	0.500
O16	0.144	0.625	0.515	0.159	0.623	0.511	0.170	0.628	0.501
O17	0.471	0.125	0.119	0.455	0.128	0.123	0.458	0.129	0.129
O18	0.472	0.625	0.118	0.453	0.629	0.124	0.456	0.632	0.129
O19	0.537	0.364	0.875	0.509	0.387	0.885	0.484	0.374	0.899
O20	0.537	0.886	0.875	0.509	0.876	0.885	0.494	0.899	0.899
O21	0.037	0.364	0.625	0.060	0.364	0.621	0.078	0.374	0.604
O22	0.037	0.886	0.625	0.059	0.880	0.621	0.072	0.879	0.606
O23	0.971	0.125	0.381	0.975	0.125	0.380	0.981	0.134	0.375
O24	0.972	0.625	0.382	0.978	0.625	0.380	0.982	0.632	0.376
O25	0.847	0.125	0.204	0.840	0.128	0.207	0.845	0.123	0.209
O26	0.850	0.625	0.203	0.838	0.628	0.209	0.845	0.626	0.209
O27	0.167	0.361	0.789	0.127	0.386	0.799	0.093	0.395	0.822
O28	0.167	0.889	0.789	0.126	0.872	0.799	0.105	0.905	0.820
O29	0.667	0.361	0.711	0.686	0.392	0.703	0.728	0.352	0.686
O30	0.667	0.889	0.711	0.681	0.855	0.702	0.732	0.862	0.686
O31	0.347	0.125	0.296	0.350	0.125	0.297	0.349	0.134	0.295
O32	0.350	0.625	0.297	0.351	0.625	0.297	0.350	0.634	0.296
O33	0.237	0.125	0.920	0.219	0.130	0.924	0.196	0.137	0.942
O34	0.249	0.625	0.914	0.207	0.630	0.926	0.200	0.639	0.939
O35	0.767	0.375	0.076	0.748	0.380	0.083	0.744	0.381	0.089
O36	0.767	0.875	0.076	0.749	0.879	0.083	0.749	0.880	0.088
O37	0.267	0.375	0.424	0.276	0.374	0.422	0.284	0.381	0.416
O38	0.267	0.875	0.424	0.276	0.874	0.422	0.282	0.881	0.415
O39	0.737	0.125	0.580	0.757	0.123	0.580	0.772	0.122	0.564
O40	0.749	0.625	0.586	0.770	0.624	0.576	0.781	0.622	0.566
O41				0.477	0.125	0.749	0.257	0.226	0.716
O42				0.552	0.232	0.729	0.503	0.504	0.772
H1				0.551	0.017	0.730	0.207	0.302	0.754
H2							0.203	0.284	0.671
H3							0.581	0.420	0.742
H4							0.481	0.449	0.819

[a] a = 6.46052 Å, b = 7.57050 Å, c = 18.30275 Å, α = 90.0000°, β = 90.0000°, and γ = 90.0000°

[b] a = 6.43674 Å, b = 7.59947 Å, c = 18.61259 Å, α = 89.8481°, β = 91.2463°, and γ = 90.0002°

[c] a = 6.44369 Å, b = 7.60885 Å, c = 19.02640 Å, α = 89.9516°, β = 89.9449°, and γ = 89.9811°

4.4 Conclusion

Platy KTN_{flux} crystals with selective Sr^{2+} removal ability were successfully prepared using the KNO_3 flux method, and the origin of the high preference for Sr^{2+} was identified by DFT calculations. The surface areas of KTN_{flux} are 48–86 $m^2 \cdot g^{-1}$ depending on the growth temperature, which is 1–2 order(s) of magnitude greater than that of KTN prepared by SSR (<1 $m^2 \cdot g^{-1}$). Notably, the growth temperature (500–600 °C) for the KNO_3 flux method is ~500 °C lower than that for the SSR method (1100 °C). Equilibrium isotherm analysis shows that the Sr^{2+} ion-exchange capacity of KTN_{flux} at 600 °C is 1.04 $mmol \cdot g^{-1}$, and most of its ion-exchange sites are homogeneous and localized. Competitive cation-exchange experiments indicate that KTN_{flux}-600 shows high preference for Sr^{2+} in comparison to Na^+ and at low pH, and the K_d^{Sr} values are 1.26×10^4 $mL \cdot g^{-1}$ at 0.1 M Na^+ and 1.78×10^4 $mL \cdot g^{-1}$ at pH ~1.9. During these studies, we found that the released amount of Ti(IV) and Nb(V) species were <0.05 mol% even in extremely acidic conditions.

DFT studies clearly indicate that the formation energy and binding mode for cation-exchanged KTN are strongly dependent on both the type of cation and the intercalation degree of water molecules. Comparative study of cation-exchanged KTNs with/without water molecules indicates that the coordination mode varies with increasing size of the intercalated cation and intercalation degree of water molecules, resulting in diverse structural arrangements. The high preference of KTN for Sr^{2+} is attributed to confinement within the subnanometer-sized pockets constructed by five apical oxygen ions of individual $(Ti/Nb)O_6$ units and two oxygen atoms of intercalated water molecules, forming a distorted monocapped heptahedron. The matching of the Sr^{2+} ion size with the pocket space of the adsorption site and the stabilization effect of intercalated solvent (H_2O) in the gallery are responsible for selective Sr^{2+} adsorption.

All together, our results highlight the importance of three underlying requirements for the rational design of inorganic ion-exchangers, especially for the selective uptake

of metal cations. First, a polyanionic metalate framework with high charge density is preferable because strong electrostatic interactions between the anionic frameworks and target cations can suppress the swelling of interlayers and the intercalation of excess water molecules, both of which weaken the interaction between the target ion and the anionic slabs. Second, controlling the pocket size of the relevant adsorption sites is crucial for selective ion adsorption. It is indeed well accepted that the distance between adsorbates and the top surface of adsorption sites is an important parameter for recognition and sensing of ions at the atomic scale in layered materials.[37,41] Finally, orientation and configuration of solvent molecules intercalated into the cavity/gallery should also be considered, as strong interactions, including (pseudo)hydrogen bonding with the metalate slabs, could give a large formation energy for the adsorbent–adsorbate complex.

References

(1) Rahman, R. O. A.; Ibrahium, H. A.; Hung, Y. T. Liquid Radioactive Wastes Treatment: A Review. *Water* **2011**, *3*, 551–565.

(2) Pedersen, C. Cyclic Polyethers and Their Complexes with Metal Salts. *J. Am. Chem. Soc.* **1967**, *89*, 7017–7036.

(3) McGovern, R. E.; Humberto, F.; Khan, A. R.; Power, N. P.; Crowley, P. B. Protein Camouflage in Cytochrome C–Calixarene Complexes. *Nature Chem.* **2012**, *4*, 527–533.

(4) Barrow, S. J.; Kasera, S.; Rowland, M. J.; del Barrio, J.; Scherman, O. A. Cucurbituril-Based Molecular Recognition. *Chem. Rev.* **2015**, *115*, 12320–12406.

(5) Minodani, S.; Owaki, M.; Sano, S.; Tsuzuki, S.; Yamanaka, M. Reinforcement of Guest Selectivity through the Self-Assembly of Host Molecules: Selective Recognition of Lithium Ions by Dimerizable Tricarboxylic Acids. *Chem. Commun.* **2015**, *51*, 12920–12923.

(6) Chen, B.; Xiang, S.; Qian, G. Metal-Organic Frameworks with Functional Pores for Recognition of Small Molecules. *Acc. Chem. Res.* **2010**, *43*, 1115–1124.

(7) Paulus, W. J.; Komarneni, S.; Roy, R. Bulk Synthesis and Selective Exchange of Strontium Ions in $Na_4Mg_6Al_4Si_4O_{20}F_4$ Mica. *Nature* **1992**, *357*, 571–573.

(8) El-Kamash, A. M. Evaluation of Zeolite A for the Sorptive Removal of Cs^+ and Sr^{2+} Ions from Aqueous Solutions Using Batch and Fixed Bed Column Operations. *J. Hazard. Mater.* **2008**, *151*, 432–445.

(9) Solbrå, S.; Allison, N.; Waite, S.; Mikhalovsky, S. V.; Bortun, A I.; Bortun, L. N.; Clearfield, A. Cesium and Strontium Ion Exchange on the Framework Titanium Silicate $M_2Ti_2O_3SiO_4 \cdot nH_2O$ (M = H, Na). *Environ. Sci. Technol.* **2001**, *35*, 626–629.

(10) Nyman, M.; Tripathi, A.; Parise, J. B.; Maxwell, R. S.; Nenoff, T. M. Sandia Octahedral Molecular Sieves (SOMS): Structural and Property Effects of Charge-Balancing the M^{IV}-Substituted (M = Ti, Zr) Niobate Framework. *J. Am. Chem. Soc.* **2002**, *124*, 1704–1713.

(11) Möller, T.; Harjula, R.; Pillinger, M.; Dyer, A.; Newton, J.; Tusa, E.; Amin, S.; Webb, M.; Araya, A. Uptake of ^{85}Sr, ^{134}Cs and ^{57}Co by Antimony Silicates Doped with Ti^{4+}, Nb^{5+}, Mo^{6+} and W^{6+}. *J. Mater. Chem.* **2001**, *11*, 1526–1532.

(12) Manos, M. J.; Ding, N.; Kanatzidis, M. G. Layered Metal Sulfides: Exceptionally Selective Agents for Radioactive Strontium Removal. *Proc. Natl. Acad. Sci. U. S. A.* **2008**, *105*, 3696–3699.

(13) Sarma, D.; Malliakas, C. D.; Subrahmanyam, K. S.; Islam, S. M.; Kanatzidis, M. G. $K_{2x}Sn_{4-x}S_{8-x}$ (x = 0.65–1): A New Metal Sulfide for Rapid and Selective Removal of Cs^+, Sr^{2+} and UO_2^{2+} Ions. *Chem. Sci*. **2016**, *7*, 1121–1132.

(14) Lehto, J.; Clearfield, A. The Ion Exchange of Strontium on Sodium Titanate $Na_4Ti_9O_{20}\cdot xH_2O$. *J. Radioanal. Nucl. Chem.* **1987**, *118*, 1–13.

(15) Yang, D.; Zheng, Z.; Zhu, H. Titanate Nanofibers as Intelligent Absorbents for the Removal of Radioactive Ions from Water. *Adv. Mater.* **2008**, *20*, 2777–2781.

(16) Sun, J.; Yang, D.; Sun, C.; Liu, L.; Yang, S.; Jia, Y.; Cai, R.; Yao, X. Potassium Niobate Nanolamina: A Promising Adsorbent for Entrapment of Radioactive Cations from Water. *Sci. Rep.* **2014**, *4*, 7313.

(17) Qi, X.; Du, K.; Feng, M.; Li, J.; Du, C.; Zhang, B. A Two-Dimensionally Microporous Thiostannate with Superior Cs^+ and Sr^{2+} Ion-Exchange Property. *J. Mater. Chem. A* **2015**, *3*, 5665–5673.

(18) Behrens, E. A.; Sylvester, P.; Clearfield, A. Assessment of a Sodium Nonatitanate and Pharmacosiderite-Type Ion Exchangers for Strontium and Cesium Removal from DOE Waste Simulants. *Environ. Sci. Technol.* **1998**, *32*, 101–107.

(19) Solbrå, S.; Allison, N.; Waite, S.; Mikhalovsky, S. V.; Bortun, A I.; Bortun, L. N.; Clearfield, A. Cesium and Strontium Ion Exchange on the Framework Titanium Silicate $M_2Ti_2O_3SiO_4\cdot nH_2O$ (M = H, Na). *Environ. Sci. Technol.* **2001**, *35*, 626–629.

(20) Mertz, J. L.; Fard, Z. H.; Malliakas, C. D.; Manos, M. J.; Kanatzidis, M. G. Selective Removal of Cs^+, Sr^{2+}, and Ni^{2+} by $K_{2x}Mg_xSn_{3-x}S_6$ (x = 0.5−1) (KMS-2) Relevant to Nuclear Waste Remediation. *Chem. Mater.* **2013**, *25*, 2116–2127.

(21) Takagaki, A.; Sugisawa, M.; Lu, D.; Kondo, J. N.; Hara, M.; Domen, K.; Hayashi, S. Exfoliated Nanosheets as a New Strong Solid Acid Catalyst. *J. Am. Chem. Soc.* **2003**, *125*, 5479–5485.

(22) Nakato, T.; Matsumoto, Y. Preparation of a Layered Titanoniobic Acid–Alumina Nanocomposite and Its Potential Applicability to Removal of Organic Contaminants in Water. *J. Porous Mater.* **2004**, *11*, 79–86.

(23) Rebbah, H.; Desgardin, G.; Raveau, B. Nonstoichiometric Oxides with a Layer Structure: The Compounds $A_{1-x}(Ti_{1-x}M_{1+x})O_5$. *J. Solid State Chem*. **1980**, *31*, 321–328.

(24) Teshima, K.; Lee, S.; Yamaguchi, A.; Suzuki, S.; Yubuta, K.; Ishizaki, T.; Shishido, T.; Oishi, S. The Growth of Highly Crystalline, Idiomorphic Potassium Titanoniobate Crystals by the Cooling of a Potassium Chloride Flux. *CrystEngComm* **2011**, *13*, 1190–1196.

(25) Jang, J.; Kim, H.; Reddy, V.; Bae, S.; Ji, S.; Lee, J. Photocatalytic Water Splitting over Iron Oxide Nanoparticles Intercalated in $HTiNb(Ta)O_5$ Layered Compounds. *J. Catal.* **2005**, *231*, 213–222.

(26) Giles, C. H.; MacEwan, T. H.; Nakhwa, S. N.; Smith, D. Studies in Adsorption. Part XI. A System of Classification of Solution Adsorption Isotherms, and Its Use in Diagnosis of Adsorption Mechanisms and in Measurement of Specific Surface Areas of Solids. *J. Chem. Soc.* **1960**, *846*, 3973–3993.

(27) Rouquerol, J.; Rouquerol, F.; Llewellyn, P.; Maurin, G.; Sing, K. S. *Adsorption by Powders and Porous Solids: Principles, Methodology and Applications*; Academic Press: Oxford, U.K., 1998.

(28) Kresse, G.; Furthmuller, J. Efficient Iterative Schemes for *Ab Initio* Total-Energy Calculations Using a Plane-Wave Basis Set. *Phys. Rev. B* **1996**, *54*, 11169–11186.

(29) Kresse, G.; Furthmuller, J. Efficiency of *Ab-Initio* Total Energy Calculations for Metals and Semiconductors Using a Plane-Wave Basis Set. *Comput. Mater. Sci.* **1996**, *6*, 15–50.

(30) Perdew, J. P.; Ruzsinszky, A.; Csonka, G. I.; Vydrov, O. A.; Scuseria, G. E.; Constantin, L. A.; Zhou, X.; Burke, K. Restoring the Density-Gradient Expansion for Exchange in Solids and Surfaces. *Phys. Rev. Lett.* **2008**, *100*, 136406.

(31) Blochl, P. E. Projector Augmented-Wave Method. *Phys. Rev. B* **1994**, *50*, 17953–17979.

(32) Ho, Y. Citation review of Lagergren kinetic rate equation on adsorption reactions. *Scientometrics* **2004**, 59, 171–177.

(33) Shannon, R. D. Revised Effective Ionic Radii and Systematic Studies of Interatomic Distances in Halides and Chalcogenides. *Acta. Cryst.* **1976**, *A32*, 751–767.

(34) Yang, G.; Kong, Y.; Hou, W.; Yan, Q. Heating Behavior and Crystal Growth Mechanism in Microwave Field. *J. Phys. Chem. B* **2005**, *109*, 1371–1379.

(35) Byeon, S.; Nam, H. Neutron Diffraction and FT-Raman Study of Ion-Exchangeable Layered Titanates and Niobates. *Chem. Mater.* **2000**, *12*, 1771–1778.

(36) Baerlocher, C.; McCusker, L. B. Database of Zeolite Structures. http://www.iza-structure.org/databases/ (accessed, May 10th, 2016).

(37) Liu, X.-D.; Lu, X.-C. A Thermodynamic Understanding of Clay-Swelling Inhibition by Potassium Ions. *Angew. Chem. Int. Ed.* **2006**, *45*, 6300–6303.

(38) Fujiki, Y.; Komatsu, Y.; Sasaki, T. *Ceramics* (in Japanese), **1984**, *19*, 126–133.

(39) Hayashi, F.; Lei, H.; Guo, J.; Hosono, H. Modulation Effect of Interlayer Spacing on the Superconductivity of Electron-Doped FeSe-Based Intercalates. *Inorg. Chem.* **2015**, *54*, 3346–3351.

(40) Guo, J.; Lei, H.; Hayashi, F.; Hosono, H. Superconductivity and Phase Instability of NH_3-Free Na-Intercalated $FeSe_{1-z}S_z$. *Nature Commun.* **2014**, *5*, 4756.

(41) Takagi, S.; Shimada, T.; Ishida, Y.; Fujimura, T.; Masui, D.; Tachibana, H.; Eguchi, M.; Inoue, H. Size-Matching Effect on Inorganic Nanosheets: Control of Distance, Alignment, and Orientation of Molecular Adsorption as a Bottom-Up Methodology for Nanomaterials. *Langmuir* **2013**, *29*, 2108–2119.

Chapter 5
Summary

Chapter 5 Summary

The present dissertation demonstrates efficient growth of functional oxide-based crystals with two- or three-dimensionally nanostructured channels from various fluxes. The resulting crystals showed faceted surface features, which could be amenable to ion exchange applications. The discussion on crystal growth manner from different flux systems gives a deep insight into factors which control the crystal shapes and exposed facets.

In **chapter 1**, the background of water purification issue was introduced. Ion exchange techniques, materials, and theory were then introduced in details. Subsequently, flux method that was used for preparation of target materials in this study was introduced. Finally, the objective and outline of this study were shown.

In **chapter 2**, platy $KTiNbO_5$ crystals were successfully grown from KNO_3 flux (KTN_{flux}), it shows selective uptake ability towards Sr^{2+} ion, and the origin of the high preference for Sr^{2+} was identified by DFT calculations. KTN_{flux} grown at 500-600 ºC show surface areas of 48-86 $m^2 \cdot g^{-1}$, which are 1-2 order(s) of magnitude larger than that (<1 $m^2 \cdot g^{-1}$) of KTN prepared through solid-state reaction at 1100 ºC. Adsorption experiments show that KTN_{flux} has high Sr^{2+} selectivity and remarkable durability at low pH conditions (pH = 0.5) as well as at $[Na^+]$ = 0.1 mol L^{-1}. Density Functional Theory (DFT) calculations reveal diverse changes in the local structure of adsorption sites and binding mode with intercalating exchangeable cations and water molecules. The high preference of $KTiNbO_5$ for Sr^{2+} is attributed to confinement within the subnanometer-sized pockets constructed by five apical oxygen ions of individual $(Ti/Nb)O_6$ units and two oxygen atoms of intercalated waters, forming a distorted mono-capped heptahedron. The matching of the Sr^{2+} ion size with the pocket space of the adsorption site and the stabilization effect of intercalated solvent (H_2O) in the gallery are responsible for selective Sr^{2+} adsorption. The results provide important

insights that will help design/identify highly selective and chemically stable adsorbents for Sr^{2+} at low pH.

In **Chapter 3**, idiomorphic $Li_5La_3Ta_2O_{12}$ single crystals were successfully grown at low temperature using LiOH flux, and their growth manner were also discussed based on the results of different crystal growth conditions. Pseudo-peroviskite $LiLa_2TaO_6$, initially formed during the holding at 500 °C, was efficiently transformed into $Li_5La_3Ta_2O_{12}$. At 700 ºC, $Li_5La_3Ta_2O_{12}$ were transformed to $Li_7La_3Ta_2O_{13}$ as a result of the reaction of $Li_5La_3Ta_2O_{12}$ with Li_2O. The holding time dependence experiments indicated that the pseudo-perovskite-type $LiLa_2TaO_6$ is a key intermediate for the formation of $Li_5La_3Ta_2O_{12}$. On the other hand, the evaporation ratio and cooling rate did not affect the phase and morphology of crystals. Low solute concentrations (1 or 5 mol%) improved the shape and dispersity of the crystals. These results indicate that the idiomorphic $Li_5La_3Ta_2O_{12}$ crystals are formed from LiOH flux through the combination of the chemical reaction with repeated dissolution-precipitation processes. The present results thus open new routes for the fabrication of related garnet-type materials.

In **Chapter 4**, the faceted β-Li_2TiO_3 crystals were successfully anisotropic grown from flux method and the growth manner of β-Li_2TiO_3 crystals were comprehensively studied as a function of variable parameters, such as type of flux, holding temperature and time, and solute concentration. Among various fluxes (LiCl, NaCl, KCl, Li_2SO_4, K_2SO_4, and Na_2SO_4), the use of Na_2SO_4 as a flux at 1000 ºC with solute concentration of 20 mol% enables the growth of platy and faceted β-Li_2TiO_3 crystals with ~15.0 μm in lateral size and aspect ratio of 3.5. This anisotropic crystal growth could be attributed to the concerted effects of the preferential attachment of sodium cations on the {001} faces, and efficient dissolution of β-Li_2TiO_3 crystals as well as the solvation of the resulting O^{2-} ions in the oxysalt fluxes.

Publications and Awards

Journal Papers

(1) Xiong Xiao, Hajime Wagata, Fumitaka Hayashi, Hitoshi Onodera, Kunio Yubuta, Nobuyuki Zettsu, Shuji Oishi, and Katsuya Teshima: Unique Growth Manner of $Li_5La_3Ta_2O_{12}$ Crystals from Lithium Hydroxide Flux at Low Temperature; *Cryst. Growth Des.*, 15 (10), 4863-4868 (2015).

(2) Xiong Xiao, Fumitaka Hayashi, Hiromasa Shiiba, Sencer Selcuk, Kazuhiro Ishihara, Kenta Namiki, Lei Shao, Hiromasa Nishikiori, Annabella Selloni, and Katsuya Teshima: Platy $KTiNbO_5$ as a Selective Sr Ion Adsorbent: Crystal Growth, Adsorption Experiments, and DFT Calculations; *J. Phys. Chem. C*, 120 (22), 11984–11992 (2016).

(3) Xiong Xiao, Fumitaka Hayashi, Kunio Yubuta, Annabella Selloni, Katsuya Teshima, Effects of Alkali Cations and Sulfate/Chloride Anions on the Flux Growth of {001}-Faceted β-Li_2TiO_3 Crystals; *Cryst. Growth Des.*, 17 (3), 1118–1124 (2017).

Awards

(1) The Best Oral Presentation Award in the Flux Growth Society of Japan held to Tohoku University, Sendai in 9th December 2016.

(2) The Best Poster Paper in the International Union of Materials Research Societies – International Conference in Asia 2013(IUMRS-ICA 2013) held at Indian Institute of Science, Bangalore during 16 – 20 December 2013.

International Conference Papers

(1) Xiong Xiao, Hajime Wagata, Katsuya Teshima, Shuji Oishi: Growth of Layered $KTiNbO_5$ Crystals from Potassium Salt Fluxes; The 13th International Symposium on Biomimetic Materials Processing (BMMP-13th) pp.23 (2013).

(2) Xiong Xiao, Hajime Wagata, Nobuyuki Zettsu, Shuji Oishi, Katsuya Teshima: Strontium Ion Exchange property of Flux Grown $KTiNbO_5$ Crystals; IUPAC 9th International Conference on Novel Materials and Synthesis (NMS-IX) & 23rd International Symposium on Fine Chemistry and Functional Polymers (FCFP-XXIII) H9 (2013).

(3) Hajime Wagata, Xiong Xiao, Nobuyuki Zettsu, Shuji Oishi and Katsuya Teshima: Flux Grown $KTiNbO_5$ Crystals for Removal of Metal Ions in Aqueous Solutions; International Union of Materials Research Societies – International Conference in Asia 2013 (IUMRS-ICA 2013).

(4) Xiong Xiao, Hajime Wagata, Nobuyuki Zettsu, Shuji Oishi, Katsuya Teshima: Flux growth of $KTiNbO_5$ Crystals and Their Strontium Ion Exchange Properties; International Union of Materials Research Societies - The 15th IUMRS International Conference in Asia, p. 28 (2014).

(5) Xiong Xiao, Hajime Wagata, Fumitaka Hayashi, Hitoshi Onodera, Nobuyuki Zettsu, Shuji Oishi, Katsuya Teshima: Low-temperature Growth of $Li_5La_3Ta_2O_{12}$ Crystals from Lithium Hydroxide Flux and Investigation of Their Growth Mechanism; The 15th International Symposium on Biomimetic Materials Processing (BMMP-15th) pp.36 (2015).

(6) Fumitaka Hayashi, Xiong Xiao, Kazuhiro Ishihara, Kenta Namiki, Shuji Oishi, Katsuya Teshima: Selective Removal of Sr(II) Ion from Aqueous Solution by Flux-Grown $KTiNbO_5$ Crystals with Zig-Zag Layered Nano-Structure; International Symposium on Ecotopia Science 2015 (ISETS '15) (2015).

Domestic Conferences (in Japan)

(1) Xiong Xiao, Hajime Wagata, Nobuyuki Zettsu, Shuji Oishi, Katsuya Teshima：The Growth and Modification of Layered Titanium- and/or Niobium-Based Oxides Crystals by Using Flux Method; The 5th Monotsukuri Workshop, p.9 (2013).

(2) Xiong Xiao, Hajime Wagata, Nobuyuki Zettsu, Shuji Oishi, Katsuya Teshima：

Flux Growth of $KTiNbO_5$ Crystals and Their Applications to Adsorption of Strontium Ion from Aqueous Solution; H26 Materials Science and Technology Conference in Japan, pp.92-93 (2014).

(3) Xiong Xiao, Hajime Wagata, Nobuyuki Zettsu, Shuji Oishi, Katsuya Teshima：Flux Growth of $KTiNbO_5$ Crystals and Their Applications to Adsorption of Strontium Ion from Aqueous Solution; The 6th Monotsukuri Workshop, p.16 (2014).

(4) Xiong Xiao, Hajime Wagata, Fumitaka Hayashi, Nobuyuki Zettsu, Shuji Oishi, Katsuya Teshima：Growth of Idiomorphic $Li_5La_3Ta_2O_{12}$ Crystals from Lithium Hydroxide Flux; The 44th National Conference on Crystal Growth (NCCG-44), (2014).

(5) Xiong Xiao, Hajime Wagata, Fumitaka Hayashi, Hitoshi Onodera, Nobuyuki Zettsu, Shuji Oishi, Katsuya Teshima：Growth of Idiomorphic $Li_5La_3Ta_2O_{12}$ Crystals from Lithium Hydroxide Flux; H26 Workshop of Four University, 2014 (2014).

(6) Xiong Xiao, Hajime Wagata, Fumitaka Hayashi, Hitoshi Onodera, Nobuyuki Zettsu, Shuji Oishi, Katsuya Teshima：Low Temperature Flux Growth of Idiomorphic $Li_5La_3Ta_2O_{12}$ Crystals from a Lithium Hydroxide Flux; The 9th Flux Growth Conference in Japan, p.77 (2014).

(7) Xiong Xiao, Fumitaka Hayashi, Hajime Wagata, Hitoshi Onodera, Nobuyuki Zettsu, Shuji Oishi, Katsuya Teshima: Exploring Ion-Sieve Property of Flux-Grown $Li_5La_3Ta_2O_{12}$ Crystals; H27 Materials Science and Technology Conference in Japan, pp.100-101 (2015).

(8) Xiong Xiao, Fumitaka Hayashi, Hajime Wagata, Hitoshi Onodera, Nobuyuki Zettsu, Shuji Oishi, Katsuya Teshima: Low-Temperature Flux-Growth of Ion-Exchangeable $Li_5La_3Ta_2O_{12}$ Crystals; The 7th Monotsukuri Workshop, p.19-20 (2015).

(9) Xiong Xiao, Fumitaka Hayashi, Hajime Wagata, Hitoshi Onodera, Nobuyuki Zettsu, Shuji Oishi, Katsuya Teshima: Growth Manner of Ion-Exchangeable $Li_5La_3Ta_2O_{12}$ Crystals from Lithium Hydroxide Flux; The 28th Fall Meeting_The Ceramic Society of Japan 1F20 (2015).

(10) Xiong Xiao, Fumitaka Hayashi, Hiromasa Shiiba, Shuji Oishi, Katsuya Teshima: Flux-Grown $KTiNbO_5$ Crystals with a Flaky-Like Structure as a Selective and Durable Ion-Exchanger for Sr(II) Removal from Aqueous Solution; H27 Workshop of Four University, 2015 (2015).

(11) Xiong Xiao, Fumitaka Hayashi, Shuji Oishi, Katsuya Teshima: Lithium Ion Exchange Properties of Titanate-Based Crystals with Different Nano-Structures; The 10th Flux Growth Conference in Japan, p.62 (2015).

(12) Xiong Xiao, Fumitaka Hayashi, Tomohito Sudare, Kunio Yubuta, Annabella Selloni, Shuji Oishi, Katsuya Teshima: Effects of Alkali Metal Salt Based Fluxes on Growth of Platy Li_2TiO_3 Crystals; The 11th Flux Growth Conference in Japan, p.94 (2016).

Acknowledgements

First and foremost, I would like to thank my supervisor, Professor Katsuya Teshima at the Shinshu University, for his courage in accepting me to the doctoral program, taking me under his wings, and giving me financial assistance and research advice. I would like to thank Assistant Professor Fumitaka Hayashi at the Shinshu University, and Senior Assistant Professor Hajime Wagata at the Meiji University for doing their work on much more than 100%, being there for me when I needed them the most, proofreading my papers late in the midnight and on the weekends.

I would like to thank to Professor Lei Shao at the Beijing University of Chemical Technology who encouraged me to further my studies in Japan. Thanks to Professor Shuji Oishi at the Nagano Prefecture Nanshin Institute of Technology for always encouraging me. Thanks to Association Professor Nobuyuki Zettsu at the Shinshu University for giving advice to me when I need help, especially, his encouraging eyes when I did presentation in conferences. Thanks to Association Professor Kunio Yubuta at the Tohoku University for TEM measurement of my samples. Thanks to Dr. Hiromasa Shiiba for his kind answering my questions in DFT calculation and guiding me on the using of calculation software. Thanks to Dr. Takeshi Kimijima for teaching me to prepare materials using solvothermal method. Thanks to Assistant Professor Sayaka Suzuki at the Shinshu University for discussing researches and inviting me to dinners. Thanks to Assistant Professor Tetsuya Yamada at the Shinshu University for his patience explanation and advice for my questions. Thanks to Assistant Professor Tomohito Sudare for his kind discussion. Thanks to Dr. Yusuke Mizuno for patiently answering my questions and encouraging me. Thanks to Dr. Daewook Kim for giving me advices in my research. Thanks to Hitoshi Onodera-san for teaching me how to use QuartzVS and encouraging me when I feel down. Thanks to Dr. Yousuke Moriya for teaching me how to calibrate the TG-DTA. Thanks to all the researchers who answered my emails and provided their papers free of charge to me.

I thank my dissertation committee members, Professor Yuji Matsumoto at the Tohoku University, Professor Hiromasa Nishikiori at the Shinshu University, Professor Seiichi Taruta at the Shinshu University, Associate Professor Tomohiko Okada at the Shinshu University, and Associate Professor Nobuyuki Zettsu at the Shinshu University, for their valuable comments on my dissertation.

I also would like to thank Fumi Okada-san for drawing beautiful schematic illustration to my papers. Thanks to all the secretaries in the Teshima' Group, Michie Aoki-san, Izumi Takahana-san and Kyoko Clancy-san, for helping me preparation of all my documents for entering school, business travel, and the conferences. Thanks to Kyoko Clancy-san again for taking me to the hospital and police office when I got into a traffic accident. Thanks to all the technique staffs in the Teshima's Group, Kumiko Ishii-san, Hanae Kondou-san, Keiko Satou-san, Reiko Shiozawa-san and Miho Shimizu-san, for helping me to read the manuals and to operate the instruments. Thanks to Kumiko Ishii-san again for teaching Yoga free of charge to us. Thanks to Keiko Nishizawa-san and Masayuki Takeuchi-san in the Administration Center for helping me to prepare documents for the foreigner student and inviting me to various activities. I should thank to Keiko Nishizawa-san again for helping me moving my luggage using her private car. Thanks to Japanese language teacher, Mrs. Qiaki Ogikubo, at the Nagano campus for her patience and kindness in teaching me Japanese. Thanks to administrator Ojii-tyan and Obaa-tyan (sorry for I don't know their name) who clean the foreigner students dormitory everyday to give us comfortable living environment when I lived there.

I also want to thank Hikaru Inagaki-san, Akemi Shirasaki-san, Hitoshi Onodera-san, Kosuke Shimizu-san, Mayuu Tanaka-san, Kenta Kawashima-san, Shimono-tyan who studied in Teshima's Group for helping me to accommodate the new environment quickly when I came to Japan. Thanks to Yuuko Yamamoto-san, Kazuya Ogawa-san, Yuuto Kamiya-san, Yukinori Murada-san, Yoshiki Saitou-san, Toshiki Imabori-san, Yuusuke Satou-san, Atsushi Zenzai-san, Minori Yanai-san, and all the students in the Teshima's group for creating a good research atmosphere. Thanks to Kazuya Ogawa-

san again for giving me medicine when I got cold and thanks to Erika Wada-san again to give me special chocolate and wishes before the final defense.

I have to offer my special thanks to my friends. Thanks to Dr. Boyang Guo who is always there for me in my darkest hours. Thanks to Doctoral student Suehan Lee for helping and taking care of me when she was in Nagano. Thanks to Professor Cruz-Silva Rodolfo who has given me a lot of advices. Thanks to all my friends who is not here with me but care about me.

Finally, I thank my parents, Yelie Xiao and Lihua Lan, for all the supports and loves they have provided. Thanks to my grandma and other family members for their loves and understanding.

March, 2017, in Nagano

Xiong XIAO